

Titre: Wideband Line/Cable Models for Real-Time and Off-Line Simulations
Title: of Electromagnetic Transients

Auteur: Octavio Ramos Leanos
Author:

Date: 2013

Type: Mémoire ou thèse / Dissertation or Thesis

Référence: Ramos Leanos, O. (2013). Wideband Line/Cable Models for Real-Time and Off-Line
Citation: Simulations of Electromagnetic Transients [Thèse de doctorat, École
Polytechnique de Montréal]. PolyPublie. <https://publications.polymtl.ca/1134/>

 **Document en libre accès dans PolyPublie**
Open Access document in PolyPublie

URL de PolyPublie: <https://publications.polymtl.ca/1134/>
PolyPublie URL:

**Directeurs de
recherche:** Jean Mahseredjian, José Luis Naredo Villagen, & Christian Dufour
Advisors:

Programme: génie électrique
Program:

UNIVERSITÉ DE MONTRÉAL

WIDEBAND LINE/CABLE MODELS FOR REAL-TIME AND OFF-LINE
SIMULATIONS OF ELECTROMAGNETIC TRANSIENTS

OCTAVIO RAMOS LEANOS

DÉPARTEMENT DE GÉNIE ÉLECTRIQUE
ÉCOLE POLYTECHNIQUE DE MONTRÉAL

THÈSE PRÉSENTÉE EN VUE DE L'OBTENTION
DU DIPLÔME DE PHILOSOPHIAE DOCTOR
(GÉNIE ÉLECTRIQUE)

AVRIL 2013

UNIVERSITÉ DE MONTRÉAL

ÉCOLE POLYTECHNIQUE DE MONTRÉAL

Cette thèse intitulée:

WIDEBAND LINE/CABLE MODELS FOR REAL-TIME AND OFF-LINE
SIMULATIONS OF ELECTROMAGNETIC TRANSIENTS

présentée par: RAMOS LEANOS Octavio

en vue de l'obtention du diplôme de : Philosophiae Doctor

a été dûment accepté par le jury d'examen constitué de :

M. KOCAR ILHAN, Ph.D., président

M. MAHSEREDJIAN JEAN, Ph.D., membre et directeur de recherche

M. NAREDO VILLAGRAN JOSE LUIS, Ph.D., membre et codirecteur de recherche

M. DUFOUR CHRISTIAN, Ph.D., membre et codirecteur de recherche

M. MARTINEZ VELASCO JUAN A., Ph.D., membre

M. GAGNON RICHARD, Ph.D., membre

DEDICATORY

To the memory of a great friend: Miguel Angel Gonzalez

AKNOWLEDGMENTS

To my friend and advisor Jose Luis Naredo Villagran. Thank you for your patience, time and guidance.

To my advisor Jean Mahseredjian. Thank you for the opportunity and for letting me know that knowledge can be acquired from every situation.

To Christian Doufour. Thank you for the trust.

To Alberto Gutierrez for your friendship and invaluable help

To my family the best thing I have in my life.

To CONACYT for financial support.

To God for making all of this possible.

RESUMÉ

Cette thèse présente le développement d'un modèle mathématique pour les lignes et câbles de transmission de puissance. Ce modèle est utilisé pour la simulation des transitoires électromagnétiques en temps réel et en temps différé. La contribution est particulièrement utile à la simulation en temps réel car ce type de modèle n'existait pas avant. Le modèle permet d'améliorer la vitesse des calculs et contribue aussi à la recherche sur la stabilité numérique.

Le modèle proposé est basé sur le modèle WideBand (WB) aussi appelé "Universal line model (ULM)". Il permet de prendre en compte la dépendance en fréquence des paramètres de ligne et câble. Le modèle ULM est donc reformulé et restructuré dans cette thèse pour répondre aux exigences strictes des simulations en temps réel.

La structure du nouveau modèle facilite la séparation des réseaux en sous-blocs qui peuvent être simulés en parallèle par un ensemble de processeurs. Une caractéristique de l'ULM qui a été préservée dans le nouveau modèle, est la représentation rationnelle des matrices d'admittance caractéristique et de fonction de propagation. Ces matrices sont obtenues directement dans le domaine des phases en utilisant les méthodes "Vector Fitting" (VF) ou mieux "Weighted Vector Fitting" (WVF). Une question nécessitant une considération particulière, est la manipulation des variables d'état complexes produits par les pôles complexes lors de l'utilisation de WVF. L'approche standard pour répondre à cette question est l'approche directe consistant à traiter tous les états internes comme complexes. Dans le cas des états réels, les parties imaginaires sont simplement nulles. Dans le cas des états complexes, les parties imaginaires doivent s'annuler entre elles car les pôles complexes et les états complexes se produisent en paires conjuguées. Clairement, cette approche standard applique un grand nombre d'opérations triviales et redondantes et inefficace. L'alternative proposée dans cette thèse est la manipulation de toutes les variables d'état en arithmétique réelle. Pour ce faire, deux méthodologies sont développées, implémentées et testées dans cette thèse.

La méthode 1 consiste à éliminer un des états de chacune des paires conjuguées, puisqu'il est démontré dans cette thèse que les deux états transmettent la même information. Chacun des états complexes restants est ensuite traité comme une paire d'états réels mutuellement couplés. En faisant cela la performance numérique du modèle est augmentée de presque quatre fois. Le nouveau modèle basé sur cette méthode est implémentée sur la plateforme RT-Lab/Artemis de la

compagnie Opal-RT permettant d'effectuer des simulations en temps réel. Ce modèle amélioré est aussi implémenté dans le logiciel EMTP-RV qui fonctionne en temps différé.

La méthode 2 consiste à grouper chaque paire de variables d'état dans un seul état décrit par une équation différentielle ordinaire (ODE). Puisque les variables d'état complexes conjuguées sont groupées, toutes les ODEs de second ordre sont dans le domaine réel. Le modèle basé sur cette approche obtient un gain additionnel de 20% en temps de calcul.

Le manque de passivité des modèles MIMO ("Multiple Input-Multiple Output") synthétisés, comme l'ULM, est un problème récurrent et un sujet de recherche actuel. Trois causes importantes de ce problème sont identifiées et rapportées dans cette thèse et des lignes directrices d'évitement sont présentées. Une des causes est le regroupement des fonctions de propagation modales selon les délais de propagation. L'objectif de ce regroupement est la réduction des temps de calcul, mais on constate pour la première fois dans cette thèse que ce regroupement peut causer des problèmes de stabilité et on propose une nouvelle approche.

La précision et la performance du modèle proposé ont été testées par comparaison avec le logiciel EMTP-RV.

ABSTRACT

The development of a mathematical model for the electromagnetic simulation of power transmission lines and cables is described in this thesis along with its hardware and software implementation. This model is intended for real-time and accelerated-time simulation of electromagnetic transients (EMTs) occurring in power-supply networks. The developed model fills an existing gap in real-time simulation practice and, in comparison with those ones currently available to power-system analysts; it represents a substantial improvement in terms of stability and of computational-efficiency.

The proposed line model is based on the Wide Band (WB) or Universal Line Model (ULM) which, because of its accuracy and generality, is widely adopted as the referent. These two features of the ULM follow from its ability to account completely and effectively for all the frequency-dependent effects of line parameters. Nevertheless, the original ULM has been reformulated and restructured here to meet the stringent requirements for real-time simulations.

The structure of the new model facilitates the partition of large networks in sub-blocks that can be simulated in parallel on a multiprocessor cluster. One feature of the ULM that is preserved in the new model is the rational representation of the characteristic admittance and the propagation function matrices, both obtained directly in the phase domain by using the Vector Fitting (VF) or the Weighted Vector Fitting (WVF) software utilities. One issue requiring special consideration is the handling of the complex state variables produced by complex poles that often arise when using VF or WVF. The standard approach to this is the direct one consisting in the treating of all internal states as complex. In the case of real states, the imaginary parts simply are zeros. In the case of complex states, the imaginary parts must cancel each other since complex poles and complex states occur in conjugate pairs. Clearly, from the computational standpoint this standard approach reports a large number of trivial and redundant operations and thus, from the computational standpoint, it is deemed here as highly inefficient. The alternative proposed in this thesis is the handling of all state variables in real Arithmetic. Two methods for doing this are developed, implemented and tested in this thesis.

Method 1 consists in discarding one state out of each conjugate pair, since it is demonstrated in this thesis that both states convey the same information. Each of the remaining complex states is then treated as a pair of mutually-coupled real states. By doing this, the

numerical efficiency of the line model is increased in about four times. The line model version based on this method is already implemented in the RT-Lab/Artemis platform to conduct parallel and real-time EMT simulations. This line model is implemented as well in the EMTP-RV with the purpose of speeding up off-line EMT simulations.

Method 2 consists in grouping each pair of state variables into a single state ruled by a second order ordinary differential equation (ODE). Since the complex state variables are paired among conjugates, all the second order ODEs are in Real Domain. The model based on this method provides an additional 20 % improvement of computational efficiency.

The lack of passivity of synthesized MIMO (Multiple Input-Multiple Output) models, such as the ULM, is a recurrent problem and an ongoing research topic. Three important causes for this problem are identified and reported here; moreover, guidelines to avoid it are provided here. One of the causes is the grouping of modal propagation functions in delay groups. The standard practice for the rational synthesis of line propagation matrices is to group line modal functions with nearly equal travel times. The purpose of this is to reduce computations. Nevertheless, it is found here that the grouping of modal functions with magnitudes differing beyond a certain threshold is a major cause for loss of passivity at synthesized line models.

The accuracy and the computational performance of the proposed line model have been tested by comparisons against the original ULM model available in EMTP-RV.

TABLE OF CONTENTS

DEDICATORY	III
AKNOWLEDGMENTS	IV
RÉSUMÉ.....	V
ABSTRACT	VII
TABLE OF CONTENTS	IX
LIST OF FIGURES.....	XIV
LIST OF ACRONYMS AND ABBREVIATIONS.....	XX
LIST OF APPENDICES	XXII
CHAPTER 1 INTRODUCTION.....	1
1.1 Electromagnetic Transient Analysis for Modern Power Systems.....	1
1.2 State of the Art in Power Line and Cable Modeling	2
1.3 Problem Statement	3
1.4 Thesis Objectives	4
1.5 Contributions of this thesis.....	4
CHAPTER 2 TRANSMISSION LINE ANALYSIS	8
2.1 Electromagnetic Basis of Line Theory	9
2.1.1 Single-phase case: first line equation	10
2.1.2 Single-phase case: second line equation	14
2.1.3 Multiconductor case: first line equation.....	17
2.1.4 Multiconductor case: second line equation	22
2.2 Frequency-domain solution of multiconductor line equations.....	24
2.3 Two-Port Line Representations.....	27
2.4 Remarks.....	31

CHAPTER 3	TRAVELLING-WAVE BASED LINE MODELS.....	32
3.1	Preamble.....	32
3.2	CP Model.....	33
3.3	FD (Frequency Dependent) Line Model	34
3.4	FDQ Cable Model	36
3.5	Universal Line Model (ULM)	38
3.6	WB Model vs CP Model	47
3.6.1	Real-Time WB (RTWB) ac 3-phase Cable.....	47
3.6.2	CP 3-phase aerial line.....	50
3.6.3	RTWB 6-phase underground cable	53
3.6.4	Transmission Network	55
3.7	WB Model vs FD Model.....	57
3.7.1	Double Circuit Aerial Line.....	58
3.7.2	BC HYDRO 9-Phase Aerial Line	62
3.8	Remarks.....	64
CHAPTER 4	RATIONAL REALIZATIONS.....	65
4.1	Vector Fitting	65
4.2	Weighted Vector Fitting.....	69
4.3	Fitting of the Characteristic Admittance Matrix	70
4.4	Fitting of the Propagation Function Matrix.....	70
4.5	Causality, Stability and Passivity	71
4.6	Passivity	72
4.6.1	Passivity test.....	72
4.6.2	Effect of the number of data samples on passivity.....	73

4.6.3	Effect of fit order on passivity.....	78
4.6.4	Effect of modal grouping on passivity	83
4.7	Remarks.....	92
CHAPTER 5 COMPUTATIONAL EFFICENCY IMPROVEMENT		94
5.1	First Order Realizations: Complex States with Real Arithmetic	95
5.2	Second Order Realizations	99
5.3	Higher Order Realizations.....	103
5.4	Application Examples	105
5.4.1	Example 1: aerial line.....	106
5.4.2	Example 2: underground cable.....	109
5.4.3	Example 3: 3-phase underground cable	112
5.4.4	Performance of proposed realizations	115
5.5	Remarks.....	115
CHAPTER 6 REAL-TIME WIDE-BAND (RTWB) LINE MODEL.....		117
6.1	Overview of Real-Time Platform.....	117
6.2	RTWB Using First Order Realizations with Real Arithmetic.....	119
6.3	RTWB Using Second Order Realizations	126
6.4	Limiting Factors in the RTWB Model	127
6.5	Test of RTWB in a Real-Time Platform	129
6.5.1	Test 1: RTWB ac 3-phase Cable	129
6.5.2	Test 2: BC HYDRO 9-phase aerial line	132
6.5.3	Test 3: RTWB 6-phase underground cable	135
6.5.4	Test 4: transmission network.....	135
6.6	Remarks.....	135

CHAPTER 7	CONCLUSION	138
7.1	Future Work	140
REFERENCES.....		142
APPENDIX I.....		147

LIST OF TABLES

Table 3.1 : RTWB ac 3-Phase Cable Provenance and Data.....	48
Table 3.2 : CP 3-Phase Aerial Line Provenance and Data.....	52
Table 3.3 : RTWB 6-Phase Cable Provenance and Data	54
Table 3.4 : Double Circuit Aerial Line Provenance and Data	58
Table 4.1 : RTE dc-Cable Provenance and Data.....	74
Table 4.2 : Mader ac-distribution 12-phase Cable's Provenance and Data	79
Table 4.3 : EDF ac-Cable Data and Provenance	85
Table 5.1 : Comparison of numerical performance.....	115

LIST OF FIGURES

Figure 2-1 : Single-phase line segment.	11
Figure 2-2 : Ampere's law on conductor I	15
Figure 2-3 : Trajectory $ABCD$ A and surface S unfolded.	15
Figure 2-4 : Gaussian surface $S' = S + S_1 + S_2$	16
Figure 2-5 : Multiconductor line segment. Application of Faraday's law.	18
Figure 2-6 : Multiconductor line segment. Application of Ampere's law.	22
Figure 2-7 : Multiconductor transmission line segment of length L	28
Figure 2-8 : Circuit representation of multiconductor traveling-wave line model.	29
Figure 2-9 : PI line model.	31
Figure 3-1 : Traveling wave concept.	33
Figure 3-2 : CP model circuitual representation.	34
Figure 3-3 : RTWB ac 3-phase cable layout.	48
Figure 3-5 : RTWB ac 3-phase cable. Voltage waveforms at the sending end of the cores, comparison with the CP model.	49
Figure 3-6 : RTWB ac 3-phase cable. Voltage waveforms at the receiving end of the cores, comparison with the CP model.	49
Figure 3-7 : RTWB ac 3-phase cable. Voltage waveforms at the sending end of the sheaths, comparison with the CP model. Insert; close up of the y and x axis.	50
Figure 3-8 : RTWB ac 3-phase cable. Voltage waveforms at the receiving end of the sheaths, comparison with the CP model.	50
Figure 3-9 : CP 3-phase aerial line circuit layout.	51
Figure 3-10 : CP 3-phase aerial line test circuit.	52
Figure 3-11 : CP 3-phase aerial line voltage waveform at phase b.	52
Figure 3-12 : RTWB 6-phase underground cable layout.	53

Figure 3-13 : RTWB 6-phase underground cable test circuit.	54
Figure 3-14 : RTWB 6-phase underground cable voltage waveform at receiving end of phase 1.	54
Figure 3-15 : Transmission line configuration.	55
Figure 3-16 : Transmission network layout and data.	56
Figure 3-17 : Transmission network voltage waveform at phase b.	57
Figure 3-18 : Transmission network voltage waveform at phase b, close up.	57
Figure 3-19 : Double circuit aerial line energizing plant.	58
Figure 3-20 : Double circuit aerial line layout.	58
Figure 3-21 : Double circuit aerial line voltage waveforms at the consumption plant side of circuit 1, subplots correspond to phase a, b, c, close up on phase a, b and c, respectively. WB solid line, FD dashed line.	60
Figure 3-22 : Double circuit aerial line current waveforms at the consumption plant side of circuit 1, subplots correspond to phase a, b, c, close up on phase a, b and c, respectively. WB solid line, FD dashed line.	61
Figure 3-23 : BC HYDRO 9-phase aerial line layout.	62
Figure 3-24 : BC HYDRO 9-phase aerial line test circuit, WB vs FD.	63
Figure 3-25 : BC HYDRO 9-phase aerial line voltage waveform at the receiving end of the 5 th phase, WB vs FD.	63
Figure 4-1 : RTE dc-cable system's layout.	74
Figure 4-2 : RTE dc-cable real part of Y_c diagonal elements. Solid line for results with 10 SPD, dashed line for results with 20 SPD.	75
Figure 4-3 : RTE dc-cable real part of H diagonal elements. Solid line for results with 10 SPD, dashed line for results with 20 SPD.	75
Figure 4-4 : RTE dc-cable test circuit (numerical test only).	76
Figure 4-5 : RTE dc-cable current waveforms at the sending end. Solid line are results with 20 SPD, dashed line are results with 10 SPD.	76

Figure 4-6: RTE dc-cable passivity test results for 10 SPD case.....	77
Figure 4-7: RTE dc-cable passivity test results for 10 SPD case close up.....	77
Figure 4-8: RTE dc-cable passivity test results for 20 SPD case.....	77
Figure 4-9: Mader ac-distribution 12-phase cable layout.	79
Figure 4-10: Mader ac-distribution 12-phase cable test circuit.....	79
Figure 4-11: Mader ac-distribution 12-phase cable. Real part of element (1,2) in matrix \mathbf{H} fitted with 2 poles. Solid line is the original value, dashed line is the fitted one.	80
Figure 4-12: Mader ac-distribution 12-phase cable. Passivity test result for a 0.01 level of absolute approximation error.	81
Figure 4-13: Mader ac-distribution 12-phase. Passivity test results close-up for the 0.01 level of absolute fitting.....	81
Figure 4-14: Mader ac-distribution 12-phase cable. Real part of element (1,2) of \mathbf{H} matrix fitted with 4 poles. Solid line is for original function values, dashed line is for fitted values.	82
Figure 4-15: Mader ac-distribution 12-phase cable. Passivity test results close-up for the 0.001 level of absolute fitting.....	82
Figure 4-16: Mader ac-distribution 12-phase cable. Sending end current waveforms. Solid line corresponds to the 0.01 error level approximation case, dashed line is for the 0.001 error-level case.	83
Figure 4-17: EDF ac-cable layout.	85
Figure 4-18: EDF ac-cable traditional grouping case passivity test results.	85
Figure 4-19: EDF ac-cable no grouping case passivity test results.....	86
Figure 4-20: EDF ac-cable, modal propagation function magnitudes.	87
Figure 4-21: EDF ac-cable test circuit.	87
Figure 4-22: EDF ac-cable nonpassive case receiving end voltage waveforms.	88
Figure 4-23: EDF ac-cable passive case receiving end voltage waveforms.	88
Figure 4-24 : BC HYDRO 9-phase aerial line layout, passivity study.	89

Figure 4-25 : BC HYDRO 9-phase aerial line. Voltage waveforms at the receiving end of circuit 1 nonpassive case.	89
Figure 4-26: BC HYDRO 9-phase aerial line traditional grouping case passivity test results.	89
Figure 4-27: BC HYDRO 9-phase aerial line traditional grouping case, passivity test results close-up.	90
Figure 4-28: BC HYDRO 9-phase aerial line, proposed grouping case, passivity test results, close-up around the low-frequency range.	91
Figure 4-29: BC HYDRO 9-phase aerial line, proposed grouping case, passivity test results, close-up.	91
Figure 4-30 : BC HYDRO 9-phase aerial line. Voltage waveforms at the receiving end of circuit 1 passive case.	92
Figure 4-31: BC HYDRO 9-phase aerial line, modal propagation functions magnitudes.	92
Figure 5-1 : RTWB 3-phase aerial line configuration.	106
Figure 5-2 : RTWB 3-phase aerial line test circuit.	107
Figure 5-3 : RTWB 3-phase aerial line receiving end voltage waveforms.	107
Figure 5-4 : RTWB 3-phase aerial line receiving end voltage relative errors.	108
Figure 5-5 : RTWB 3-phase aerial line receiving end current waveforms.	108
Figure 5-6 : RTWB 3-phase aerial line receiving end current relative errors.	109
Figure 5-7 : RTWB 2-phase underground cable layout.	110
Figure 5-8 : RTWB 2-phase underground cable test circuit.	110
Figure 5-9 : RTWB 2-phase underground cable receiving-end voltage waveforms.	111
Figure 5-10 : RTWB 2-phase underground cable receiving-end voltage relative differences.	111
Figure 5-11 : RTWB 2-phase underground cable receiving-end current waveforms.	112
Figure 5-12 : RTWB 2-phase underground cable receiving-end current relative differences.	112
Figure 5-13: RTWB 3-phase cable-core receiving-end voltage waveforms.	113

Figure 5-14: RTWB 3-phase cable-sheath receiving-end voltage waveforms.....	114
Figure 5-15: RTWB 3-phase cable-core relative differences.....	114
Figure 5-16: RTWB 3-phase cable-sheath relative differences.	114
Figure 6-1: Discrete time-domain Norton equivalent of a multiconductor line.....	120
Figure 6-2 : Flow diagram for RTWB implementation and its interface with SSN.	122
Figure 6-3 : Integer multiple buffer scheme.....	125
Figure 6-4 : Interpolation buffer scheme.....	125
Figure 6-5 : RTWB ac 3-phase cable sending-end core-voltages, real-time test. Solid line for EMTP-RV results dashed line for RTWB results.	129
Figure 6-6 : RTWB ac 3-phase cable sending-end sheath-voltages, real-time test. Solid line for EMTP-RV results dashed line for RTWB results.	130
Figure 6-7 : RTWB ac 3-phase cable receiving-end core-voltages, real-time test. Solid line for EMTP-RV results dashed line for RTWB results.	130
Figure 6-8 : RTWB ac 3-phase cable receiving-end sheath-voltages, real-time test. Solid line for EMTP-RV results dashed line for RTWB results.	131
Figure 6-9 : RTWB ac 3-phase cable sending-end sheath-voltages, solid line simulation with a $1\mu\text{s}$ time step, dashed line simulation with a $10\mu\text{s}$ time step.	132
Figure 6-10 : BC HYDRO 9-phase aerial line test circuit, real-time test.	133
Figure 6-11 : BC HYDRO 9-phase aerial line circuit 1 receiving-end voltage-waveforms, real- time test. Solid line for EMTP-RV results dashed line for RTWB results.	133
Figure 6-12 : BC HYDRO 9-phase circuit 2 receiving-end voltage-waveforms, real-time test. Solid line for EMTP-RV results dashed line for RTWB results.	134
Figure 6-13 : BC HYDRO 9-phase circuit 3 receiving-end voltage-waveforms, real-time test. Solid line for EMTP-RV results dashed line for RTWB results.	134
Figure 6-14 : RTWB 6-phase cable voltage waveforms at the receiving end of phase a, real-time test. Solid line for EMTP-RV results dashed line for RTWB results.	136

Figure 6-15 : Transmission network voltage waveforms at Bus1, real-time test. Solid line for EMTP-RV results dashed line for RTWB results.	136
--	-----

LIST OF ACRONYMS AND ABBREVIATIONS

BPA	Bonneville Power Administration
CP	Constant Parameters
CTSS	Continuous Time State Space
DG	Distributed Generation
DTSS	Discrete Time State Space
EHV	Extra-High Voltage
EMTP	Electromagnetic Transients Program
EMTP-RV	Electromagnetic Transients Program-Restructured Version
EMTs	Electromagnetic Transients
FACTS	Flexible ac Transmission Systems
FD	Frequency Domain
FDQ	Frequency Domain Cable
FFD	Full-Frequency Dependent
HIL	Hardware in the Loop
HVDC	High-Voltage direct current
RES	Renewable Energy Sources
RTWB	Real-Time Wide Band
RTWB2B	Real-Time Wide Band 2 nd order Blocks
TEM	Transversal Electromagnetic
UHV	Ultra-High Voltage
ULM	Universal Line Model
VF	Vector fitting
WB	Wide Band

WVF Weighted Vector Fitting

LIST OF APPENDICES

Appendix-I

147

CHAPTER 1 INTRODUCTION

1.1 Electromagnetic Transient Analysis for Modern Power Systems

Modern Power Systems are rapidly growing in complexity and size as they continue to incorporate new technologies. As a result, the time required for their study becomes excessive. For instance, HVDC interconnections, SVC, STATCOM, FACT devices, among others, each time are more popular. Distributed-generation (DG) devices and renewable energy sources (RES) are also current examples of new trends in power systems.

The aforementioned components and techniques usually are connected to the network using power electronic converters, giving as result a constantly changing network containing a broad range of frequencies. This situation can also be present in the case of power system faults. During normal operation, constant load and topology, electromechanical and electromagnetic energy exchanges are normally below the equipment rates. While, on the other hand, under switching events or system disturbances, the energy exchanges subject the circuit to higher stresses resulting from excessive current or voltage variations. These events often lead to equipment degradation or even total loss. The prediction of overcurrents and overvoltages is the main objective of Electromagnetic Transient Analysis.

Power system utilities and consultants rely each time more on digital simulators to test and to design electrical networks and apparatuses based on Transient Analysis results. For this reason, the use of real-time simulators is becoming more recurrent nowadays. Real-time simulators allow to test and verify equipment without using actual real networks because of their Hardware-in-the-Loop (HIL) capabilities. These analysis tools can perform simulations in a fraction of the time needed by their off-line counterparts.

Reliable and efficient power-network component-models are needed for real-time and parallel simulations. Power transmission power lines and cables are very important elements since they can represent up to 90% of the components in the Power System and provide natural time-decoupling between subsystems allowing parallel simulation. Transmission lines are often very difficult to simulate with the required accuracy. Inaccurate line/cable models may result into: 1) System overvoltage is underestimated, causing an underrating of the tested equipment which next can be the cause of a major blackout. 2) System overvoltage is overestimated, giving

as result an overrating of the equipment with the consequent overexpense. Thus, for economical and safety reasons is important to perform studies with the most accurate and efficient line/cable models.

This thesis focuses on line/cable models which are accurate, numerical efficient and suitable for real-time simulations.

1.2 State of the Art in Power Line and Cable Modeling

Presently, real-time and off-line simulators employ two types of line models: the Constant Parameters (CP) [1] and the Frequency Dependent (FD) [2] ones. The former is based on the assumption of line parameters being frequency independent and it is highly efficient, computationally speaking. It also is capable of simulating aerial lines and underground and submarine cables. Nevertheless, the assumption of constant parameters is correct only for steady-state analysis. At transient state studies the CP model tends to overestimate voltage and current magnitudes, thus misrepresenting the transient phenomena mostly in underground cables where parameters are highly frequency dependent.

One of the most successful frequency-dependent line models perhaps was the FD-line one presented in [2]. The basic assumption in it is that modal transformations can be accurately attained through a real and constant matrix. The FD-line model is widely used because of its robustness. Its accuracy is also very good, except for cases involving underground and submarine cables, as well as highly asymmetric aerial lines. Recently, the FD line model has been reformulated to make it compatible with the Vector Fitting tool (VF) [3]. This results in a model with high numerical efficiency that is suitable for real-time simulations [4]. Since the late 1980s to present, a very active area of research has been the development of fully frequency dependent or wideband (WB) line models [3]-[7].

Nowadays, the most accepted WB model undoubtedly is the Universal Line Model (ULM) [5]. It is based on the traveling-wave principle and its parameters are obtained through the VF algorithm. ULM works well in most cases and, before the work being reported here, it was only available for off-line simulators. Nevertheless, the ULM still requires further development. In some situations one may not be able to achieve the desired accuracy with it or, if the fitting process delivers unstable poles, these have to be flipped to the stable region and this degrades its

accuracy. Moreover, there have been reports of cases where the fitting procedure fails to converge. Weighted Vector Fitting (WVF) [6] is a modification to VF that helps to overcome some of these problems and that can produce lower order realizations.

1.3 Problem Statement

For industrial-grade real-time simulators, the available line models are either of the constant parameters (CP) or of the frequency dependent (FD) class. CP line models are very efficient computationally speaking and are capable of simulating line and cables. However, this kind of model considers that line parameters are constant, *i.e.*, they don't vary with frequency. This assumption is correct only for steady-state analysis while, for transient analysis it is known that CP models tend to overestimate voltage and current magnitudes misrepresenting the transient phenomena mostly in underground cables where parameters are highly frequency dependent.

The FD line model is more accurate than the CP one since the former model takes into account the frequency dependence of line propagation functions. FD models work in the modal domain and perform the transformation between modal and phase domain by a single real constant transformation matrix. This feature makes the FD line model computationally efficient. Is also because of this feature that the model is inaccurate for simulating, highly-asymmetrical aerial-lines and underground and submarine cables.

Given the increasing use of underground/submarine cables for safety, environmental and economical reasons, the need for an accurate and reliable line/cable model, capable of performing simulations in real-time is evident. The lack of such model is thus the main motivation for the research reported in this thesis.

The Universal Line Model (ULM) or Wide Band (WB) line model is the most general, state-of-the-art line model presently available for off-line simulators. This model takes into account the full frequency dependence (FFD) of line parameters and works directly in the phase domain. This feature makes it highly accurate. At the same time also, its numerical efficiency is much lower than that of the CP line and FD line models.

Given the fact that the ULM is capable of accurately simulating aerial lines as well as insulated cables, its implementation in a real-time platform is highly attractive. However, real-time simulation imposes restrictions nonexistent in off-line simulations. In its current state the

ULM is not capable of completely meet those restrictions. It thus needs to be reformulated in order to meet the requirements imposed by real-time simulations. Furthermore, there are reports of cases where the ULM fails and results in unstable time-domain simulations [6] [7].

Thus, a major objective of this thesis is to overcome existing problems with the ULM. Other important objective is to achieve real-time performance while retaining accuracy and stability.

1.4 Thesis Objectives

General Objective

The general objective of this thesis is to formulate and to implement a full-frequency-dependent (FFD) line/cable model for real-time and off-line simulators. This implementation should overcome most of the remaining limitations of the ULM. Major focus of this thesis is on the numerical efficiency, the accuracy and the stability of the implemented ULM or WB line model.

Specific Objectives

The obtained line/cable model must be solved much faster (at least two times) than existing full-frequency-dependent models. For this reason numerical efficiency must be dramatically increased.

The obtained line/cable model must be accurate and deliver comparable results to those obtained with already existing models. Nevertheless, in this thesis an acceptable compromise between speed and accuracy is searched.

The obtained line/cable model must be suitable for implementation in real-time platforms as well as in off-line simulators.

The obtained line/cable model must be stable and passive for all simulations. It must increase its level of generalization to solve existing problematic cases.

1.5 Contributions of this thesis

Because the main goal of this research is to develop and implement a full-frequency-dependent line model capable of simulating aerial lines as well as underground/submarine cables

for a real-time platform with the additional feature of being able to be implemented in offline platforms. The already existing WB model implemented in EMTP-RV is taken as the basis to develop more stable and faster line/cable models that not only improve upon the computational performance of its predecessor at offline simulations, but that also overcomes real-time restrictions while preserving accuracy. Passivity, stability and causality in the proposed models are also improved by identifying and curing several drawbacks within the fitting stage of the model.

The WB model basically consists in three main stages 1) line parameters calculation, 2) rational fitting or obtaining rational models and 3) time-domain iteration or solving line model equations in time domain. This research deals mainly with stage number three where the original WB model is modified to achieve a substantially increase in computational efficiency. In a lesser degree, this thesis deals with stage two where the fitting process is analyzed to obtain passive, stable and causal models.

At the original ULM, the VF tool or its modification WVF is used to obtain rational fits of the characteristic admittance and propagation functions matrices. One advantage of using this tool is that it delivers accurate and compact rational models. Nevertheless, an important disadvantage of this technique is that it may produce complex-conjugate pairs of poles thus forcing state variables and related equations to be declared as complex, even if obtained poles are real. This results in a loss of numerical efficiency, since the handling of real variables as complex increases the number of required sums at least by a factor of two and the number of real multiplications by a factor of four. In addition, all of the added sums and multiplications are trivial; that is, sums of zeros and multiplications by zeros. It is shown in Chapter 5 that for the case of complex conjugate state variables, the two states from a conjugate pair convey the same information and the computation of these two is redundant. This information leads to the development of a model here denominated “first order blocks” or “first order realizations” model. The proposed modification enables achieving a gain of up to 7 times in computational speed. This model is first implemented in Simulink and in EMTP-RV for offline simulations and, in the OPAL-RT real-time platform, for real-time simulations. The real-time version of the model is further named RTWB for real-time WB line model and is the first of its kind being implemented in a cluster-based real-time simulator.

It is also shown in Chapter 5 that complex-conjugate states are naturally eliminated by their combination into a single state ruled by a second order differential equation. The application of this idea results in a model that is called here as “second order blocks” or “second order realizations.” This modification permits achieving a gain of up to 8 times in computational speed with respect to standard implementations of the original ULM. The new model is further implemented in Simulink and in EMTP-RV for offline simulations. Even though, the second orders block model is not implemented yet in a real-time platform, this can be done with relative ease. This second model is here on called RTWB2B for real-time WB 2nd order blocks model.

RTWB and RTWB2B are not only several times faster than they predecessor they also provide accurate simulations. This is supported through several tests included in Chapter 5.

One problem encountered when using VF is that this tool does not guarantees passivity and therefore neither causality nor stability of the obtained rational models, thus leading to unstable or erroneous time-domain results.

At Chapter 4 several cases are analyzed and used to draw and overcome realized steps inside the fitting stage of the line model that if not well addressed may lead to nonpassive, unstable, or noncausal rational models. Such steps are 1) mode grouping, 2) representation of initial characteristic admittance and propagation factors matrices and 3) number of poles or fitting accuracy. The passivity test proposed in [8] is used to test for passivity inside the obtained rational models.

A general accepted practice on the modeling of multiconductor lines is that modes with nearly equal time delays and angles must be grouped in a single delay group for the sake of numerical efficiency. It is shown at section 4.6.4 that the grouping of modes by taking into account angles and time delays only, can introduce stiffness into the fitting process ending up with a nonpassive, unstable and noncausal model. It is shown also in this section that by taking into account the mode magnitudes too, by means of a simple error comparison, the aforesaid problems are prevented.

It is also shown at Chapter 4 that by given a sufficiently large number of frequency points at the representation of the initial characteristic admittance and propagation matrices, nonpassivity problems can be avoided. The effect of the number of poles on passivity also is addressed at Chapter 4. It is reported there that the number of fitting poles is closely related to the

fitting error and that by increasing this number the fitting is improved and passivity violations are reduced to a small value as to obtain stable time-domain solutions.

The above mentioned three points are used as guidelines to avoid the lack of passivity in the obtained rational models, as well as to obtain accurate and stable time-domain simulations. These points are adopted with the models being proposed here. In consequence, these models are more stable than the original ULM. In sum the models proposed here not only are faster and accurate, but also are more stable than the original ULM.

CHAPTER 2 TRANSMISSION LINE ANALYSIS

Transmission line analysis has its basis on a pair of partial differential equations usually referred to as the Telegrapher's Equations. For a lossless multiconductor line these equations are stated as follows:

$$-\frac{\partial \mathbf{v}}{\partial x} = \mathbf{L}_0 \frac{\partial \mathbf{i}}{\partial t} \quad (2.1)$$

$$-\frac{\partial \mathbf{i}}{\partial x} = \mathbf{C}_0 \frac{\partial \mathbf{v}}{\partial t} \quad (2.2)$$

where \mathbf{v} and \mathbf{i} are the respective vectors of conductor voltages and conductor currents, \mathbf{L}_0 is the matrix of self and mutual inductances of the line conductors and \mathbf{C}_0 is the matrix of their self and mutual capacitances. Both, \mathbf{L}_0 and \mathbf{C}_0 are in per unit length units and are of order $N \times N$ for a line with N conductors.

For the lossy-line case, the transmission line equations are stated more conveniently in the frequency domain:

$$-\frac{d\mathbf{V}}{dx} = \mathbf{Z}\mathbf{I} \quad (2.3)$$

$$-\frac{d\mathbf{I}}{dx} = \mathbf{Y}\mathbf{V} \quad (2.4)$$

where \mathbf{V} and \mathbf{I} are the Fourier Transforms of \mathbf{v} and \mathbf{i} respectively, $\mathbf{Z} = \mathbf{R} + j\omega\mathbf{L}$ is the matrix of self and mutual impedances of the line conductors, and, $\mathbf{Y} = \mathbf{G} + j\omega\mathbf{C}$ is the matrix of their self and mutual admittances. Both matrices, \mathbf{Z} and \mathbf{Y} , are in per-unit length units.

The following equations often are used and correspond to an approximation of (2.3) and (2.4) obtained under the assumption of line-parameter matrices $\mathbf{L}, \mathbf{R}, \mathbf{C}$ and \mathbf{G} being independent of the frequency ω .

$$-\frac{\partial \mathbf{v}}{\partial x} = \mathbf{L} \frac{\partial \mathbf{i}}{\partial t} + \mathbf{R}\mathbf{i} \quad (2.5)$$

$$-\frac{\partial \mathbf{i}}{\partial x} = \mathbf{C} \frac{\partial \mathbf{v}}{\partial t} + \mathbf{G} \mathbf{v} \quad (2.6)$$

Nevertheless, the time domain equivalents of (2.3) and (2.4) should involve convolution operations. For instance, the following forms are due to Radulet, *et.al.* [9].

$$-\frac{\partial \mathbf{v}}{\partial x} = \mathbf{L}_0 \frac{\partial \mathbf{i}}{\partial t} + \frac{\partial}{\partial t} \int_0^t \mathbf{i}(\tau) \mathbf{r}'(t-\tau) d\tau \quad (2.7)$$

$$-\frac{\partial \mathbf{i}}{\partial x} = \mathbf{C}_0 \frac{\partial \mathbf{v}}{\partial t} + \frac{\partial}{\partial t} \int_0^t \mathbf{v}(\tau) \mathbf{g}'(t-\tau) d\tau \quad (2.8)$$

where \mathbf{L}_0 and \mathbf{C}_0 are as in (2.1) and (2.2), $\mathbf{r}'(t)$ and $\mathbf{g}'(t)$ are the respective matrices of transient resistances and transient conductances corresponding to the inverse Fourier transforms of

$$\mathbf{R}' = \mathbf{L} - \mathbf{L}_0 + \frac{\mathbf{R}}{j\omega}$$

$$\mathbf{G}' = \mathbf{C} - \mathbf{C}_0 + \frac{\mathbf{G}}{j\omega}$$

At most texts in the specialized literature, line equations usually are derived from well accepted circuit representations of transmission lines. Although this approach provides a rapid introduction to line analysis, it leaves out important aspects of the line transmission phenomena that are needed when developing a state of the art line model. Electromagnetic Theory, on the other hand, provides a complete description of line phenomena and this is the approach presented next.

2.1 Electromagnetic Basis of Line Theory

A transmission line essentially is a longitudinal array of parallel conductors. The purpose of this array is to guide electromagnetic (EM) waves along the line path. One basic assumption of Line Theory is that the transversal dimensions of a line (*i.e.*, conductor cross-sections and distances) are smaller than one fourth the shortest wavelength involved in the wave propagation phenomenon. For a lossless line, this assumption implies that the only spatial mode supported by

the line is the transversal electromagnetic (TEM) one; that is, the mode in which the electric and magnetic fields are transversal to the line path.

For the case of lossy lines including imperfect conductors, a longitudinal component of the electric field appears and is associated to charge movement. A non-transversal component of the magnetic field can as well be produced by asymmetric distributions of currents inside the line conductors. In spite of the presence of those non-transversal EM-field components, transmission line analysis is extended to lossy lines under the assumption of these components being of much smaller magnitudes than those of their transversal counterparts. It is thus said that wave propagation is in quasi-transversal electromagnetic (or quasi-TEM) mode.

2.1.1 Single-phase case: first line equation

A one-conductor, or single-phase, transmission line actually consists of two parallel conductors being electrically insulated from each other. One of these conductors is taken as the reference one assigning to it a 0 V potential value all along the line. From here on, the reference conductor is labeled as the conductor 0. Figure 2-1 depicts a segment of a single-phase transmission line made of two cylindrical conductors. The actual transversal shape of the conductors is irrelevant for the analysis that follows. Included is in Figure 2-1 the oriented trajectory or path $ABCD A$ which defines the rectangular surface S of width Δz . Faraday's Law being applied to the line segment states that the variations in the magnetic flux flowing through S will induce an electromotive force along the path $ABCD A$, that the magnitude of this force is proportional to the flux variation and that the force polarity is opposed to the flux changes. From the frequency-domain form of Faraday's Law:

$$\oint_{ABCD A} \mathbf{E} \cdot d\mathbf{l} = -j\omega \int_S \mathbf{B} \cdot d\mathbf{s} \quad (2.9)$$

The closed-path integral at the left hand side (LHS) of (2.9) is decomposed next as the sum of the four line integrals along segments AB , BC , CD and DA :

$$\oint_{ABCD A} \mathbf{E} \cdot d\mathbf{l} = \int_{AB} \mathbf{E} \cdot d\mathbf{l} + \int_{BC} \mathbf{E} \cdot d\mathbf{l} + \int_{CD} \mathbf{E} \cdot d\mathbf{l} + \int_{DA} \mathbf{E} \cdot d\mathbf{l} \quad (2.10)$$

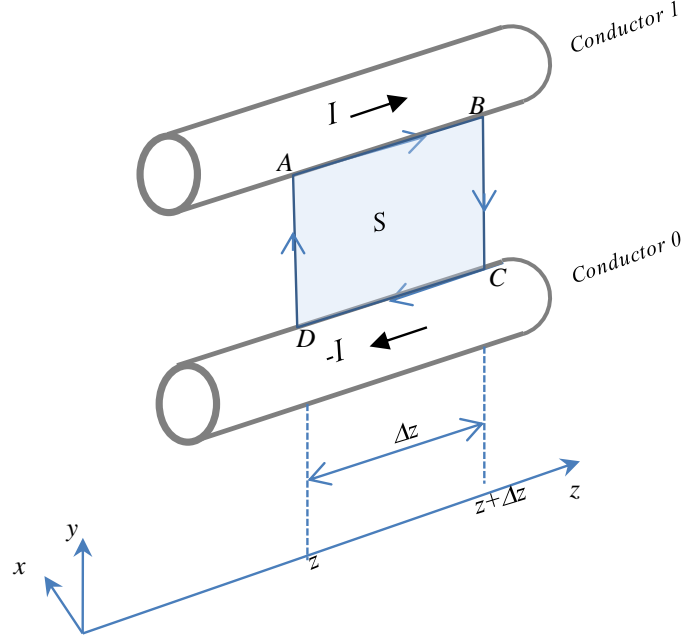


Figure 2-1 : Single-phase line segment.

a) Lossless line

In the case of an ideal line, the line integrals along segments AB and CD are zero, since there cannot be an electric field tangential to the surface of an ideal conductor. The line integral along segment BC corresponds to the voltage rise at point B with respect to point C . Let this voltage be denoted as $V(z + \Delta z)$. The line integral along segment DA represents the voltage drop at point A with respect to point D which is denoted as $-V(z)$. Hence:

$$\oint_{ABCD} \mathbf{E} \cdot d\mathbf{l} = V(z + \Delta z) - V(z) \quad (2.11)$$

Consider now the right hand side (RHS) of (2.9) and assume that the width of rectangular surface S is sufficiently small as to permit neglecting of \mathbf{B} -field variations along Δz ; hence:

$$-j\omega \int_S \mathbf{B} \cdot d\mathbf{s} = -j\omega \Delta z \int_{y_D}^{y_A} B dy \quad (2.12)$$

\mathbf{B} -field intensity is proportional to the current I flowing through conductor 1 and returning through conductor 0 . The following relation can thus be established:

$$\int_{y_D}^{y_A} B dy = L_0 I \quad (2.13)$$

The proportionality constant L_0 in (2.13) is identified as the ideal line inductance in per unit of length. The subscript “0” is to indicate that this inductance accounts for magnetic fields outside the conductors, as (2.11), (2.12) and (2.13) are replaced in (2.9) the following relation is obtained:

$$-\frac{V(z + \Delta z) - V(z)}{\Delta z} = j\omega L_0 I \quad (2.14)$$

On taking the limit $\Delta z \rightarrow 0$, and on applying the inverse Fourier transform:

$$-\frac{\partial v}{\partial z} = L_0 \frac{\partial i}{\partial t} \quad (2.15)$$

Expression (2.15) is the single-phase version of (2.1).

a) Lossy line

For the case of a non-ideal line with imperfect conductors, the line integrals along segments AB and CD at (2.10) cease to be zero. Nevertheless, Δz is taken sufficiently small as to permit neglecting \mathbf{E} -field variations along it. Expression (2.11) is thus modified as follows:

$$\oint_{ABCD} \mathbf{E} \cdot d\mathbf{l} = V(z + \Delta z) - V(z) + E_1 \Delta z - E_0 \Delta z \quad (2.16)$$

where E_1 and E_0 are the respective longitudinal \mathbf{E} -field components at segments AB and CD on the surfaces of conductors 1 and 0 . From Ohm's Law:

$$E_1 = \rho_1 J_1$$

$$E_0 = \rho_0 J_0$$

with ρ_1 and ρ_0 being conductor 1 and conductor 0 resistivities, and J_1 and J_0 are the respective current densities at segments AB and CD . Clearly both, E_1 and J_1 must be proportional to bulk

current I flowing through conductor 1 . By the same token, E_0 and J_0 must be proportional to bulk current $-I$ flowing through conductor 0 . The following relation can thus be established:

$$E_1 - E_0 = Z_c I \quad (2.17)$$

with the proportional constant being

$$Z_c = \rho_1 \frac{J_1}{I} - \rho_0 \frac{J_0}{(-I)}.$$

Since J_1 and J_0 generally are not in phase with I , Z_c is complex:

$$Z_c = R + j\omega L_c.$$

Z_c represents an impedance due to the magnetic flux penetration inside imperfect conductors 1 and 0 . Its real part R corresponds to the resistance of the two conductors in per unit of length. L_c is the internal inductance of the two conductors, also in per unit of length.

Let now expressions (2.12), (2.13), (2.15), and (2.16) be introduced in (2.9) and, after a rearrangement of terms:

$$-\frac{V(z + \Delta z) - V(z)}{\Delta z} = ZI \quad (2.18)$$

with

$$Z = R + j\omega L = R + j\omega(L_0 + L_c).$$

As the limit $\Delta z \rightarrow 0$ is applied in (2.18), the following expression is obtained:

$$-\frac{dV}{dz} = ZI. \quad (2.19)$$

Note that (2.19) is the single-phase version of (2.3). Note also that the line inductance parameter L is the sum of L_c due to magnetic flux penetration inside the imperfect conductors and L_0 due to magnetic flux outside at the insulation. The former term is strongly dependent on the frequency. As this dependence is neglected, the inverse Fourier transform of (2.19) yields:

$$-\frac{\partial v}{\partial z} = Ri + L \frac{\partial i}{\partial t}$$

2.1.2 Single-phase case: second line equation

Figure 2-2 depicts a line segment as the one in Figure 2-1. This time, however, the rectangular surface S , of width Δz and delimited by closed path $ABCD$, is wrapped around conductor I . Consider further that trajectories AB and CD overlap. Figure 2-3 shows the surface S and its contour $ABCD$ being extended. Ampere's Law being applied to this contour states that the circulation of the \mathbf{H} -field around $ABCD$ is equal to the current passing through S . This is stated mathematically as follows in the frequency domain:

$$\oint_{ABCD} \mathbf{H} \cdot d\mathbf{l} = (\sigma + j\omega\epsilon) \iint_S \mathbf{E} \cdot d\mathbf{s} \quad (2.20)$$

where σ is the conductivity of the insulating material between the line conductors and ϵ is its electric permittivity. The LHS integral of (2.20) is now decomposed in four terms:

$$\oint_{ABCD} \mathbf{H} \cdot d\mathbf{l} = \int_{AB} \mathbf{H} \cdot d\mathbf{l} + \oint_{BC} \mathbf{H} \cdot d\mathbf{l} + \int_{CD} \mathbf{H} \cdot d\mathbf{l} + \oint_{DA} \mathbf{H} \cdot d\mathbf{l} \quad (2.21)$$

Since trajectories AB and CD are made to coincide in Figure 2-2 and one runs opposite to the other, the first and the third terms at the RHS of (2.21) cancel each other. Note in addition that points B and C coincide, same as D and A . It is for this reason that the second and the fourth terms on the RHS of (2.21) are closed integrals. As Ampere's Law is applied to the second term, the result is $-I(z + \Delta z)$. The application of this law to the fourth term yields $I(z)$. In sum:

$$\oint_{ABCD} \mathbf{H} \cdot d\mathbf{l} = I(z) - I(z + \Delta z) \quad (2.22)$$

Let the RHS of (2.20) be considered now. Figure 2-4 illustrates a closed surface S' formed by surface S from Figure 2-2 and Figure 2-3 being wrapped around conductor I , and by the two flat and lateral covers S_1 and S_2 . If conductor I is perfect, the \mathbf{E} -field passing through S_1 and S_2 is zero and the integral on the RHS of (2.20) can be replaced by the closed integral through S' :

$$\iint_S \mathbf{E} \cdot d\mathbf{s} = \oiint_{S'} \mathbf{E} \cdot d\mathbf{s} \quad (2.23)$$

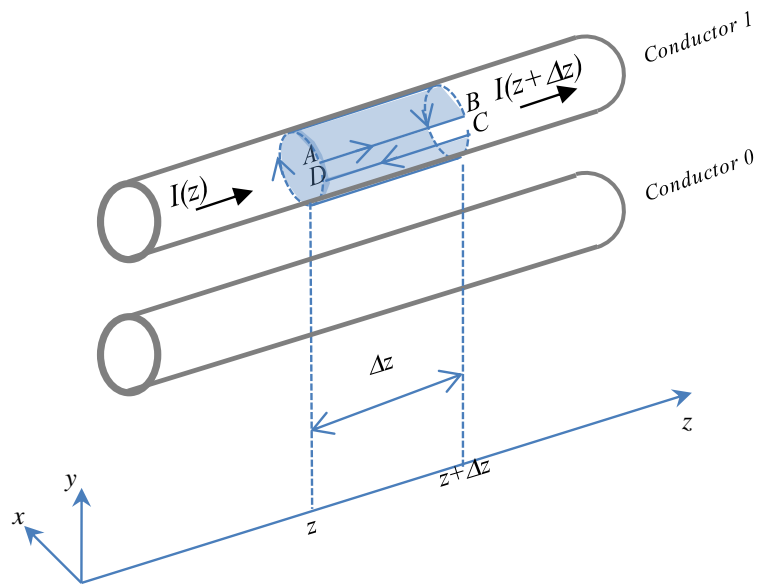


Figure 2-2 : Ampere's law on conductor I .

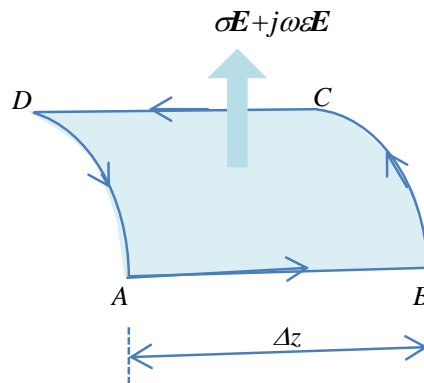


Figure 2-3 : Trajectory $ABCD$ A and surface S unfolded.

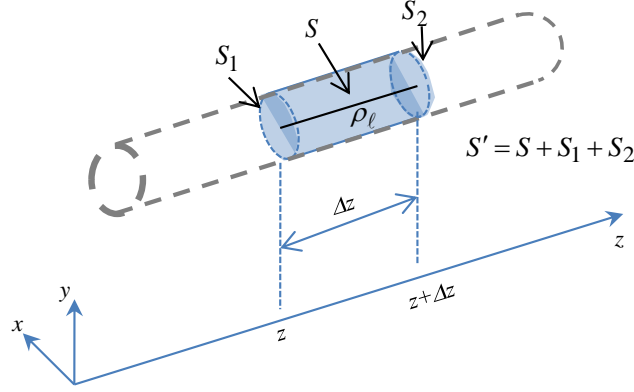


Figure 2-4 : Gaussian surface $S' = S + S_1 + S_2$.

When conductor I is imperfect, but still a good conductor, the \mathbf{E} -field at S_1 and S_2 is negligible as compared to that at S and expression (2.23) is accurate. On applying Gauss' Law in (2.23)

$$\iint_S \mathbf{E} \cdot d\mathbf{s} = \frac{Q_{enc}}{\epsilon}$$

With Q_{enc} being the total electric charge inside S' . It is possible to think of Q_{enc} as a linear charge density q_l distributed along Δz . By being Δz short enough, q_l can be considered constant and

$$\iint_S \mathbf{E} \cdot d\mathbf{s} = \frac{\Delta z q_l}{\epsilon} \quad (2.24)$$

q_l is further related to V , the voltage of conductor I with respect to conductor 0 , as follows

$$q_l = CV \quad (2.25)$$

where C is the line capacitance in per unit length.

a) Lossless line

Let be assumed in (2.20) that the line insulation is perfect (*i.e.*, $\sigma=0$). The introduction of (2.22), (2.24) and (2.25) into (2.20) yields:

$$-\frac{I(z+\Delta z)}{\Delta z} = j\omega CV \quad (2.26)$$

Further application of the limit $\Delta z \rightarrow 0$ and of the inverse Fourier transform in (2.26) results in the second Telegrapher equation:

$$-\frac{\partial i}{\partial z} = C \frac{\partial v}{\partial t} \quad (2.27)$$

b) Lossy line

Consider now that the line insulation presents a certain amount of conductivity ($\sigma>0$). As (2.22), (2.24) and (2.25) are replaced in (2.20) one obtains:

$$-\frac{I(z+\Delta z)}{\Delta z} = (G + j\omega C)V \quad (2.28)$$

where

$$G = \frac{\sigma}{\varepsilon}$$

is the conductance in per unit length. On taking the limit $\Delta z \rightarrow 0$

$$-\frac{dI}{dz} = YV \quad (2.29)$$

with $Y = G + j\omega C$ being the line admittance in per unit length. On neglecting the frequency dependence of G and C expression (2.29) can be approximated as follows:

$$-\frac{\partial i}{\partial z} = Gv + C \frac{\partial v}{\partial t}$$

2.1.3 Multiconductor case: first line equation

Figure 2-5 depicts a short segment of a multiconductor line formed by N conductors plus the reference one labeled as 0. Note in the figure the oriented trajectory $ABCD$ defining the

rectangular area S_i of width Δz . Segment AB runs along the surface of the i th conductor, with $i=1,2,\dots,N$. Segment CD runs along conductor 0. As Kirchhoff's currents law is applied in Figure 2-5, it follows that:

$$I_0 = -\sum_{k=1}^N I_k \quad (2.30)$$

Let the frequency-domain form of Faraday's law be applied to trajectory $ABCD$ in Figure 2-5:

$$\oint_{ABCD} \mathbf{E} \cdot d\mathbf{l} = -j\omega\Phi_i \quad (2.31)$$

with Φ_i being the total magnetic flux through surface S_i produced by currents I_0, I_1, \dots, I_N . This total flux can be considered as composed by N partial fluxes:

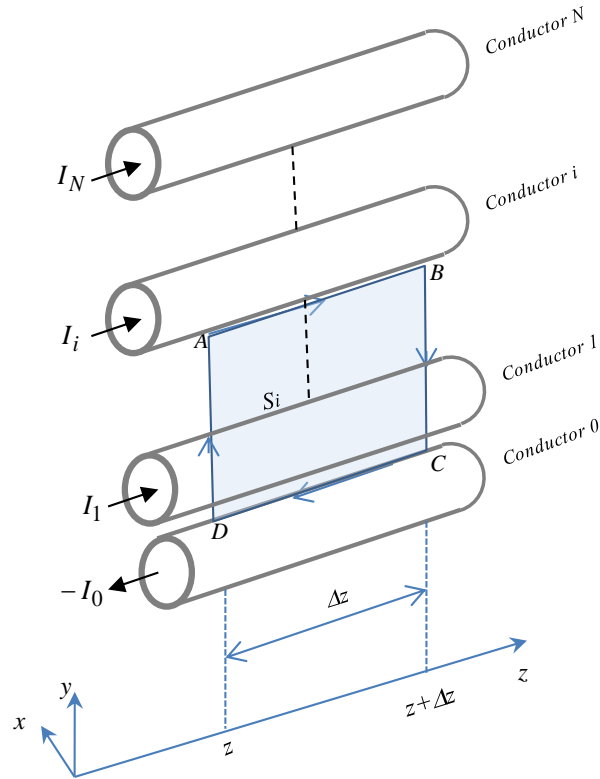


Figure 2-5 : Multiconductor line segment. Application of Faraday's law.

$$\Phi_i = \sum_{k=1}^N \phi_{i,k}$$

where $\phi_{i,k}$ is the k th partial flux produced by current I_k on conductor k , along with its return current $-I_k$ on conductor 0 . Moreover, as each partial flux ϕ_k is proportional to its associated current I_k :

$$\Phi_i = \Delta z \sum_{k=1}^N L_{0i,k} I_k \quad (2.32)$$

where the k th proportionality constant $L_{0i,k}$ is referred to as the mutual inductance (in per unit of length) between conductors i and k , or as the self inductance of conductor i when $i=k$. Note in (2.32) that the assumption has been made as to Δz being sufficiently small for neglecting variations of I_k and $\phi_{i,k}$ along the z -axis.

a) Lossless line

Consider the line integral on the LHS of (2.31) and its expansion as in (2.10):

$$\oint_{ABCD} \mathbf{E} \cdot d\mathbf{l} = \int_{AB} \mathbf{E} \cdot d\mathbf{l} + \int_{BC} \mathbf{E} \cdot d\mathbf{l} + \int_{CD} \mathbf{E} \cdot d\mathbf{l} + \int_{DA} \mathbf{E} \cdot d\mathbf{l} \quad (2.33)$$

Since conductors 0 and i are ideal, the integrals along AB and CD are zero, and the other two integrals amount to the voltage difference between points B and A on conductor i , both being referred to conductor 0 :

$$\oint_{ABCD} \mathbf{E} \cdot d\mathbf{l} = V_i(z + \Delta z) - V_i(z) \quad (2.34)$$

As (2.33) and (2.34) are introduced in (2.32), and the limit $\Delta z \rightarrow 0$ is taken, the following expression is obtained:

$$-\frac{dV_i}{dz} = j\omega \sum_{k=1}^N L_{0i,k} I_k; \quad i = 1, 2, \dots, N$$

or, in matrix-vector form:

$$-\frac{dV}{dz} = j\omega \mathbf{L}_0 \mathbf{I} \quad (2.35)$$

where \mathbf{L}_0 is the matrix of line inductances (in *p.u.l.* units)

$$\mathbf{L}_0 = \begin{bmatrix} L_{01,1} & \cdots & L_{01,N} \\ \vdots & \ddots & \vdots \\ L_{0N,1} & \cdots & L_{0N,N} \end{bmatrix}$$

and V and I are the respective vectors of voltages and of currents at the N line conductors

$$\mathbf{V} = \begin{bmatrix} V_1 \\ \vdots \\ V_N \end{bmatrix}, \quad \mathbf{I} = \begin{bmatrix} I_1 \\ \vdots \\ I_N \end{bmatrix}.$$

Finally, application of the inverse Fourier transform in (2.35) yields (2.1); that is, the first of the Telegrapher Equations for multiconductor lines:

$$-\frac{\partial v}{\partial z} = \mathbf{L}_0 \frac{\partial \mathbf{i}}{\partial t}$$

b) Lossy line

Consider again the line integral on the LHS of (2.31) and its expansion. The values for line integrals along segments BC and DA have been previously established as $V(z + \Delta z)$ and $-V(z)$, respectively. As conductors 0 and 1 are not considered ideal any longer, the \mathbf{E} -fields along segments AB and CD are different from zero; still though, Δz is taken sufficiently small to neglect their variations with respect to z ; hence:

$$\oint_{ABCD} \mathbf{E} \cdot d\mathbf{l} = V_i(z + \Delta z) - V_i(z) + E_{AB}\Delta z + E_{CD}\Delta z \quad (2.36)$$

Since E_{AB} is the value of the \mathbf{E} -field along conductor i , this value must be proportional to current I_i :

$$E_{AB} = Z_{cnd_{i,i}} I_i; \quad i = 1, 2, \dots, N \quad (2.37)$$

The term E_{CD} , on the other hand, corresponds to the E -field along E_{CD} conductor 0 being taken as reference. According to (2.30), current I_0 is the sum of return currents $-I_1, -I_2, \dots, -I_N$. The value of E_{CD} is thus composed by N terms, each one being proportional to a return current:

$$E_{CD} = Z_{ref,i,1} I_1 + Z_{ref,i,2} I_2 + \dots + Z_{ref,i,N} I_N; \quad i = 1, 2, \dots, N \quad (2.38)$$

The application of (2.36), (2.37), (2.38) and (2.33) in (2.32), along with the limit $\Delta z \rightarrow 0$, results in:

$$-\frac{dV_i}{dz} = Z_{cnd,i,i} I_i + \sum_{k=1}^N Z_{ref,i,k} I_k + j\omega \sum_{k=1}^N L_{0i,k} I_k; \quad i = 1, 2, \dots, N \quad (2.39)$$

Expression (2.39) is further stated in matrix-vector form as follows:

$$-\frac{dV}{dz} = \mathbf{Z} \mathbf{I} \quad (2.40)$$

with

$$\mathbf{Z} = \mathbf{Z}_G + \mathbf{Z}_{cnd} + \mathbf{Z}_{ref}$$

and

$$\mathbf{Z}_G = j\omega \mathbf{L}_0,$$

$$\mathbf{Z}_{cnd} = \text{diag}(Z_{cnd,1}, Z_{cnd,2}, \dots, Z_{cnd,N}) = \mathbf{R} + j\omega \mathbf{L}_{cnd}$$

$$\mathbf{Z}_{ref} = \begin{bmatrix} Z_{ref1,1} & \cdots & Z_{ref1,N} \\ \vdots & \ddots & \vdots \\ Z_{refN,1} & \cdots & Z_{refN,N} \end{bmatrix}.$$

\mathbf{Z}_G often is called the matrix of geometric impedances as its elements depend, apart from the insulation permittivity, on the transversal line geometry [10].

2.1.4 Multiconductor case: second line equation

Consider the multiconductor line segment depicted in Figure 2-6 where the surface S defined by the closed trajectory $ABCD$ is wrapped around conductor i . In much the same way as in the single-phase case of subsection 2.1.2, Ampere's law is applied to $ABCD$:

$$\oint_{ABCD} \mathbf{H} \cdot d\mathbf{l} = (\sigma + j\omega\epsilon) \iint_S \mathbf{E} \cdot d\mathbf{s} \quad (2.41)$$

As in the single-phase case, the LHS of this expression amounts to the following currents difference:

$$\oint_{ABCD} \mathbf{H} \cdot d\mathbf{l} = I_i(z) - I_i(z + \Delta z) \quad (2.42)$$

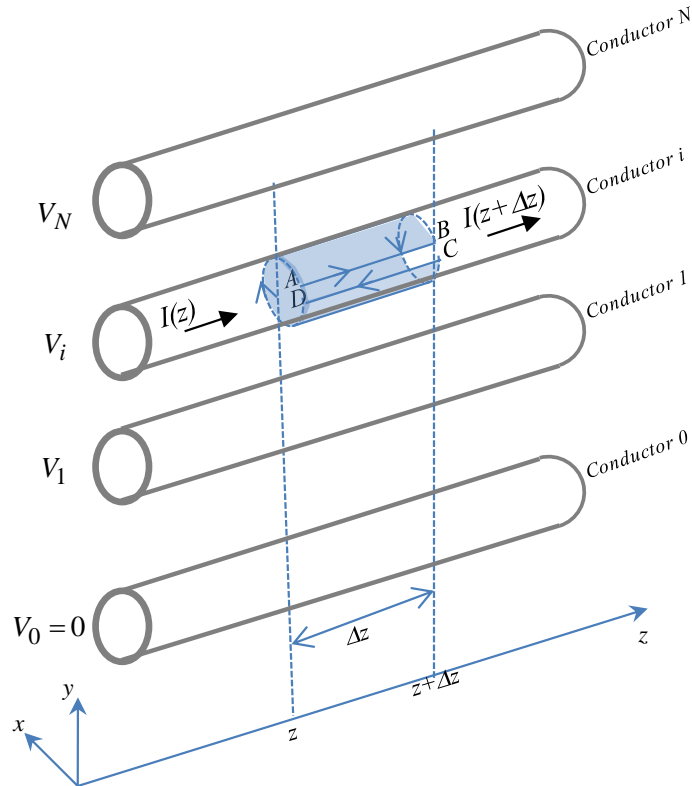


Figure 2-6 : Multiconductor line segment. Application of Ampere's law.

Under the assumption of a perfect or a good conductivity for conductor i :

$$\iint_S \mathbf{E} \cdot d\mathbf{s} = \frac{Q_{encl}}{\varepsilon} \quad (2.43)$$

The total charge being enclosed by the S-defined cylinder Q_{encl} can be considered composed by N partial charges:

$$Q_{encl} = q_1 + q_2 + \dots + q_i + \dots + q_N$$

with each component q_k having its reciprocal $-q_k$ at the k th conductor. Notice here that the reciprocal for q_i is at conductor 0 (the reference one). Each component q_k is, in addition, proportional to $V_i - V_k$, the voltage difference between conductors i and k , and the proportionality factor $\Delta z c_{i,k}$ is the capacitance between the two conductor segments i and k of length Δz . Hence:

$$Q_{encl} = \Delta z c_{i,i} V_i + \Delta z \sum_{\substack{k=1 \\ k \neq i}}^N c_{i,k} (V_i - V_k)$$

where $c_{i,i} = c_{i,0}$. This last expression is further arranged as follows:

$$Q_{encl} = \Delta z \sum_{k=1}^N C_{i,k} V_k \quad (2.44)$$

with

$$C_{i,k} = \begin{cases} -c_{i,k} & i \neq k \\ \sum_{m=1}^N c_{i,m} & i = k \end{cases}$$

The introduction of (2.42), (2.43) and (2.44) into (2.41) yields

$$\frac{I_i(z) - I_i(z + \Delta z)}{\Delta z} = \left(\frac{\sigma}{\varepsilon} + j\omega \right) \sum_{k=1}^N C_{i,k} V_k \quad i = 1, 2, \dots, N$$

Application of the limit $\Delta z \rightarrow 0$ results in:

$$-\frac{dI_i}{dz} = \sum_{k=1}^N G_{i,k} V_k + j\omega \sum_{k=1}^N C_{i,k} V_k; \quad i = 1, 2, \dots, N \quad (2.45)$$

where $G_{i,k} = (\sigma/\varepsilon)C_{i,k}$ is the admittance *p.u.l.* between conductors i and k . This is in case that the line dielectric is imperfect. Expression (2.45) is put in matrix form as follows:

$$-\frac{d\mathbf{I}}{dz} = \mathbf{Y}\mathbf{V} \quad (2.46)$$

with

$$\mathbf{Y} = \mathbf{G} + j\omega\mathbf{C}$$

where \mathbf{Y} is the matrix of line admittances, \mathbf{G} is the matrix of line conductances and \mathbf{C} is the matrix of line capacitances. All these matrices are of dimensions $N \times N$ and in *p.u.l.* units. Expression (2.46) is the frequency domain form of the second line equation for multiconductor lines. If line conductors are perfect, \mathbf{C} and \mathbf{G} at (2.46) are independent of frequency; thus, in the time domain:

$$-\frac{\partial \mathbf{i}}{\partial z} = \mathbf{G}\mathbf{v} + \mathbf{C} \frac{\partial \mathbf{v}}{\partial z} \quad (2.47)$$

As the line conductors are imperfect, but still good conductors, and their transversal dimensions are much smaller than the conductors distances (*i.e.*, less than ten times), one can consider \mathbf{C} and \mathbf{G} as being frequency independent and (2.47) represents an accurate approximation of (2.46) [10], [11].

On aerial power lines, the reference conductor is the ground plane whose transversal dimensions are not smaller than the conductor distances. Depending on the frequencies and ground resistivities involved, for these lines one could need to account for the frequency dependence of \mathbf{C} and \mathbf{G} [10]; nevertheless, in practical analysis these cases are rare.

2.2 Frequency-domain solution of multiconductor line equations

Equations (2.40) and (2.46) can be combined into a second order matrix equation involving only the vectors of currents

$$\frac{d^2 \mathbf{I}}{dz^2} = \mathbf{Y} \mathbf{Z} \mathbf{I} \quad (2.48)$$

or into one involving only the vectors of voltages

$$\frac{d^2 \mathbf{V}}{dz^2} = \mathbf{Y} \mathbf{Z} \mathbf{V} \quad (2.49)$$

For the case of single-phase lines, $\mathbf{I}, \mathbf{V}, \mathbf{Z}$ and \mathbf{Y} become scalar at (2.48) and at (2.49) and their solution is straightforward:

$$I(z) = C_1 \exp(-\gamma z) + C_2 \exp(\gamma z) \quad (2.50)$$

and

$$V(z) = Z_c [C_1 \exp(-\gamma z) - C_2 \exp(\gamma z)] \quad (2.51)$$

where

$$\gamma = \sqrt{Y Z} = \alpha + j\beta \quad (2.52)$$

is the line propagation constant, α is the attenuation, β is the phase-shift constant,

$$Z_c = Y^{-1} \gamma = \sqrt{Z/Y} \quad (2.53)$$

is the line characteristic impedance, and C_1 and C_2 are integration constants to be determined by the initial and boundary conditions of the line under analysis. The first term at the *RHS* of (2.50) represents a wave of current traveling forward with respect to the direction of the z -axis, while the second term represents a backward traveling wave of current. The inverse of Z_c in (2.53) is the line characteristic admittance

$$Y_c = \sqrt{Y/Z} \quad (2.54)$$

Solutions (2.50) and (2.51) for single-phase line equations are extended to the multiconductor line case through Modal Analysis [12],[13]. For this, it is postulated that the $\mathbf{Y} \mathbf{Z}$ matrix product is diagonalizable; that is, there exists a nonsingular matrix \mathbf{T} such that

$$\mathbf{YZT} = \mathbf{TA} \quad (2.55)$$

and \mathbf{A} is diagonal. The columns of \mathbf{T} are the eigenvectors of \mathbf{YZ} and are called the propagation modes of the multiconductor line [12],[13]

$$\mathbf{T} = [\mathbf{T}_1 | \mathbf{T}_2 | \dots | \mathbf{T}_N]$$

The diagonal elements of \mathbf{A} are the eigenvalues of \mathbf{YZ} .

$$\mathbf{A} = \text{diag}(\lambda_1, \lambda_2, \dots, \lambda_N)$$

Any analytic function f being applied to a diagonal matrix amounts to applying the function to its diagonal elements:

$$f(\mathbf{A}) = \begin{bmatrix} f(\lambda_1) & \cdots & 0 \\ \vdots & \ddots & \vdots \\ 0 & \cdots & f(\lambda_N) \end{bmatrix}$$

Application of an analytic function to \mathbf{YZ} is thus accomplished as follows [14]:

$$f(\mathbf{YZ}) = \mathbf{T}f(\mathbf{A})\mathbf{T}^{-1}$$

From all the above, the solutions to (2.50) and (2.51) in the multiconductor line case ($N > 1$) can be stated as follows:

$$\mathbf{I}(z) = \mathbf{C}_1 \exp(-\mathbf{\Gamma}z) + \mathbf{C}_2 \exp(\mathbf{\Gamma}z) \quad (2.56)$$

and

$$\mathbf{V}(z) = \mathbf{Z}_c [\mathbf{C}_1 \exp(-\mathbf{\Gamma}z) - \mathbf{C}_2 \exp(\mathbf{\Gamma}z)] \quad (2.57)$$

where

$$\sqrt{\mathbf{YZ}} = \mathbf{T}\sqrt{\mathbf{A}}\mathbf{T}^{-1}$$

$$\mathbf{Z}_c = \mathbf{Y}^{-1}\mathbf{\Gamma}$$

Γ being the so called propagation matrix, and C_1 and C_2 are vectors of integration constants. One point worth mentioning is that of the diagonal elements of modal matrix Γ_m being defined as follows:

$$\Gamma_m = +\sqrt{YZ} = \begin{bmatrix} \gamma_1 & \cdots & 0 \\ \vdots & \ddots & \vdots \\ 0 & \cdots & \gamma_N \end{bmatrix}$$

with

$$\gamma_i = +\sqrt{\lambda_i} = \alpha_i + j\beta_i; \quad i = 1, 2, \dots, N$$

Here the plus sign at the two expressions above indicates the root with the positive real part. The terms $\gamma_1, \gamma_2, \dots, \gamma_N$ correspond to the propagation constants of the corresponding propagation modes (or columns of T). Moreover, α_i is the attenuation constant of the i th mode and β_i is its phase-shift constant which is related to the mode velocity v_i as follows:

$$v_i = \frac{\omega}{\beta_i}$$

2.3 Two-Port Line Representations

Transmission line models can be constructed on the basis of solutions (2.56) and (2.57) of the multiconductor line equations. Figure 2-7 depicts a multiconductor line section of length L , with one of its ends at $x=0$ and the other at $x=L$. Let V_0 and V_L denote the voltage-vector values at the corresponding ends, and I_0 and I_L the current-vector injections at $x=0$ and at $x=L$, respectively. As solutions (2.56) and (2.57) are applied for $x=0$:

$$I(0) = I_0 = C_1 + C_2.$$

and

$$V(0) = V_0 = Z_c(C_1 - C_2).$$

Thus,

$$C_1 = \frac{1}{2}(I_0 + Y_c V_0) \quad (2.58)$$

and

$$C_2 = \frac{1}{2}(I_0 - Y_c V_0) \quad (2.59)$$

Solutions (2.48) and (2.49) are now applied to conditions at end $x = L$:

$$-I(L) = I_L = -\exp(-\Gamma L)C_1 - \exp(\Gamma L)C_2 \quad (2.60)$$

and

$$V(L) = V_L = Z_c [\exp(-\Gamma L)C_1 - \exp(\Gamma L)C_2]. \quad (2.61)$$

On left-multiplying (2.61) by Y_c :

$$Y_c V_L = \exp(-\Gamma L)C_1 - \exp(\Gamma L)C_2. \quad (2.62)$$

As (2.62) is subtracted from (2.60), and C_1 is replaced by its value at (2.58), one obtains:

$$I_L - Y_c V_L = -\exp(-\Gamma L)[I_0 + Y_c V_0].$$

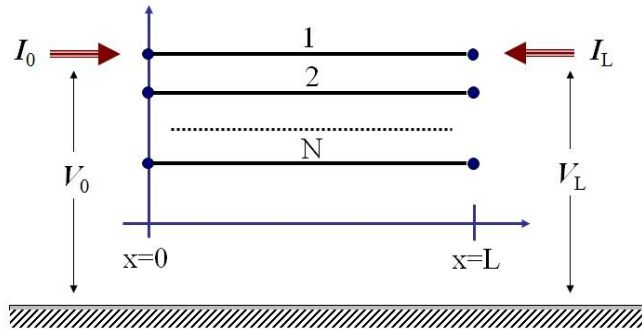


Figure 2-7 : Multiconductor transmission line segment of length L .

or

$$\mathbf{I}_L = \mathbf{Y}_c \mathbf{V}_L - \mathbf{H}[\mathbf{I}_0 + \mathbf{Y}_c \mathbf{V}_0] \quad (2.63)$$

where $\mathbf{H} = \exp(-\Gamma L)$ is the propagation functions matrix. Let now (2.60) and (2.62) be added and \mathbf{C}_2 be replaced by its value at (2.59):

$$\mathbf{I}_L + \mathbf{Y}_c \mathbf{V}_L = -\exp(-\Gamma L)[\mathbf{I}_0 - \mathbf{Y}_c \mathbf{V}_0]$$

or

$$\mathbf{I}_0 = \mathbf{Y}_c \mathbf{V}_0 - \mathbf{H}[\mathbf{I}_L + \mathbf{Y}_c \mathbf{V}_L] \quad (2.64)$$

Expressions (2.63) and (2.64) constitute a two-port model for multiconductor lines. This is based on traveling wave concepts. Recall that \mathbf{C}_1 and \mathbf{C}_2 in (2.58) and (2.59) represent forward and backward traveling waves, respectively. Most line models at the Electromagnetic Transients Program (EMTP) are based on these traveling-wave relations. Figure 2-8 provides the circuit representation for this model. Note that (2.63) corresponds to the model for the line end at $x = L$, while (2.64) corresponds to that for the line end at $x = 0$.

Given the fact that time domain results are easier to interpret than frequency domain ones, transient analysis is carried out in the time domain. Thus, time-domain solution of expressions (2.63) and (2.64) are of great importance and is given as follows [15]

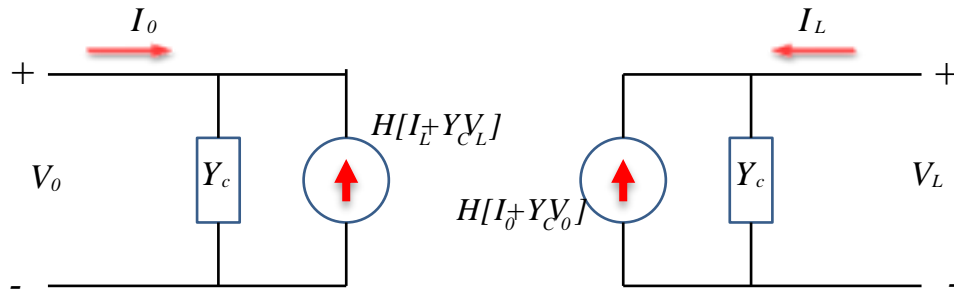


Figure 2-8 : Circuit representation of multiconductor traveling-wave line model.

$$\mathbf{i}_L - \mathbf{y}_c * \mathbf{v}_L = -\mathbf{h} * (\mathbf{i}_0 + \mathbf{y}_c * \mathbf{v}_0) \quad (2.65)$$

$$\mathbf{i}_0 - \mathbf{y}_c * \mathbf{v}_0 = -\mathbf{h} * (\mathbf{i}_L + \mathbf{y}_c * \mathbf{v}_L), \quad (2.66)$$

where the symbol $*$ indicates convolution. Expressions (2.65) and (2.66) are the solution to the telegrapher equations in the time domain.

As expressions (2.60) and (2.61) are combined in different ways, various other two-port models are obtained. Some of the most important models are enlisted as follows.

1. Nodal line model:

$$\begin{bmatrix} \mathbf{I}_0 \\ \mathbf{I}_L \end{bmatrix} = \begin{bmatrix} \mathbf{A} & \mathbf{B} \\ \mathbf{B} & \mathbf{A} \end{bmatrix} \begin{bmatrix} \mathbf{V}_0 \\ \mathbf{V}_L \end{bmatrix}$$

with

$$\mathbf{A} = \coth(\mathbf{I}L)\mathbf{Y}_c \text{ and } \mathbf{B} = -\operatorname{cosech}(\mathbf{I}L)\mathbf{Y}_c$$

2. ABCD parameters line model:

$$\begin{bmatrix} \mathbf{V}_0 \\ \mathbf{I}_0 \end{bmatrix} = \begin{bmatrix} \mathbf{A} & \mathbf{B} \\ \mathbf{C} & \mathbf{D} \end{bmatrix} \begin{bmatrix} \mathbf{V}_L \\ \mathbf{I}_L \end{bmatrix}$$

with

$$\mathbf{A} = \cosh^T(\mathbf{I}L)$$

$$\mathbf{B} = -\mathbf{Z}_c \sinh(\mathbf{I}L)$$

$$\mathbf{C} = \sinh(\mathbf{I}L)\mathbf{Y}_c$$

$$\mathbf{D} = -\cosh(\mathbf{I}L)$$

3. Exact PI line model (see Figure 2-9):

$$\begin{bmatrix} \mathbf{V}_0 \\ \mathbf{I}_0 \end{bmatrix} = \begin{bmatrix} \mathbf{U} + \mathbf{Z}'\mathbf{Y}'/2 & -\mathbf{Z}' \\ \mathbf{Y}'[\mathbf{U} + \mathbf{Z}'\mathbf{Y}'/4] & -[\mathbf{U} + \mathbf{Z}'\mathbf{Y}'/2] \end{bmatrix} \begin{bmatrix} \mathbf{V}_L \\ \mathbf{I}_L \end{bmatrix}$$

with

$$\mathbf{Z}' = \mathbf{Z}_c \sinh(\mathbf{\Gamma}L)$$

$$\mathbf{Y}' = 2 \tanh(\mathbf{\Gamma}L/2) \mathbf{Y}_c$$

and \mathbf{U} the identity matrix.

4. Nominal PI line model:

When the line length is much smaller than one quarter of the shortest wavelength involved in the analysis, the following approximations can be used at the circuit in Figure 2-9

$$\mathbf{Z}' \cong \mathbf{Z}L$$

$$\mathbf{Y}' \cong \mathbf{Y}L/2$$

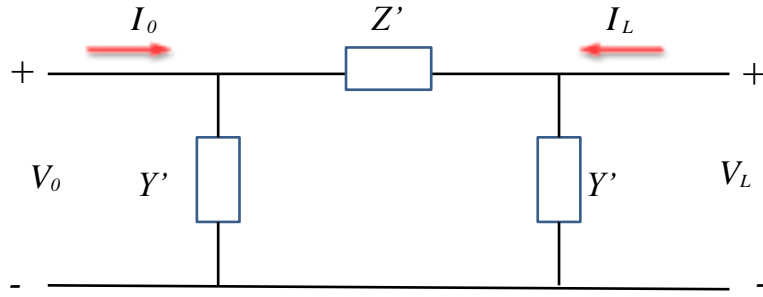


Figure 2-9 : PI line model.

2.4 Remarks

Transmission Line Theory is based on the Telegrapher's Equations and these are derived from Electromagnetic Theory. The connection between these two theories is considered here as essential for the purposes of this thesis. At most texts in the specialized literature, line equations are derived from well-established circuit representations of lines. Although this approach provides a rapid introduction to the subject, it leaves out important concepts that are necessary for developing state-of-the-art line and cable models. The treatment in this chapter is similar in some ways to the one at reference [17]. As opposed to the time-domain analysis in this reference, frequency-domain analysis is employed in this chapter and this permits a rigorous treatment and the removal of various simplifying assumptions.

CHAPTER 3 TRAVELLING-WAVE BASED LINE MODELS

3.1 Preamble

EMTP-type programs are nowadays the most used tool to simulate transient phenomena in electrical networks. The more important transmission line models implemented in these tools can be considered as traveling-wave types given the fact that such models solve equations which involve traveling waves with the form of (3.1) and (3.2).

The traveling wave concept as well as the generic time domain solution for lossless lines was first introduced by d'Alembert. If a line is consider lossless the resistance R and the conductance G in expressions (2.40) and (2.46) are zero and the general time solution is given as

$$v(x, t) = Z_s f_1(x - at) - Z_s f_2(x + at) \quad (3.1)$$

$$i(x, t) = f_1(x - at) + f_2(x + at), \quad (3.2)$$

where $Z_s = \sqrt{L/C}$ is the surge impedance, $a = 1/\sqrt{LC}$ is the phase velocity and, f_1 and f_2 are arbitrary functions . The physical interpretation of $f_1(x - at)$ is that of a wave travelling at a velocity a towards the receiving end and is called forward, or incident, wave and of $f_2(x + at)$ is that of a wave travelling away from the receiving end and is called backward, or reflected, wave [1]. Multiplying (3.2) by Z_s and adding it to (3.1) gives

$$v(x, t) + Z_s i(x, t) = 2Z_s f_1(x - at). \quad (3.3)$$

The meaning of (3.3) as well as that of a forward travelling wave can be explained as follows. If an observer travels along the line in a forward direction at velocity a . Then $(x - at)$ and consequently $(v + Z_s i)$ along the line will be constant for him. If the travel time to get from one side of the line to the other is

$$\tau = L/a = L\sqrt{LC} \quad (3.4)$$

where L is the length of the line, then the expression $(v + Z_s i)$ encountered by the observer when he leaves node 0 at time $t - \tau$ must still be the same when he arrives at node L at time t , see

Figure 3-1.

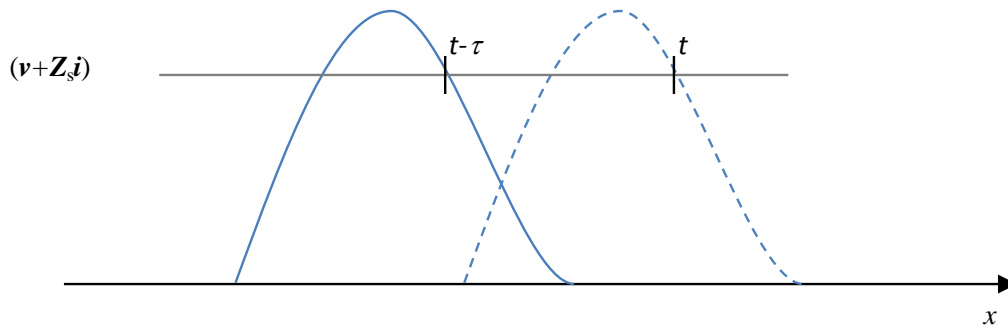


Figure 3-1 : Traveling wave concept.

In the following sections the most important line models implemented in EMTP-type programs are reviewed from a general point of view.

3.2 CP Model

The Constant Parameters (CP) model is classified as a frequency independent line model since its parameters are calculated at a single frequency thus the frequency dependence of the parameters is not taken in to account. The main advantage of this model is its computational speed. However, since the most noticeable effect of frequency dependence is on rounding the square pulses and reducing the height of spikes the CP model tends to exaggerate the effects of transient phenomena. And because this model does not take into consideration the full-frequency dependence of the parameters, it is not well suited for simulating most underground cable cases because cable parameters are strongly frequency dependent [7][16],[18],[20],[22],[24]

This model was one of the first transmission line models to be implemented in a real time platform because of its simplicity and due to the fact that provides the ability to naturally decouple both sides of the line [4][20]-[23], as will be shown further, allowing to simulate the network in two different processors speeding up the simulation to attain real time performance with small simulation time steps.

Consider equations (2.63) and (2.64) and let \mathbf{R} , \mathbf{G} , \mathbf{L} and \mathbf{C} be frequency independent which means constants along frequency. The time domain representation of afore mentioned equations under such circumstances is

$$\mathbf{i}_L - \mathbf{y}_c \mathbf{v}_L = -(\mathbf{i}_0(t - \tau) + \mathbf{y}_c \mathbf{v}_0(t - \tau)) = \mathbf{i}_{0,h} \quad (3.5)$$

$$\mathbf{i}_0 - \mathbf{y}_c \mathbf{v}_0 = -(\mathbf{i}_L(t - \tau) + \mathbf{y}_c \mathbf{v}_L(t - \tau)) = \mathbf{i}_{L,h} \quad (3.6)$$

which are similar to (2.65) and (2.66), respectively. Terms $\mathbf{i}_{0,h}$ and $\mathbf{i}_{L,h}$ are history currents [1]. The main difference between expressions (2.65), (2.66) and (3.5), (3.6) lies in the fact that (3.5) and (3.6) who represent the CP model do not contain convolutions making this model computational efficient. In the case of multi-phase lines, the model equations are diagonalized representing the line in the modal domain, that is, a matrix transformation is required to convert the quantities (voltages and currents) from the phase or physical domain to the decoupled modal domain [19]. Once in the modal domain the line is solved as N single phase lines.

Expressions (3.5) and (3.6) result in the circuit representation of the line given in Figure 3-2 where can be seeing that both sides of the line are time decoupled allowing network parallelization for real time simulations. This is a feature that all traveling-wave based models present.

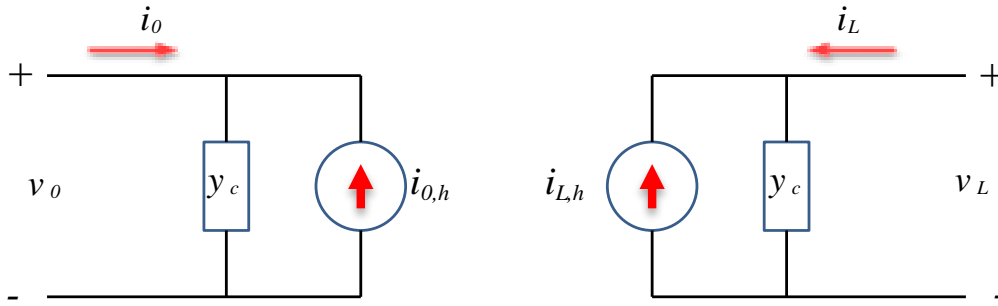


Figure 3-2 : CP model circuitual representation.

3.3 FD (Frequency Dependent) Line Model

One of the most widely used transmission line models in ETMP-type programs is the FD line model [2],[20]-[24]. This model is very accurate for single phase aerial lines and accurate for several multiphase aerial cases [20],[22],[24]. The FD model is also very efficient with its modal

domain solution. The line equations are diagonalized and the line is solved as N single phase lines [20],[22],[24]. Nevertheless, this model still has to solve convolutions at difference from the CP model which imposes a higher computational burden.

A fundamental limitation of this model is that it assumes that the transformation matrix that relates modal and phase quantities can be considered as real and constant within the frequency range of study. This assumption although valid in many cases can lead to inaccurate results in strongly asymmetrical line configurations and highly frequency dependent cases [20],[22],[24]. Examples of such cases are underground cables, multicircuit aerial configurations, and short circuit analysis, currents in short circuit scenarios are highly affected inside the FD model given the nature of the propagation functions matrix [20],[22],[24]. This is further explained in section 3.7. Also the model is sometimes unable to simulate low frequency coupling effects [19].

The FD line model is based in expressions (2.63) and (2.64) and its solution is made in the modal domain. Modal relations between voltages and currents are given as follows:

$$\mathbf{I} = \mathbf{T}_I \mathbf{I}_m, \quad (3.7)$$

$$\mathbf{V} = \mathbf{T}_V \mathbf{V}_m \quad (3.8)$$

where \mathbf{T}_I is the current transformation matrix whose columns are the eigenvectors or modes of the \mathbf{YZ} product. \mathbf{T}_V is the transformation matrix of voltages and sub-index m denotes modal quantities.

Applying relations (3.7) and (3.8) to expressions (2.63) and (2.64) these are expressed in modal domain

$$\mathbf{I}_{L,m} - \mathbf{Y}_{c,m} \mathbf{V}_{L,m} = -\mathbf{H}_m (\mathbf{I}_{0,m} + \mathbf{Y}_{c,m} \mathbf{V}_{0,m}) \quad (3.9)$$

$$\mathbf{I}_{0,m} - \mathbf{Y}_{c,m} \mathbf{V}_{0,m} = -\mathbf{H}_m (\mathbf{I}_{L,m} + \mathbf{Y}_{c,m} \mathbf{V}_{L,m}) \quad (3.10)$$

All matrices in expressions (3.9) and (3.10) are diagonal making the model very efficient. The time domain solution of the model is given by:

$$\mathbf{i}_{L,m} - \mathbf{y}_{c,m} * \mathbf{v}_{L,m} = -\mathbf{h}_m * (\mathbf{i}_{0,m} + \mathbf{y}_{c,m} * \mathbf{v}_{0,m}) \quad (3.11)$$

$$\mathbf{i}_{0,m} - \mathbf{y}_{c,m} * \mathbf{v}_{0,m} = -\mathbf{h}_m * (\mathbf{i}_{L,m} + \mathbf{y}_{c,m} * \mathbf{v}_{L,m}) \quad (3.12)$$

where convolutions are involved and for this reason this model is less efficient than the CP model but it is significantly more accurate. In the FD line model the characteristic impedance and the propagation functions matrices are approximated as rational functions using a Bode-type asymptotic fitting technique. One drawback of this technique is that it requires a much higher order of approximation compared to least squares identification methods such as Vector Fitting (VF) [3],[26]. Recently the FD model was reformulated in order to work with VF and it was found that the number of poles required by the model drops almost by half when using VF [4], however, the use of the Bode technique assures that the resulting rational functions will be passive since all poles and zeros are real, positive and simple (not complex conjugate). This is not the case with least squares methods [25], [26].

This model also allows network decoupling and was first implemented in a real-time simulator in the late 1980s [21]. These developments relied on specific purpose hardware, usually a digital signal processor (DSP) as reported in [27]. Two other important efforts in this direction were conducted in the mid-1990s [27],[28]. What these groups accomplished then was an FD line model running in real-time inside a dedicated processor that could be interfaced or included within a larger simulator. In 2010 the FD model was reformulated and implemented in a real-time simulator [4]. Although, this model was reformulated to increase its computational efficiency its main drawbacks are still present and a full-frequency-dependent line model is still required to simulate transient phenomena in underground cables as well as in multiconductor lines in real-time simulators.

3.4 FDQ Cable Model

The full frequency dependent cable (FDQ) model [29] solves the problem of a strongly frequency dependent transformation matrix by fitting the elements of this matrix with rational functions in the frequency domain using Bode-type asymptotic fitting [7],[20]. Then relations between phase domain and modal domain can be written as follows :

$$\mathbf{I} = \mathbf{T}'_I \mathbf{I}_m, \quad (3.13)$$

$$\mathbf{V} = \mathbf{T}'_V \mathbf{V}_m \quad (3.14)$$

where primed values are rational approximations of the transformation matrices \mathbf{T}_I and \mathbf{T}_V , respectively. Thus, the following convolutions are necessary in time domain [7],[20]:

$$\mathbf{i} = \mathbf{T}'_I(t) * \mathbf{i}_m, \quad (3.15)$$

$$\mathbf{v} = \mathbf{T}'_V(t) * \mathbf{v}_m \quad (3.16)$$

This model can give good results for cable simulations in low and high frequency ranges. However, in order to implement the recursive convolutions for the purpose of updating the history sources of equivalent model circuits, all elements of the frequency dependent propagation matrix, characteristic admittance matrix and modal transformation matrices (one for each frequency point) should be fitted with rational functions in the frequency domain. This results in a large number of operations in the time domain convolutions [7],[20] and in a high computational resources consumption making it unappealing for its implementation in real-time platforms. A difficulty of this model is that eigenvectors are defined only to a complex constant; that is, an eigenvector multiplied by any complex constant remains a valid eigenvector. This characteristic makes the synthesis of eigenvector as continuous frequency functions difficult complicating the fitting process. Thus, even the model gives accurate results for most cable systems it is in general not applicable to overhead lines because the modal decomposition is sometimes unstable. Hence, there is not a guarantee for all cases that the numerical stability of the rational functions for the frequency dependent transformation matrices can be satisfied. Even for cable cases it is not rare that this model numerically explodes in EMTP after a certain number of time steps [7].

At the moment of writing this thesis there are no reports concerning the implementation of this model in a real-time platform, mainly because of aforementioned drawbacks.

3.5 Universal Line Model (ULM)

The Universal Line Model (ULM) [5] also known as the WideBand (WB) model, is considered a phase domain line model at difference from CP, FD and FDQ that are considered as modal domain models. In order to overcome the problem of frequency dependent transformation matrices the WB model is directly formulated in the phase domain [5],[19]. In this model the propagation functions matrix \mathbf{H} as well as the characteristic admittance matrix \mathbf{Y}_c are directly fitted in the phase domain [5],[19] by the VF tool. The elements of \mathbf{Y}_c are smooth functions of frequency and can easily be fitted [5],[19].

Fitting of \mathbf{H} is more difficult because its elements contain modal contributions with different time delays. This problem is overcome by including modal time delays in the phase domain the model is based in the calculation of unknown residues when poles and time delays have been pre-calculated from the modes [5],[19]. All poles are assumed to contribute to the elements of \mathbf{H} .

This model gives highly accurate results for multiconductor aerial lines as well as for underground/submarine cables since it takes into account the full-frequency-dependence of line parameters. Nevertheless, there are some drawbacks with this model. Because the model works in the phase domain all matrices inside the model are full, thus its computational performance is low compared against the FD model. There are also some reports where the WB model fails and renders unstable simulations [6],[7],[26].

Despite of the afore mentioned drawbacks the WB is the state-of-the-art model implemented in EMTP-type programs and at the moment of writing this thesis there are no reports of this or any other full-frequency-dependent line model been implemented in a real-time platform.

In this thesis the WB model is taken as the base model for developing a full-frequency-dependent (FFD) line model for real-time simulations. The challenges for a real-time model are reviewed next.

The WB model is based on the expressions (2.63) and (2.64) [16] which are repeated here for convenience

$$\mathbf{I}_L - \mathbf{Y}_c \mathbf{V}_L = -\mathbf{H}(\mathbf{I}_0 + \mathbf{Y}_c \mathbf{V}_0)$$

$$\mathbf{I}_0 - \mathbf{Y}_c \mathbf{V}_0 = -\mathbf{H}(\mathbf{I}_L + \mathbf{Y}_c \mathbf{V}_L)$$

Their solutions in time domain are given by (2.65) and (2.66) [16]

$$\mathbf{i}_L - \mathbf{y}_c * \mathbf{v}_L = -\mathbf{h} * (\mathbf{i}_0 + \mathbf{y}_c * \mathbf{v}_0)$$

$$\mathbf{i}_0 - \mathbf{y}_c * \mathbf{v}_0 = -\mathbf{h} * (\mathbf{i}_L + \mathbf{y}_c * \mathbf{v}_L)$$

These expressions contain convolutions and since the WB model solves such equations in the phase domain all matrices in (2.65) and (2.66) are full, thus the model is less efficient than the FD model and requires a higher amount of computational resources. Due to this fact one of the main goals of this thesis is to increase the computational efficiency of the WB model.

If the characteristic impedance matrix \mathbf{Y}_c and the propagation functions matrix \mathbf{H} are synthesized with rational functions, their corresponding expressions in time domain will become simple sums of exponential functions [7],[19]. Then, convolutions in time domain expressions (2.65), (2.66) can be evaluated with a fast recursive algorithm appealing to state space methods.

In order to fit \mathbf{Y}_c and \mathbf{H} functions a least squares method is used, in the original implementation VF fitting is the used tool. There are some reports where the WB has failed or renders unstable models, in [26] a new fitting routine called Weighted Vector Fitting (WVF) is proposed, this routine overcomes most of the problems found with VF.

In the original implementation the modes of \mathbf{H} are calculated via a frequency dependent transformation matrix \mathbf{T}_I as follows:

$$\mathbf{H} = \mathbf{T}_I \mathbf{H}_m \mathbf{T}_I^{-1} \quad (3.17)$$

where \mathbf{T}_I is the matrix of eigenvectors of the \mathbf{YZ} product in (2.57) and \mathbf{H}_m is a diagonal matrix of the form

$$\mathbf{H} = \text{diag}\left[e^{-\alpha_1 L}, e^{-\alpha_2 L}, \dots, e^{-\alpha_n L}\right] \quad (3.18)$$

with α being the modal propagation constant [30].

It can be shown that equation (3.17) can be rewritten as:

$$\mathbf{H} = \sum_{k=1}^N \mathbf{D}_k e^{(-\alpha_k L)} \quad (3.19)$$

where \mathbf{D}_k is the rank-1 matrix obtained by pre-multiplying the k th column of the \mathbf{T}_I matrix by the k th row of the \mathbf{T}_I^{-1} matrix. \mathbf{D}_k is in fact an idempotent [20]. Equation (3.19) can be further decomposed to give:

$$\mathbf{H} = \sum_{k=1}^N \mathbf{D}_k e^{(-\tilde{\alpha}_k L)} e^{(-s\tau_k)} = \sum_{k=1}^N \tilde{\mathbf{H}}_k e^{(-s\tau_k)} \quad (3.20)$$

where τ_k is the time delay associated to the velocity of the k th mode and α_k is the k th modal propagation constant being modified by the delay subtraction. The time delays in (3.20) can be initially estimated by applying Bode's relation for minimum phase complex functions [31] to the modal exponential factors in (3.18). A commune consideration when implementing the WB model is that modal delays often occur in groups with almost identical values and whether a set of exponential factors can be grouped or not is determined by comparing the phase shifts associated to their time delays. The set is a delay group if the phase shift differences are below a pre-established value, typically chosen at 10° at high frequencies [5]. This is the delay grouping method used in standard WB model implementations in EMT-type programs. Nevertheless, it will be shown through examples in the next section that in spite of the associated phases of two modal propagation constants being almost identical, their magnitudes can be quite apart and grouping these constants stiffens the fitting process. This results in poor fitting and consequently causes numerical instability problems in time domain. The number of total poles is not necessarily reduced either with the standard grouping method.

Each term $\tilde{\mathbf{H}}_k$ in (3.20) can be fitted as follows

$$\tilde{\mathbf{H}}_k = \sum_{i=1}^{Nh(k)} \frac{\mathbf{R}_{k,i}}{s - p_{k,i}} \quad (3.21)$$

where $Nh(k)$ corresponds to the k th term $\tilde{\mathbf{H}}_k$, $\mathbf{R}_{k,i}$ is a matrix of residues and $p_{k,i}$ is its i th fitting pole.

With poles and time delays from the modes known, \mathbf{H} is finally fitted in the phase domain where only residues are calculated

$$\mathbf{H} = \sum_{k=1}^{Ng} \exp(-s\tau_k) \sum_{i=1}^{Nh(k)} \frac{\mathbf{R}_{k,i}}{s - p_{k,i}} \quad (3.22)$$

where, Ng is the number of groups. In the case of \mathbf{Y}_c first the poles are calculated from the modal form using the trace [7],[19]

$$\mathbf{Y}_c = \mathbf{G}_0 + \sum_{i=1}^{Ny} \frac{\mathbf{G}_i}{s - q_i} \quad (3.23)$$

and then the elements of \mathbf{Y}_c are fitted in the phase domain where residues are calculated [7], [19]. In this case Ny is the order of the fit, q_i represents the i th fitting pole, \mathbf{G}_i is the corresponding matrix of residues and \mathbf{G}_0 is a constant matrix obtained at the limit of \mathbf{Y}_c when $s=j\omega \rightarrow \infty$. Note that common poles are used for the fitting of all elements of \mathbf{Y}_c [7],[19].

Recalling the line model of (2.63) and (2.64), this can be rewritten as:

$$\mathbf{I}_0 = \mathbf{I}_{sh,0} - \mathbf{I}_{H-aux,0} \quad (3.24)$$

where

$$\mathbf{I}_{sh,0} = \mathbf{Y}_c \mathbf{V}_0 \quad (3.25)$$

and

$$\mathbf{I}_{H-aux,0} = \mathbf{H} \mathbf{I}_{fw,L} \quad (3.26)$$

$$\mathbf{I}_{fw,L} = \mathbf{I}_L + \mathbf{Y}_c \mathbf{V}_L \quad (3.27)$$

Expressions similar to (3.24)-(3.26) are obtained for the line end at $x=L$ by interchanging subscripts “0” and “L” in (3.24)-(3.26). The time domain forms of these equations are as follows:

$$\mathbf{i}_0 = \mathbf{i}_{sh,0} - \mathbf{i}_{h-aux,0} \quad (3.28)$$

$$\mathbf{i}_{sh,0} = \mathbf{y}_c * \mathbf{v}_0 \quad (3.29)$$

$$\mathbf{i}_{h-aux,0} = \mathbf{h} * \mathbf{i}_{fw,L}. \quad (3.30)$$

Expressions (3.28)-(3.30) provide a time domain model for the line end at $x=0$, see Figure 2-7. The model corresponding to the other end is obtained interchanging sub-indexes “0” and “L” at (3.28)-(3.30). Expression (3.28) provides basically the interface of the line end model with a nodal-network solver that usually is an EMTP-type program [32].

Convolutions in (3.29) and (3.30) are carried out conveniently through the state-space relations that arise when matrices \mathbf{Y}_c and \mathbf{H} are represented by rational functions. Using the rational representation for \mathbf{Y}_c of (3.23) a state-space representation for (3.29) is derived next.

Let (3.23) be now introduced in (3.25) as follows:

$$\mathbf{I}_{sh,0} = \mathbf{G}_0 \mathbf{V}_0 + \sum_{i=1}^{Ny} \mathbf{W}_i \quad (3.31)$$

with

$$\mathbf{W}_i = \frac{1}{s - q_i} \mathbf{G}_i \mathbf{V}_0; \quad i = 1, 2, \dots, Ny. \quad (3.32)$$

Subsequent application of the Inverse Laplace Transform in (3.31) and (3.32) yields the following state-space (SS) form for $\mathbf{i}_{sh,0}$

$$\mathbf{i}_{sh,0} = \mathbf{G}_0 \mathbf{v}_0 + \sum_{i=1}^{Ny} \mathbf{w}_i \quad (3.33)$$

and

$$\frac{d\mathbf{w}_i}{dt} = q_i \mathbf{w}_i + \mathbf{G}_i \mathbf{v}_0; \quad i = 1, 2, \dots, Ny. \quad (3.34)$$

A SS form for (3.26) is obtained in a similar way as for $\mathbf{i}_{sh,0}$ above. Introduction of (3.22) into (3.26) renders

$$\mathbf{I}_{H-aux,0} = \sum_{k=1}^{Ng} \sum_{i=1}^{Nh(k)} \mathbf{X}_{k,i} \quad (3.35)$$

where

$$\mathbf{X}_{k,i} = \frac{\mathbf{R}_{k,i}}{s - p_{k,i}} \mathbf{I}_{fw,L} \exp(-s \tau_k); \quad \begin{array}{l} k = 1, 2, \dots, Ng \\ i = 1, 2, \dots, Nh(k) \end{array} \quad (3.36)$$

Application of the Inverse Laplace Transform to (3.35) and (3.36) yields the following SS form of (3.26) for evaluation of $\mathbf{i}_{h-aux,0}$

$$\mathbf{i}_{h-aux,0} = \sum_{k=1}^{Ng} \sum_{i=1}^{Nh(k)} \mathbf{x}_{k,i} \quad (3.37)$$

$$\frac{d\mathbf{x}_{k,i}}{dt} = p_{k,i} \mathbf{x}_{k,i} + \mathbf{R}_{k,i} \mathbf{i}_{fw,L}(t - \tau_k); \quad \begin{array}{l} k = 1, 2, \dots, Ng \\ i = 1, 2, \dots, Nh(k) \end{array} \quad (3.38)$$

The SS forms (3.33), (3.34), (3.37) and (3.38) provide the basis for the WB line model [16], [22]. However, their solution by a digital processor requires the SS forms to be discretized. This is accomplished applying a numerical differentiation rule to the SS forms. The one adopted here as well as in the original implementation is the trapezoidal rule of integration extensively used in EMTP [1],[16].

The application of the trapezoidal integration to (3.33) and (3.34) with Δt as the solution time step results in:

$$\mathbf{w}_i = \alpha_i \mathbf{w}'_i + \lambda_i (\mathbf{v}_0 + \mathbf{v}'_0); \quad i = 1, 2, \dots, Ny \quad (3.39)$$

$$\mathbf{i}_{sh,0} = \mathbf{G}_0 \mathbf{v}_0 + \sum_{i=1}^{Ny} \mathbf{w}_i \quad (3.40)$$

where primed values indicated the value of the variable one time step behind.

At the original implementation a change of variable in above equations is made because the state variable \mathbf{w}_i depends on the input at the same time instant of evaluation (*i.e.* has an improper

form) [16], [19]. Nevertheless, in EMTP the input is the first datum given to the model. Thus, in theory there is no need to realize such variable change. However, it was found that the change of variable allows increasing the numerical performance of the model [22] and for this reason the change of variable continues to be applied in this work. The mathematical proof of this assertion is given in Appendix I. Thus, introduction of the succeeding state variable

$$\mathbf{x}_i = \mathbf{w}_i - \lambda_i \mathbf{v}_0; \quad i = 1, 2, \dots, Ny \quad (3.41)$$

into (3.39) and (3.40) results in

$$\mathbf{x}_i = \alpha_i \mathbf{x}'_i + \beta_i \mathbf{v}'_0; \quad i = 1, 2, \dots, Ny \quad (3.42)$$

$$\mathbf{i}_{sh,0} = \mathbf{G}_y \mathbf{v}_0 + \sum_{i=1}^{Ny} \mathbf{x}_i \quad (3.43)$$

A second change of variable can be applied in order to simplify the state equation [19] ; this is only done at the original implementation, in this work just the first change of variable is carried out. Then, the next variable is introduced in (3.42) and (3.43)

$$\mathbf{y}_i = \beta_i^{-1} \mathbf{x}_i; \quad i = 1, 2, \dots, Ny \quad (3.44)$$

which renders

$$\mathbf{y}_i = \alpha_i \mathbf{y}'_i + \mathbf{v}'_0; \quad i = 1, 2, \dots, Ny \quad (3.45)$$

$$\mathbf{i}_{sh,0} = \mathbf{G}_y \mathbf{v}_0 + \sum_{i=1}^{Ny} \beta_i \mathbf{y}_i. \quad (3.46)$$

Variables α, λ, β and \mathbf{G}_y are as follows:

$$\alpha_i = \frac{2 + \Delta t q_i}{2 - \Delta t q_i}, \quad i = 1, 2, \dots, Ny$$

$$\lambda_i = \frac{\Delta t \mathbf{G}_i}{2 - \Delta t q_i}, \quad i = 1, 2, \dots, Ny$$

$$\beta_i = (\alpha_i + 1)\lambda_i, \quad i = 1, 2, \dots, Ny$$

$$\mathbf{G}_y = \mathbf{G}_0 + \sum_{i=1}^{Ny} \lambda_i.$$

A discrete SS form for expressions (3.37) and (3.38) is obtained in a similar way as for (3.33) and (3.34). Applying the trapezoidal rule of integration to (3.37) and (3.38)

$$\mathbf{x}_{k,i} = \alpha_{k,i} \mathbf{x}'_{k,i} + \lambda_{k,i} \left[\mathbf{i}_{fw,L}(t - \tau_k) + \mathbf{i}'_{fw,L}(t - \tau_k) \right] \quad \begin{matrix} k = 1, 2, \dots, Ng \\ i = 1, 2, \dots, Nh(k) \end{matrix} \quad (3.47)$$

$$\mathbf{i}_{h-aux,0} = \sum_{k=1}^{Ng} \sum_{i=1}^{Nh(k)} \mathbf{x}_{k,i} \quad (3.48)$$

And introducing the new state variable

$$\mathbf{w}_{k,i} = \mathbf{x}_{k,i} - \lambda_{k,i} \mathbf{i}_{fw,L}; \quad \begin{matrix} k = 1, 2, \dots, Ng \\ i = 1, 2, \dots, Nh(k) \end{matrix} \quad (3.49)$$

into (3.51) and (3.48) the following expressions are obtained

$$\mathbf{w}_{k,i} = \alpha_{k,i} \mathbf{w}'_{k,i} - \beta_{k,i} \mathbf{i}'_{fw,L}(t - \tau_k); \quad \begin{matrix} k = 1, 2, \dots, Ng \\ i = 1, 2, \dots, Nh(k) \end{matrix} \quad (3.50)$$

$$\mathbf{i}_{h-aux,0} = \sum_{k=1}^{Ng} \sum_{i=1}^{Nh(k)} \left(\mathbf{w}_{k,i} + \lambda_{k,i} \mathbf{i}_{fw,L}(t - \tau_k) \right) \quad (3.51)$$

Changing again the state variable for

$$\mathbf{y}_{k,i} = \beta_{k,i}^{-1} \mathbf{w}_{k,i}; \quad \begin{matrix} k = 1, 2, \dots, Ng \\ i = 1, 2, \dots, Nh(k) \end{matrix} \quad (3.52)$$

the next expressions are given

$$\mathbf{y}_{k,i} = \alpha_{k,i} \mathbf{y}'_{k,i} + \mathbf{i}'_{fw,L}(t - \tau_k); \quad \begin{matrix} k = 1, 2, \dots, N_g \\ i = 1, 2, \dots, Nh(k) \end{matrix} \quad (3.53)$$

$$\mathbf{i}_{h-aux,0} = \sum_{k=1}^{N_g} \sum_{i=1}^{Nh(k)} (\mathbf{y}_{k,i} \boldsymbol{\beta}_{k,i} + \boldsymbol{\lambda}_{k,i} \mathbf{i}_{fw,L}(t - \tau_k)) \quad (3.54)$$

where variables $\alpha, \boldsymbol{\lambda}$ and $\boldsymbol{\beta}$ are as follows:

$$\alpha_{k,i} = \frac{2 + \Delta t p_{k,i}}{2 - \Delta t p_{k,i}}, \quad \begin{matrix} k = 1, 2, \dots, N_g \\ i = 1, 2, \dots, Nh(k) \end{matrix}$$

$$\boldsymbol{\lambda}_{k,i} = \frac{\Delta t \mathbf{R}_{k,i}}{2 - \Delta t p_{k,i}}, \quad \begin{matrix} k = 1, 2, \dots, N_g \\ i = 1, 2, \dots, Nh(k) \end{matrix}$$

$$\boldsymbol{\beta}_{k,i} = (\alpha_{k,i} + 1) \mathbf{R}_{k,i}, \quad \begin{matrix} k = 1, 2, \dots, N_g \\ i = 1, 2, \dots, Nh(k) \end{matrix}$$

In general the time delay τ of a given delay group will not be an integer multiple of the time step Δt used in the simulation [16],[19],[33].[34] This makes it necessary to interpolate between sample points of the forward currents.

The travel time is expressed as:

$$\tau = (m + \varepsilon) \Delta t \quad (3.55)$$

where m is an integer and ε is a real number between 0 and 1. The interpolated values are calculated by linear interpolation. In [34] the use of second order interpolation was investigated and it was found that the use of linear interpolation is satisfactory since second order interpolation only renders from 1 to 2% of accuracy improvements.

3.6 WB Model vs CP Model

In this section several examples that reinforce the need of a Full-Frequency-Dependent (FFD) line model by putting in evidence the flaws of the Constant Parameters (CP) model are shown.

3.6.1 Real-Time WB (RTWB) ac 3-phase Cable

The first example consists of the 3-phase underground cable depicted in Figure 3-3. The test circuit is given in Figure 3-4. Circuit parameters are:

- Cable length: 15 km
- Cable sheaths are grounded by a 1Ω resistance at both ends
- AC source AC1: 169 kV, Y-grounded
- R1 is 1 k Ω
- RL1 is determined by its zero and positive sequence data in Ohms: $R_0=2$, $R_I=1$, $X_0=22$, $X_I=15$
- Capacitor bank is determined in Siemens $C1=0.000278$
- Switch SW1 closing times are: 0 s on phase a, 0.63 ms on phase b and 0.4 ms on phase c

Transversal dimensions, electrical properties of each cable and the case provenance are listed in Table 3.1. In this case the voltage at both ends is measured at the cores and at the sheaths of the cable. The used simulation time step is $1\mu s$. Figure 3-5 to Figure 3-8 present the voltage waveforms obtained with both models the WB (solid line) and the CP (dashed line) where phase a is represented in blue, phase b in green and phase c in red. After analysis of these figures is obvious that the CP model does not represent accurately the transient phenomenon being simulated for results disagree completely from those obtained by the WB model. The CP model does not only presents more damping for this case but also fails to present the high frequency peaks that result from the use of the capacitors bank as can be seen in Figure 3-7 and Figure 3-8 where these effects are more noticeable. For this case CP parameters were calculated for a frequency of 10 kHz.

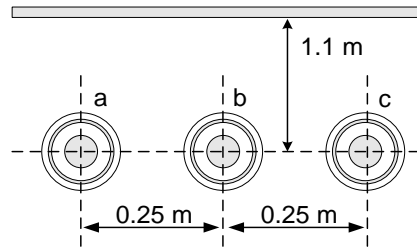


Figure 3-3 : RTWB ac 3-phase cable layout.

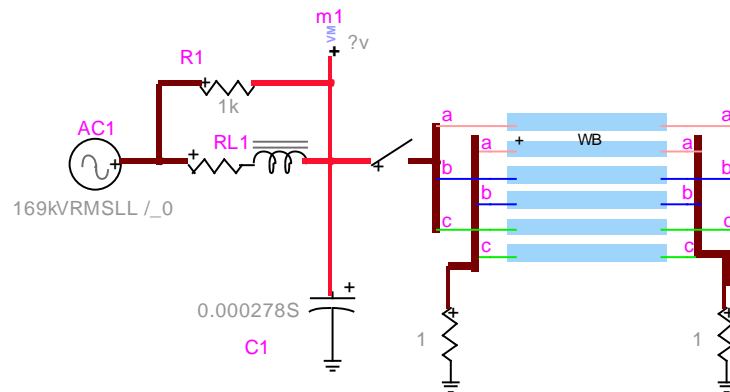


Figure 3-4 : RTWB ac 3-phase cable circuit test.

Table 3.1 : RTWB ac 3-Phase Cable Provenance and Data

Case proposed by Jean Mahseredjian	
Radius of inner solid conductor (m)	0.003175
Resistivity nuclei/sheath (ohm/m)	2.1e-7/1.7e-8
Inner/Outer radius of sheath (m)	0.022735/0.026225
Relative permittivity of 1st & 2nd insulation	3.5/2.0
Insulation Outer radius	0.029335

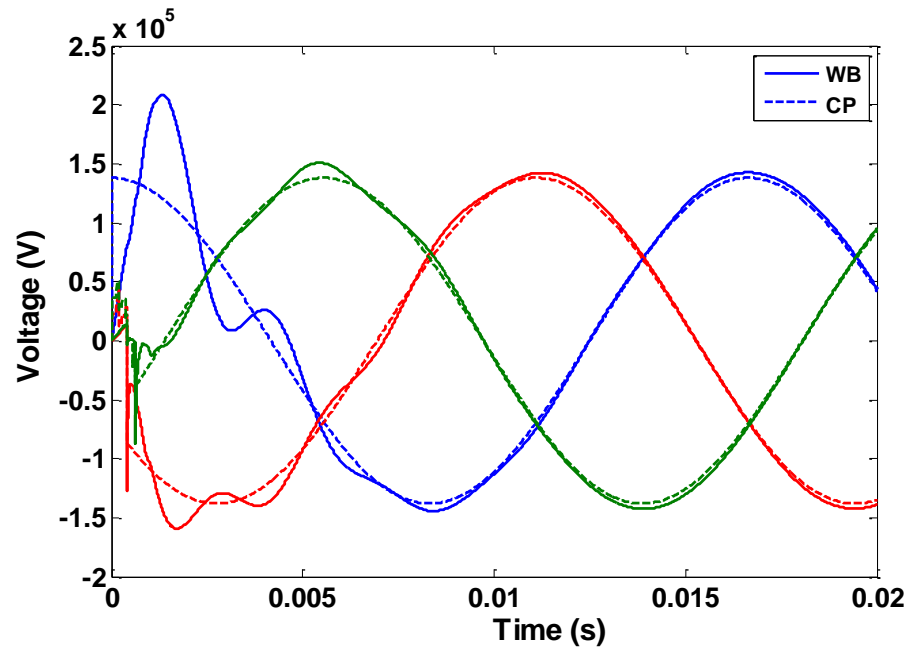


Figure 3-5 : RTWB ac 3-phase cable. Voltage waveforms at the sending end of the cores, comparison with the CP model.

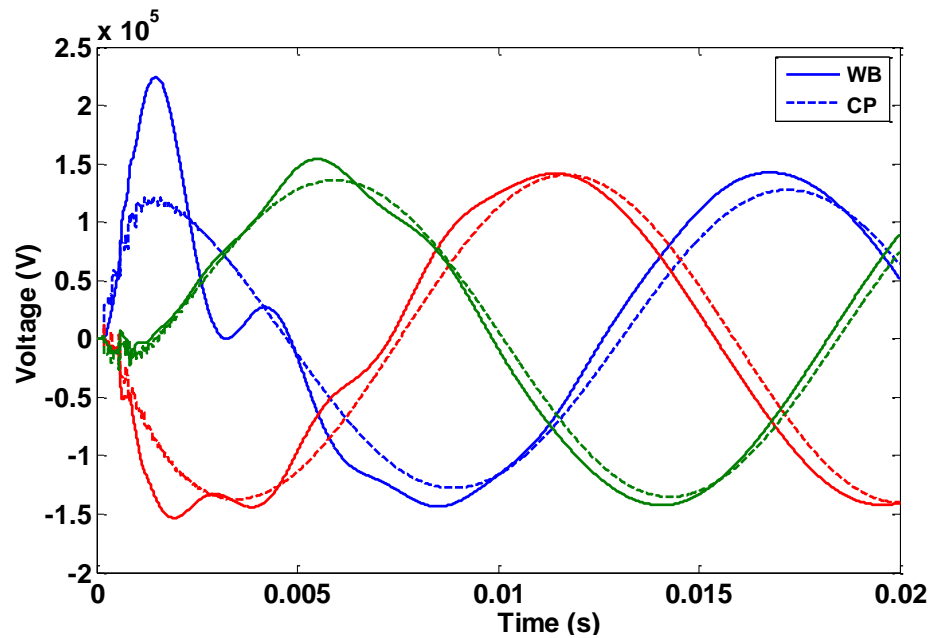


Figure 3-6 : RTWB ac 3-phase cable. Voltage waveforms at the receiving end of the cores, comparison with the CP model.

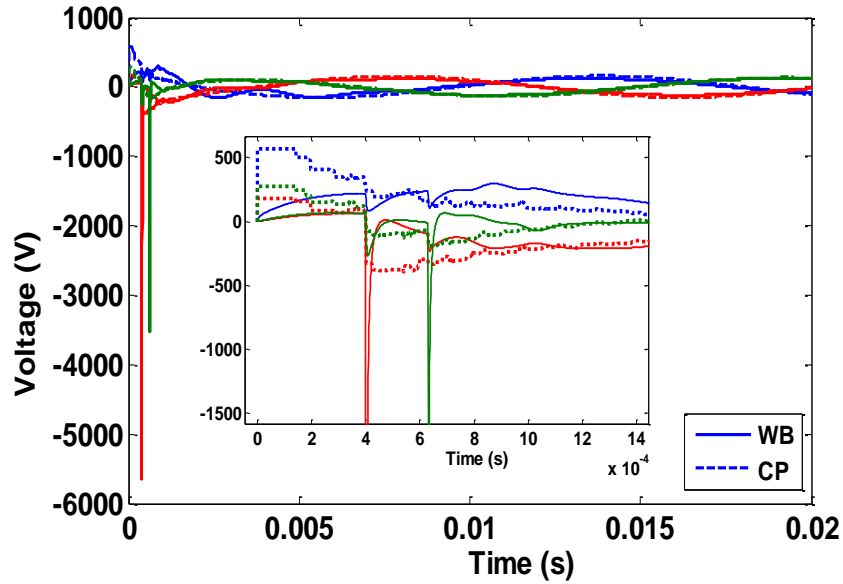


Figure 3-7 : RTWB ac 3-phase cable. Voltage waveforms at the sending end of the sheaths, comparison with the CP model. Insert; close up of the y and x axis.

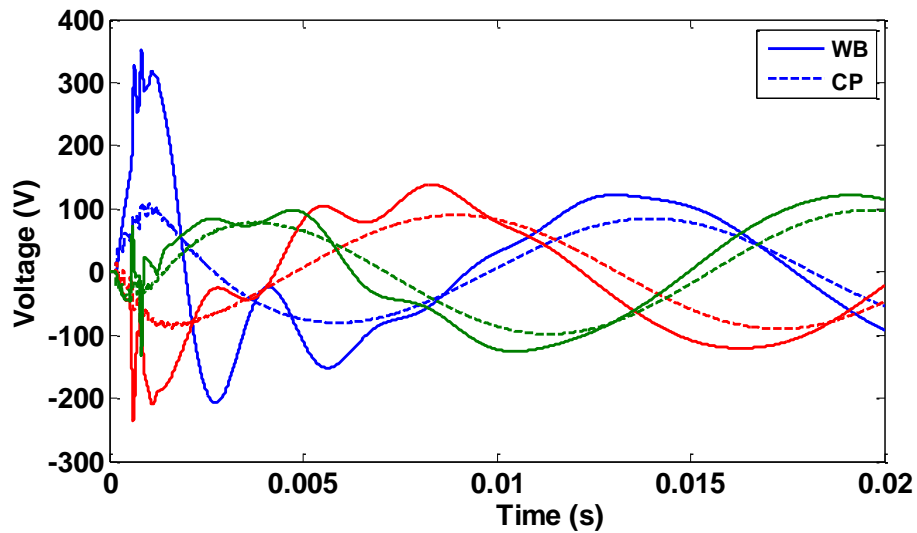


Figure 3-8 : RTWB ac 3-phase cable. Voltage waveforms at the receiving end of the sheaths, comparison with the CP model.

3.6.2 CP 3-phase aerial line

The second case consists of an unbalance fault in the 3-phase aerial line depicted in Figure 3-9. The test circuit is given in Figure 3-10. Circuit parameters are:

- Line length: 200 km
- Phase a and c are faulted by a 20Ω resistance at receiving end (numerical test, no practical application)
- AC source AC1: 345 kV, Y-grounded
- RL1 is determined by its zero and positive sequence data in Ohms: $R_0=2$, $R_1=1$, $X_0=22$, $X_1=15$
- Switch SW1 closes at 15 ms and SW2 closes at 5ms

Transversal dimensions, and electrical properties of phase and ground wires as well as the case provenance are given in Table 3.2. The simulation time step used in this case is $5\mu\text{s}$. In this case the voltage at the receiving end is measured. The voltage waveforms obtained at phase c with the WB (solid line) and the CP (dashed line) model are compared in Figure 3-11. From this figure it can be seen that the CP model renders incorrect results. For this case CP parameters were calculated for a frequency of 3325 Hz (automatically chosen by EMTP), this explains the difference at steady state seen in Figure 3-11.

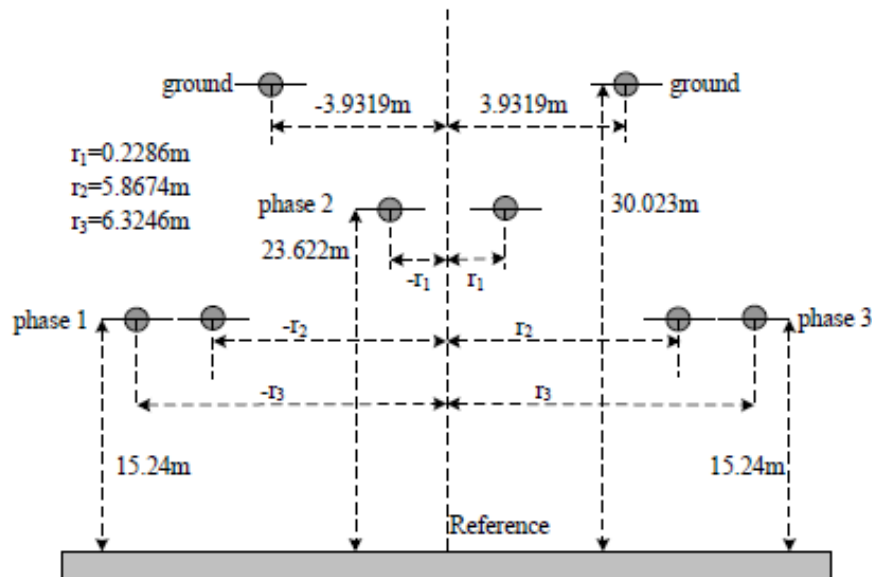


Figure 3-9 : CP 3-phase aerial line circuit layout.

Table 3.2 : CP 3-Phase Aerial Line Provenance and Data

Case proposed by Ilhan Kocar	
Conductors diameter phase/ground (m)	0.040698/0.009804
DC resistance phase/ground (ohm/m)	32.4e-6/162.16e-6

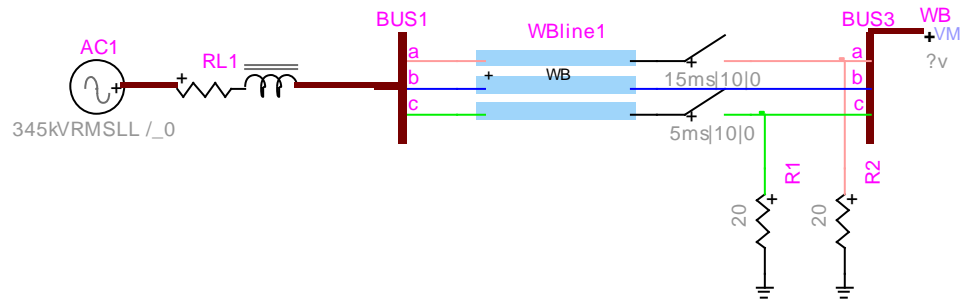


Figure 3-10 : CP 3-phase aerial line test circuit.

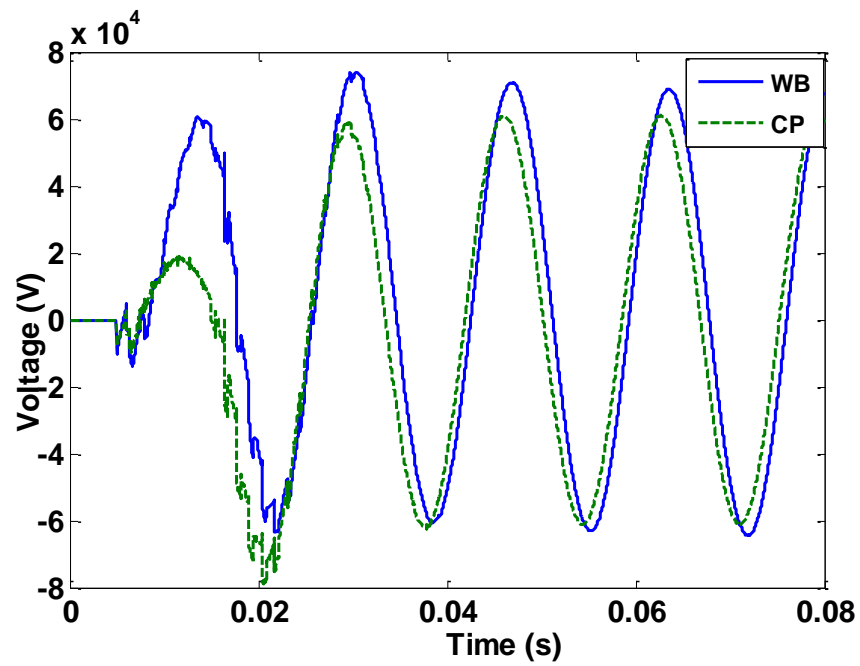


Figure 3-11 : CP 3-phase aerial line voltage waveform at phase b.

3.6.3 RTWB 6-phase underground cable

The underground cable system used in this test consists of six coaxial cables; the system and test were taken from [7] the system layout is shown in Figure 3-12. Corresponding electrical circuit diagram is shown in Figure 3-13. Circuit parameters are:

- Cable length: 1km
- Cable sheaths are solidly grounded at both ends
- DC source DC_1: 1V, for numerical proposes
- Cable cores are open ended
- DC source activates at time $t=0s$

Transversal dimensions and electrical properties of each cable as well as the case provenance are listed in Table 3.3.

Simulation results are presented in Figure 3-14, where WB results are in solid line whereas CP results are in dashed line. The used time step in this case is $1\mu s$. The discrepancies between both results can be easily spotted. An interesting phenomenon to notice besides the loss of phase and the low damping of the CP model is the rounding effect obtained when using the WB model. Such rounding is due to the frequency dependence of line parameters a feature that is not accounted by the CP model. For this case CP parameters where calculated for a frequency of 1 kHz.

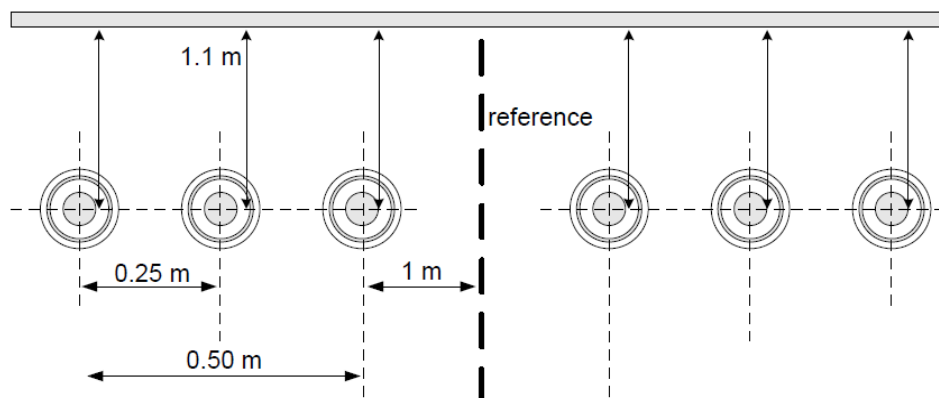


Figure 3-12 : RTWB 6-phase underground cable layout.

Table 3.3 : RTWB 6-Phase Cable Provenance and Data

Case proposed by Ilhan Kocar	
Inner/Outer radius of core (m)	0.003175/0.01254
Resistivity nuclei/sheath (ohm/m)	1.7e-8/3.36e-8
Inner/Outer radius of sheath (m)	0.022735/0.026225
Relative permittivity of 1st & 2nd insulation	3.5/2.0
Insulation Outer radius	0.029335

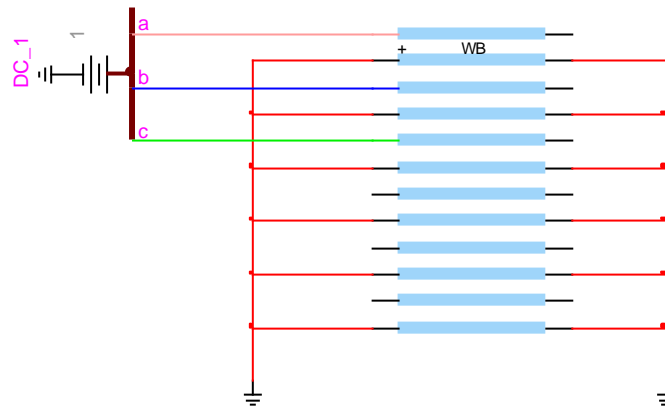


Figure 3-13 : RTWB 6-phase underground cable test circuit.

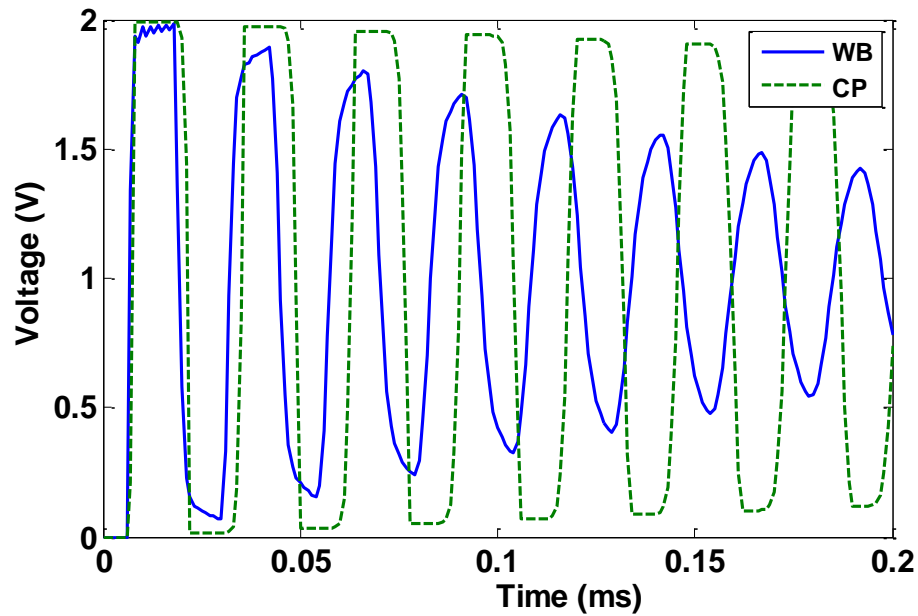


Figure 3-14 : RTWB 6-phase underground cable voltage waveform at receiving end of phase 1.

3.6.4 Transmission Network

For this test a 230 kV transmission network with 7 buses, 4 loads and 6 generators is used. Network configuration is taken from [35] and is shown in Figure 3-16. The network contains 7 transmission lines with the configuration shown in Figure 3-15 and different lengths, all phase conductors are 1192.5 ASCR 54/19. The network contains 5 transformers. Transformers, loads, capacitors and sources data is given in Figure 3-16.

The test performed in this case consists of a 2-phase unbalance fault at one end of the transmission line that runs between Bus 7 and Bus 1. At time $t=0.2s$ the fault occurs in the line at the side of Bus 1, the fault is cleared after 0.05s at time $t=0.25s$ by opening the switches between the faulted line. After 0.05s the fault is cleared and the line is reconnected to the network at time $t=0.3s$. Figure 3-17 shows the voltage at Bus 3 for phase b obtained with both the WB (solid line) and the CP (dashed line) model. The simulation time step used in this case is $10\mu s$.

After analysis of Figure 3-17 it can be seen that at $t=0.2s$ the applied fault is almost imperceptible for the system whereas at $t=0.22s$ there is an overvoltage which is well represented as the rest of the fault by the CP model. At time $t=0.25s$ when the line is liberated a trapped charge appears in the line, this trapped charge is not well represented by the CP model in fact it is underestimated as can be seen in Figure 3-18 which presents a close up of Figure 3-17. At time $t=0.3s$ when the line is reconnected the occurring transient is misrepresented by the CP model given that the first strike is underestimated by 1.5kv and the second strike is overestimated by 3.3kv by the CP model. Afterwards, for the rest of the simulation the CP model presents less attenuation than the WB model. For this case CP parameters were calculated for a frequency of 1 kHz.

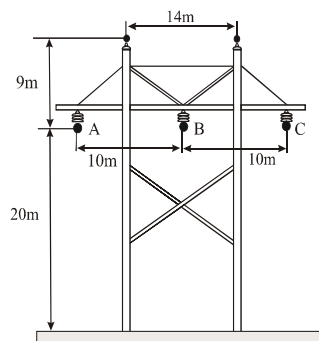


Figure 3-15 : Transmission line configuration.

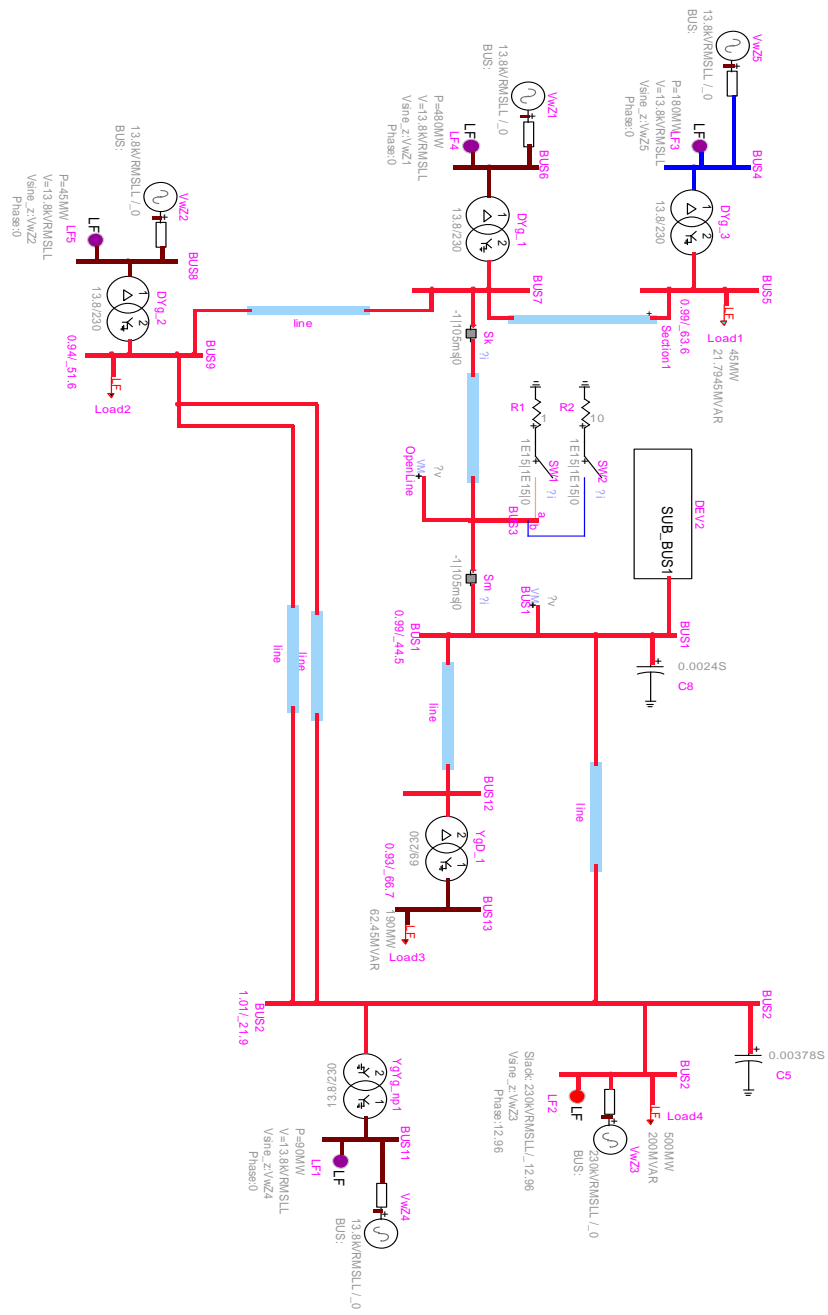


Figure 3-16 : Transmission network layout and data.

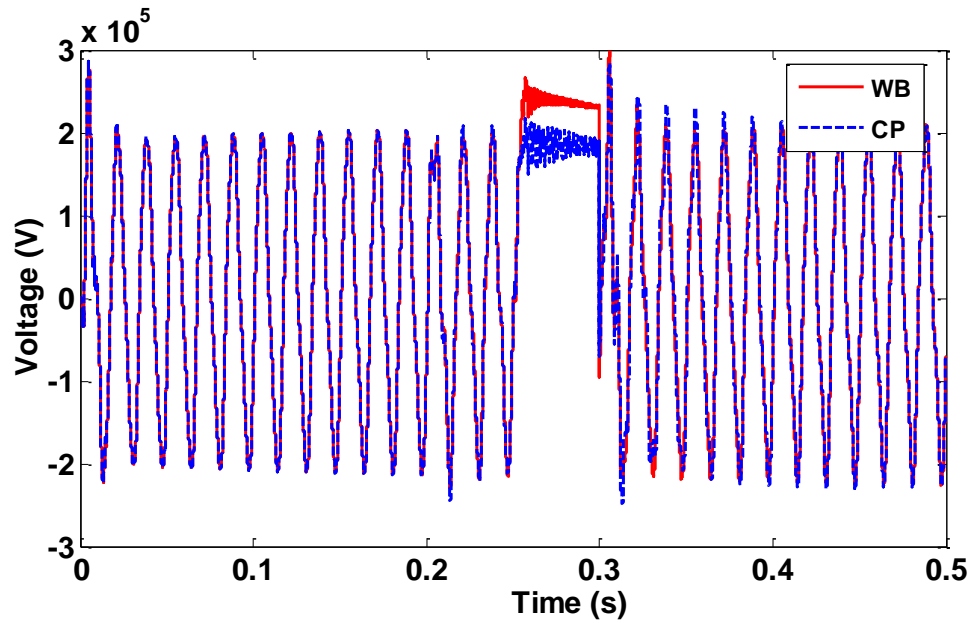


Figure 3-17 : Transmission network voltage waveform at phase b.

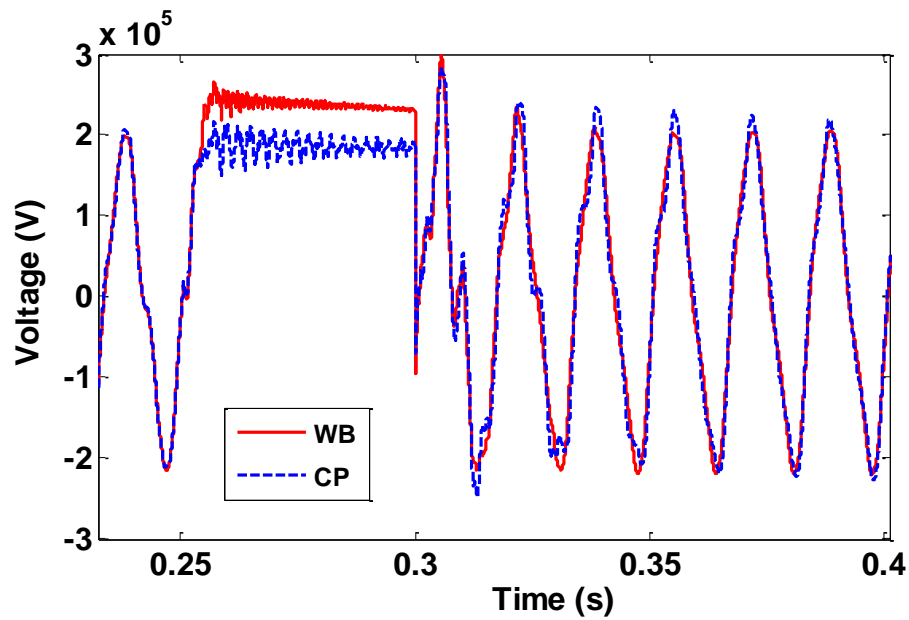


Figure 3-18 : Transmission network voltage waveform at phase b, close up.

3.7 WB Model vs FD Model

In Section 3.3 it was mentioned that the FD model renders inaccurate results when used for very asymmetrical multicircuit lines. The next examples show this issue.

3.7.1 Double Circuit Aerial Line

As a first example consider the feeding of a consumption plant represented by its inductance, resistance and a transformer as shown in the right-hand side of Figure 3-19. Consumption plant data is shown in Figure 3-19. The left-hand side of the figure contains the energizing plant, where all the related data is shown. The source is an inductive 20kV source. The transmission line is a mirror circuit whose layout is given in Figure 3-20. The conductor data as well as the case provenance are given in Table 3.4. The length of the line is 252km.

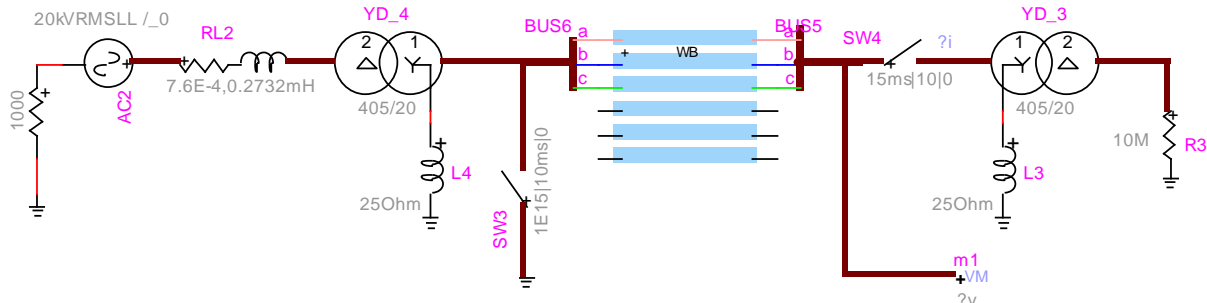


Figure 3-19 : Double circuit aerial line energizing plant.

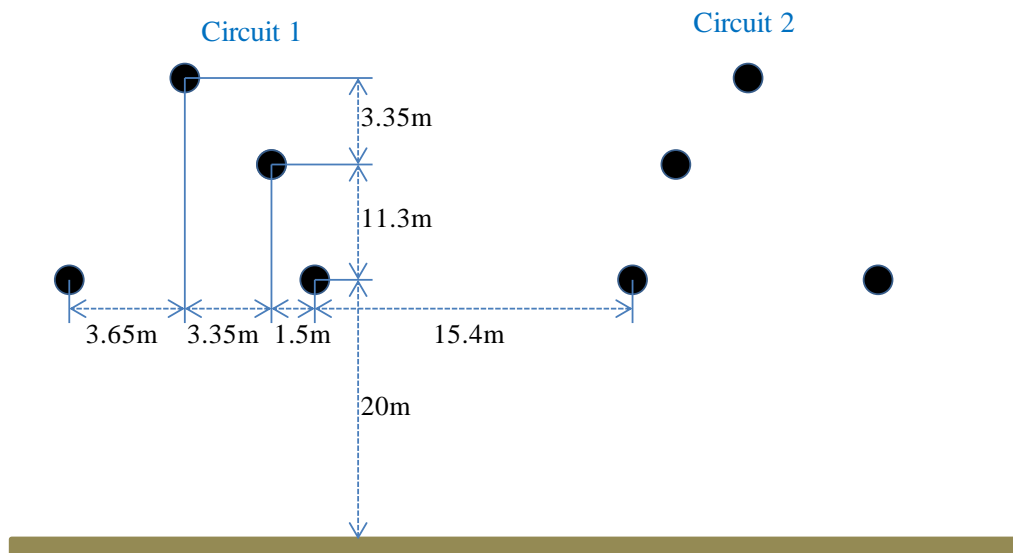


Figure 3-20 : Double circuit aerial line layout.

Table 3.4 : Double Circuit Aerial Line Provenance and Data

Case proposed by Jean Mahseredjian	
Conductors diameter phase/ground (m)	0.03284/0.0143
DC resistance phase/ground (ohm/m)	50.52e-6/260.76e-6

The simulation for this case starts from steady state, switch SW3 remains open during the entire simulation, the receiving end of the line remains open until switch SW4 closes at 15 ms feeding the plant. Only circuit 1 is fed whereas circuit 2 remains open at both sides. The simulation time step is 20 μ s. Voltages and currents are measured at the receiving end of the line and results are given in Figure 3-21 and Figure 3-22. Results for the WB model are plotted using solid lines and FD results are plotted with dashed lines.

Analyzing Figure 3-21 and Figure 3-22 is clear that the WB and FD models render very different results for this case not only in magnitude but also in phase, presenting the most prominent differences in the currents. This is due to the fact that the receiving side presents a short-circuit condition where the FD line is more prone to fail. This situation was exposed in [24] and explained in [25]. The explanation given there is as follows:

When a voltage is applied to an open or short circuited line, voltages or currents are given by the following equation for the open case

$$V_{oc} = V_s \frac{2H}{1+H^2} \quad (3.56)$$

and for the short circuit case:

$$I_{sc} = V_s Y_c \frac{1+H^2}{1-H^2} \quad (3.57)$$

When H tends to 1 as ω tends to zero, (3.56) gives $V_{oc} \approx V_s$. However, the denominator of (3.57) tends to zero and the small errors in the eigenvalues which determine H will produce large variations in the current. Also notice that the short-circuit condition depends on both the H matrix and the Y_c matrix, thus I_{sc} is much more affected by errors than V_{oc} .

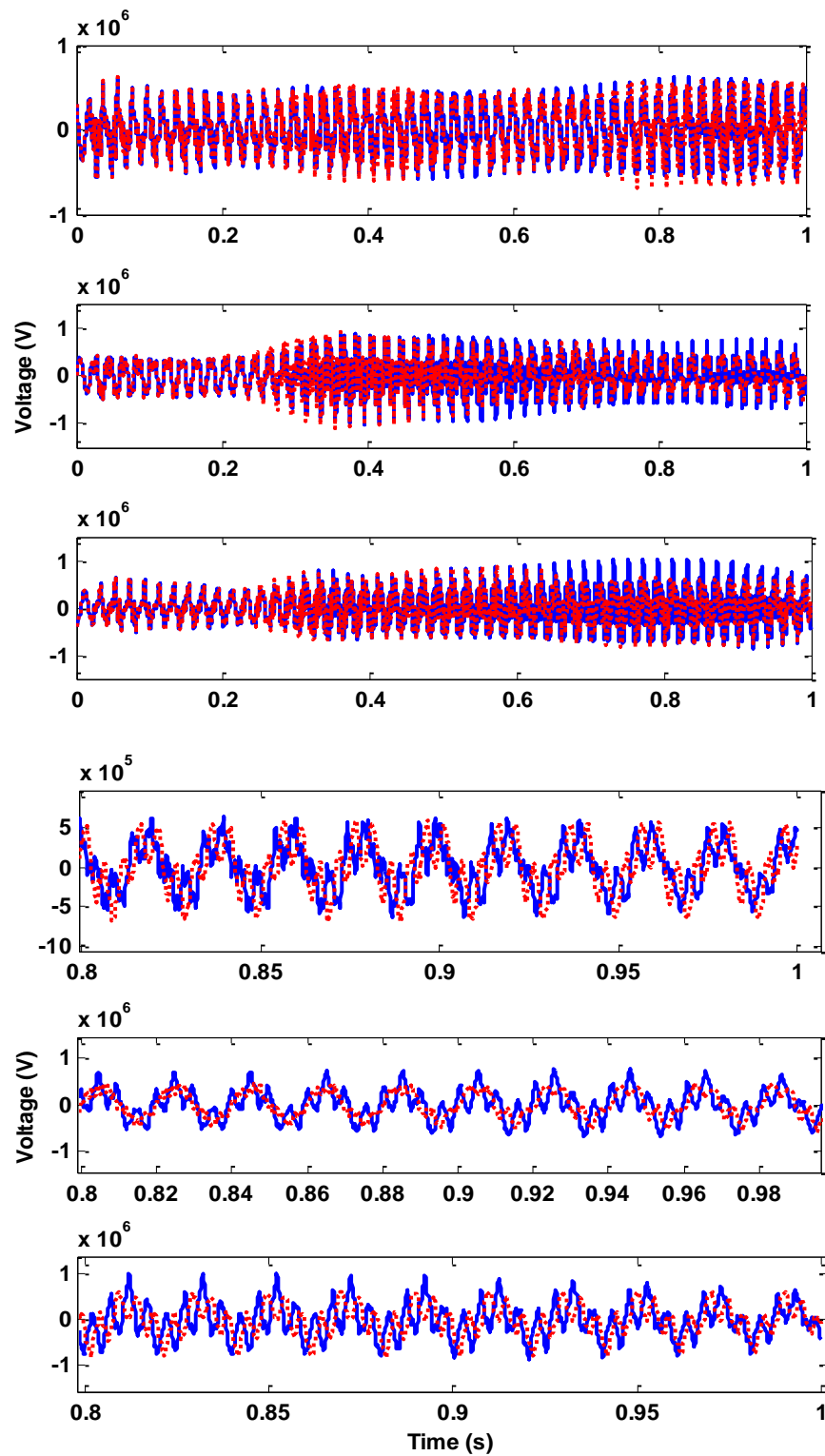


Figure 3-21 : Double circuit aerial line voltage waveforms at the consumption plant side of circuit 1, subplots correspond to phase a, b, c, close up on phase a, b and c, respectively. WB solid line, FD dashed line.

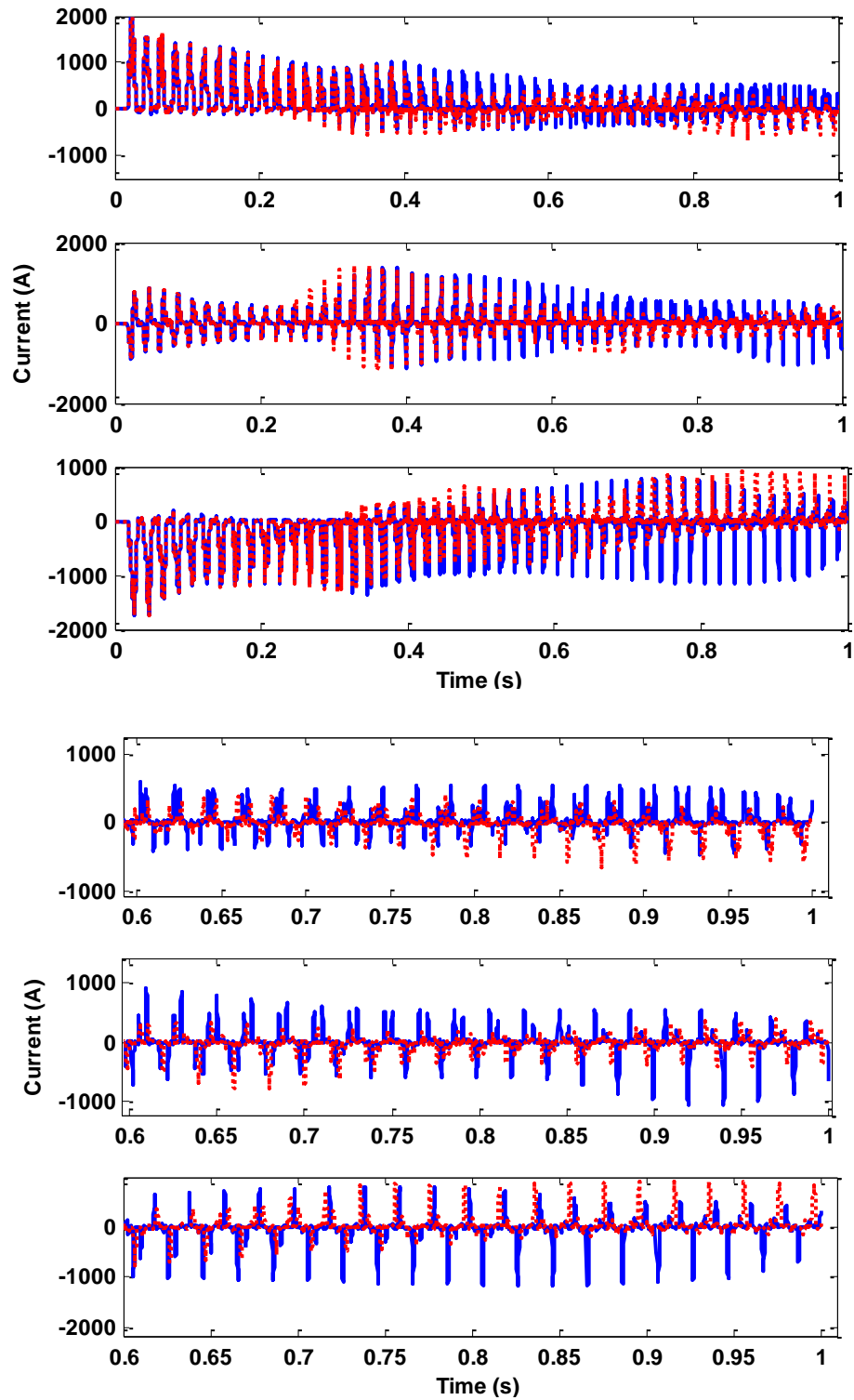


Figure 3-22 : Double circuit aerial line current waveforms at the consumption plant side of circuit 1, subplots correspond to phase a, b, c, close up on phase a, b and c, respectively. WB solid line, FD dashed line.

3.7.2 BC HYDRO 9-Phase Aerial Line

This case consists of the 9-phase aerial line depicted in Figure 3-23. Phase conductors are 1192.5 kcmil ASCR 54/19 and ground wires are ACSS no. 5. There are three coupled transmission circuits. Circuit 1 is composed of conductors 1 to 3, Circuit 2 by conductors 5 to 6 and Circuit 3 uses conductors 7 to 9. The line length is 150 km. The test circuit is shown in Figure 3-24 where the value of the ideal source is 735kV. This case was proposed by BC Hydro and was obtained from [24].

The simulation (numerical test) presents a solid 3-phase fault to ground at the receiving end of circuit 1 while circuits 2 and 3 are grounded through a 10 ohms resistance (numerical test) at both sides of the line. The induced voltage at phase 5 is plotted in Figure 3-25 for both models WB (solid line) and FD (dashed line). In the same figure differences between both models are conspicuous. As explained in the last example the differences between both models are the result of the fact that the FD model fails when applied to very asymmetrical aerial lines and/or short-circuit simulations [24]. The simulation time step for this case is 10 μ s.

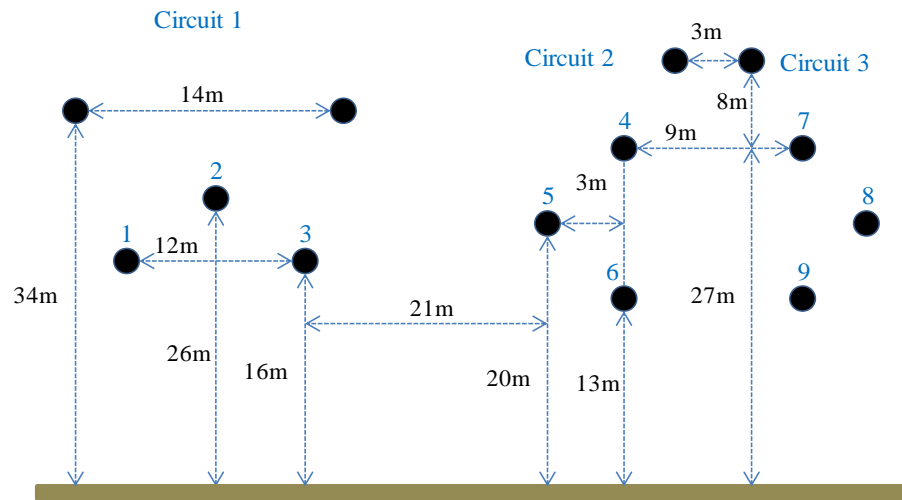


Figure 3-23 : BC HYDRO 9-phase aerial line layout.

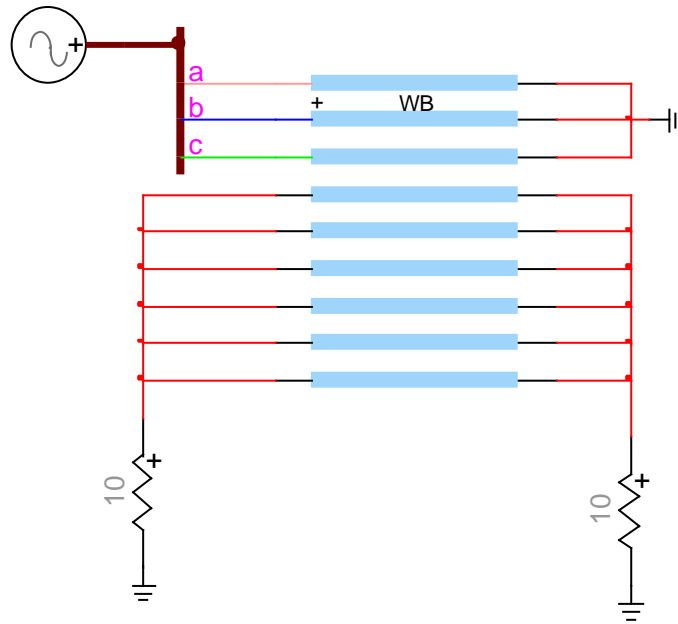


Figure 3-24 : BC HYDRO 9-phase aerial line test circuit, WB vs FD.

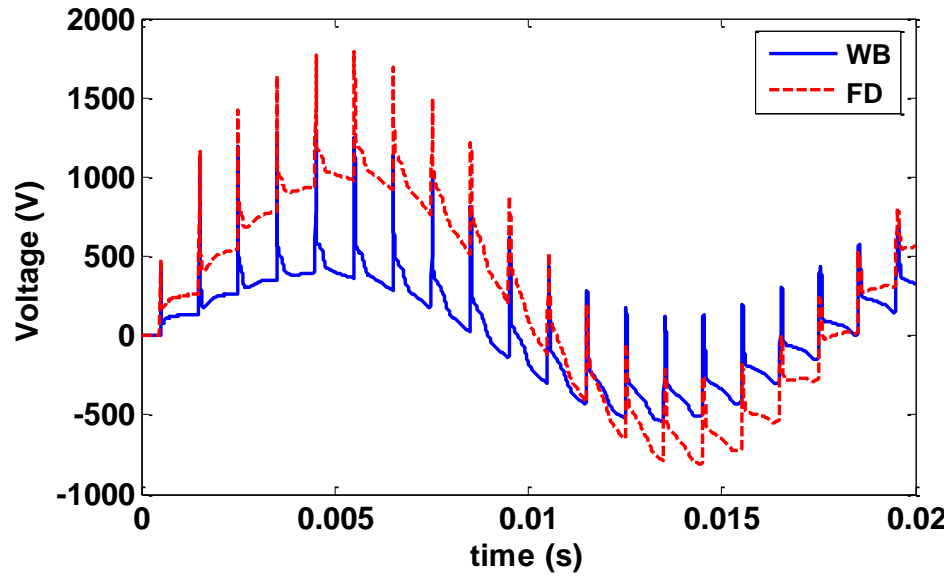


Figure 3-25 : BC HYDRO 9-phase aerial line voltage waveform at the receiving end of the 5th phase, WB vs FD.

3.8 Remarks

In this chapter it was stated that the WB model is the most accurate and general model available nowadays. The model takes into account the full-frequency-dependence of line/cable parameters and works directly in the phase domain.

It was also stated that WB model suffers from some drawbacks regarding computational efficiency and for some cases obtaining passive and stable rational approximations. Despite of these drawbacks the WB model is used in this work for the development of a FFD model for real-time simulations. Since high computational performance is crucial for real-time platforms, this aspect is researched in this work.

There are reports which present cases where the WB model fails or renders unstable models. Thus, this thesis also searches to mitigate the problems causing the WB model to fail.

A comparison between the WB, the CP and the FD models was presented. The obtained results demonstrate that the CP model is incapable of accurately simulate cases where the frequency dependence of line parameters play an important role whereas the FD model fails to accurately represent short-circuit conditions and highly asymmetrical lines plus the fact that the FD is unsuitable to simulate underground cables [16]. The obtained results indicate that the WB model is the most appealing model to be applied in a real-time platform in terms of generality and reliability.

CHAPTER 4 RATIONAL REALIZATIONS

Matrices \mathbf{Y}_c and \mathbf{H} , which fully describe the EMT behavior of multiconductor lines and cables in the frequency domain, are related to the \mathbf{YZ} product through transcendental matrix functions. At practical analysis these relations are approximated by rational matrix functions. The major advantage of this approach is that enables the application of well-established state-space techniques in the time domain simulation of travelling waves.

The accuracy of those rational approximations is a major feature sought in EMT analysis; however, it is not the only one. Rational approximations should also guarantee that line synthesized models be causal, stable as well as passive [36]. It has been shown in [36] that if a model is passive, then it is causal and stable. It has also been shown there that causality and stability do not imply passivity. Another feature desirable in rational approximations, particularly at those intended for real-time simulations, is these are of low order. The reason for this is that computation time is proportional to model order.

The technique employed in this thesis to perform rational approximations is the one known as Weighted Vector Fitting (WVF) that was first proposed in [26]. WVF is an improvement of the Vector Fitting (VF) method previously proposed in [3].

Even though WVF and VF enforce stability and causality by assuring that all poles have strictly negative real parts, there are still many cases where both techniques render nonpassive approximations causing the time-domain solution to diverge or present erroneous results due to passivity violations.

In this chapter the basic theory of the WVF technique is presented in a general manner along with the theory for VF since WVF is based on the latter. Special attention is given to the common practice of mode grouping as this grouping can sometimes lead to nonpassive models.

4.1 Vector Fitting

The purpose of the VF utility is to obtain a rational approximation for a given frequency-response function $f(s)$. The rational approximation is represented in the form of a partial fraction expansion (PFE) as follows

$$f(s) \cong \sum_{n=1}^N \frac{r_n}{s + \bar{p}_n} \quad (4.1)$$

where N is the order of the fit, p_1, p_2, \dots, p_N are poles or roots of the denominator polynomial and r_1, r_2, \dots, r_N are the residues corresponding to each pole. VF estimates the system parameters (*i.e.*, poles and residues) through a two-stage linear least-squares procedure. The first stage consists in the identification of poles for the rational fit. The second stage is for the identification of the corresponding residues.

First a set of initial poles is proposed for the partial fraction approximation as in (4.1); then these poles are relocated iteratively until the prescribed convergence is achieved. Convergence is tested by means of a second linear least-squares approximation for which the poles are already known and residues are to be determined.

VF fitting basic relation is [7]:

$$\sum_{n=1}^N \frac{\hat{r}_n}{s + \bar{p}_n} \cong f(s) \left(1 + \sum_{n=1}^N \frac{\tilde{r}_n}{s + \bar{p}_n} \right) \quad (4.2)$$

where, $\bar{p}_1, \bar{p}_2, \dots, \bar{p}_N$ are the poles known either from initialization or from previous iteration. $\hat{r}_1, \hat{r}_2, \dots, \hat{r}_n$ and $\tilde{r}_1, \tilde{r}_2, \dots, \tilde{r}_n$ are unknown residues. Poles are initialized by distributing N of these linearly or logarithmically over the frequency range of interest. Equation (4.2) can be rewritten as

$$\sum_{n=1}^N \frac{\hat{r}_n}{s + \bar{p}_n} - \left(\sum_{n=1}^N \frac{\tilde{r}_n}{s + \bar{p}_n} \right) f(s) \cong f(s) \quad (4.3)$$

An overdetermined least squares problem is obtained by evaluating (4.3) at a given number M of frequency samples in matrix form as follows:

$$\mathbf{A}\mathbf{x} = \mathbf{b} \quad (4.4)$$

where \mathbf{A} is the $M \times 2N$ matrix of known coefficients from (4.3), \mathbf{x} is the vector (column matrix) with the $2N$ unknown residues and \mathbf{b} is the vector with the values of function $f(s)$ at the M

chosen frequencies. An arbitrary row of A corresponding to the k th frequency sample would have the following form [7]:

$$A_k = \left[\frac{1}{s_k + \bar{p}_n} \dots \frac{1}{s_k + \bar{p}_N} - \frac{1}{s_k + \bar{p}_n} f(s_k) \dots - \frac{1}{s_k + \bar{p}_N} f(s_k) \right].$$

Thus [7]:

$$\mathbf{x} = \begin{bmatrix} \hat{r}_1 \dots \hat{r}_N & \tilde{r}_1 \dots \tilde{r}_N \end{bmatrix}^T$$

and

$$\mathbf{b} = [b_1, b_1, \dots, b_M]^T$$

with

$$b_k = f(s_k).$$

Matrix A and vector b are further built separating the real and imaginary parts; thus there are two equations associated to each frequency value. Special care is taken to accommodate complex conjugate pairs in successive rows of A [7].

$$\begin{bmatrix} \text{Re}(A) \\ \text{Im}(A) \end{bmatrix} \mathbf{x} = \begin{bmatrix} \text{Re}(\mathbf{b}) \\ \text{Im}(\mathbf{b}) \end{bmatrix}$$

Equation (4.4) is solved through an iterative process and super-indexes are introduced as follows to keep record of iteration steps:

$$\mathbf{A}^{(j-1)} \mathbf{x}^{(j)} = \mathbf{b} \quad (4.5)$$

As it has been already mentioned $\mathbf{A}^{(0)}$ is found with the initial poles distributed either linearly or logarithmically over the frequency range of interest for the fitting of $f(s)$ [7].

After finding the solution of (4.5) at the first iteration, from the obtained residues the second step is to recalculate the zeros of the fitted transfer function $f(s)$. This is achieved by computing the eigenvalues of the matrix \mathbf{Q} [7]:

$$\mathbf{Q} = \mathbf{W} - \mathbf{g}\tilde{\mathbf{x}}^T \quad (4.6)$$

where \mathbf{W} is a diagonal matrix containing the poles \bar{p} of all frequency samples, \mathbf{g} is a column vector of ones and $\tilde{\mathbf{x}}$ contains the \tilde{r} terms only. The explanation to this is as follows. Rewrite expression (4.2) as

$$\frac{\sum_{n=1}^N \frac{\hat{r}_n}{s + \bar{p}_n}}{\sum_{n=1}^N \frac{\tilde{r}_n}{s + \bar{p}_n} + 1} = \frac{\prod_{n=1}^{N'} (s + \hat{z}_n)}{\prod_{n=1}^N (s + \tilde{z}_n)} \cong f(s). \quad (4.7)$$

From (4.7) it is apparent that the cancellation of pole products makes the zeros \tilde{z} to become the poles of $f(s)$. Since the left-hand side denominator of (4.7) can be represented as:

$$\sum_{n=1}^N \frac{\tilde{r}_n}{s + \bar{p}_n} + 1 = \frac{\prod_{n=1}^N (s + \tilde{z}_n)}{\prod_{n=1}^N (s + \bar{p}_n)} \quad (4.8)$$

the zeros \tilde{z} are obtained by finding the roots of:

$$\sum_{i=1}^N \left(\tilde{r}_i \prod_{n=1, n \neq i}^N (s + \bar{p}_n) \right) + \prod_{n=1}^N (s + \bar{p}_n) = 0 \quad (4.9)$$

which is equivalent to finding the eigenvalues of \mathbf{Q} in (4.6).

The newly found set of poles can be simply replaced in (4.1) to determine the residues r_n . This is again an over-determined linear system. The desired fitting error limit is tested at this stage for each sample $f(s)$. If the error is not acceptable, the new poles are used to restart the procedure with (4.3). If the error limit is not met after a pre-specified number of iterations the order of approximation N is increased and the iterative procedure is restarted [7].

Even if the initial poles are not chosen adequately VF is capable of finding a solution at the expense of more iterations. If an iteration yields unstable poles, these are simply flipped to the left-hand-side of the complex plane and a new solution is searched [7].

4.2 Weighted Vector Fitting

WVF basic relation is [7]:

$$\frac{\sum_{n=1}^N \frac{\hat{r}_n}{s + \bar{p}_n}}{\sum_{n=1}^N \frac{\tilde{r}_n}{s + \bar{p}_n} + 1} \cong f(s). \quad (4.10)$$

The theoretical foundation of the WVF identification problem is the following minimization:

$$\min \left| \frac{1}{\sum_{n=1}^N \frac{\tilde{r}_n}{s + \bar{p}_n} + 1} \left[\sum_{n=1}^N \frac{\hat{r}_n}{s + \bar{p}_n} - \left(\sum_{n=1}^N \frac{\tilde{r}_n}{s + \bar{p}_n} + 1 \right) f(s) \right] \right|. \quad (4.11)$$

The VF method discards the left-most factor outside the square brackets at (4.11), while in WVF it constitutes a weight [7]. This weight is maintained through an iterative process. For the first iteration the weighting function can be estimated by analysis of the asymptotic behavior of the unknown partial fractions as [7]:

$$C^{(1)}(s) \cong \frac{\tilde{r}_n^{(1)}}{s + \bar{p}_n^{(1)}} + 1. \quad (4.12)$$

In WVF it is proposed to estimate $\tilde{r}_n^{(1)}$ and $\bar{p}_n^{(1)}$ by approximating the frequency domain response of $f(s)$ with a first order partial fraction expression. This first order approximation maintains the magnitude and shape of N th order function $C(s)$ sufficiently close to the exact value to produce acceptable starting values. At a subsequent iteration j , the weighting term $C(s)$, can be approximated by:

$$C^{(j)}(s) \cong \sum_{n=1}^N \frac{\tilde{r}_n^{(j-1)}}{s + \bar{p}_n^{(j-1)}} + 1 \quad (4.13)$$

The system of equations for WVF is

$$\mathbf{A}'^{(j-1)} \mathbf{x}^{(j)} = \mathbf{b}' \quad (4.14)$$

where primed values are found by dividing each frequency row by the corresponding weighting factor $C^{(j)}(s_k)$ [7].

In WVF as well as in VF if in some cases an iteration yields unstable poles, such poles are simply flipped into the left complex plane and a new solution is searched [7].

4.3 Fitting of the Characteristic Admittance Matrix

In the case of the fitting of the characteristic admittance matrix, common poles are calculated from the trace but can also be calculated from the matrix [7]. These poles are used to fit Y_c in the phase domain. Thus, each element of Y_c has the same set of poles. The approximation is thus of the following form [7]:

$$Y_c(s) = \sum_{n=1}^N \frac{c_n}{s - p_n} + d. \quad (4.15)$$

Note that the terms c_n and d in (4.15) represent matrices of residues.

4.4 Fitting of the Propagation Function Matrix

The approximation of H is much more difficult than that of Y_c since each propagation mode contributes to each element of H . Thus, the propagation function is first fitted in the modal domain in order to extract time delays and poles which are used for the fitting of the whole H matrix in phase domain. The process is summarized by following steps [7]:

1. Calculation of modal propagation parameters using frequency dependent transformation matrices.

2. Application of tracking routine to avoid artificial mode switchover [37].
3. Identification of time delays for each propagation mode.
4. Grouping of modes having identical or nearly identical time delays.
5. Fitting of the scalar propagation functions for each delay group with WVF combined with a time delay search scheme.
6. Fitting of \mathbf{H} in phase domain using poles and time delays obtained in 5.

The overall idea of this approach can be formulated as follows [7]

$$\tilde{\mathbf{H}}(s) = \sum_{m=1}^M \sum_{n=1}^{N(m)} \frac{\mathbf{c}_{m,n}}{s - p_{m,n}} \exp(-s\tau_m) \quad \text{such that} \quad (4.16)$$

$$\min_c \left\| \mathbf{H}(s) - \tilde{\mathbf{H}}(s) \right\|_2^2$$

where M is the number of delay groups, $N(m)$ is the number of poles for the m th delay group and τ_m is the time-delay. The poles $p_{m,n}$ are calculated using WVF and matrix residues $\mathbf{c}_{m,n}$ are calculated using least squares techniques.

4.5 Causality, Stability and Passivity

Several drawbacks have been found with the WB model and these are traced to the fitting utilities. There are many cases where the model renders non-convergent time-domain simulations for certain line terminations, such errors and “instabilities” have been traced back to the lack of passivity or passivity violations of the obtained rational approximations [36]-[40]. When VF is applied, the passivity of the obtained rational approximation cannot be guaranteed. An earlier fitting method was introduced in [2]. This is based on the Bode-diagram technique, it uses only real-valued poles and guarantees passivity [38]. On the other hand, however, this fitting method produces rational models of substantially higher order than those obtained with VF or WVF. Since by physical principles transmission lines and cables are passive devices, their models should also be passive. Recall that passivity guarantees stability and causality of the synthesized models [36].

Various techniques have been proposed to overcome passivity violations, these are referred

to as passivity enforcement [36]-[40]. Mention is made here that this is an ongoing research topic. Passivity enforcement techniques require the reformulation of previously obtained nonpassive models often through the perturbation of their components. Such solutions, however, often compromise the accuracy of the synthesized models.

It is shown in this chapter that the lack of passivity can often be cured by correctly addressing three simple aspects of the fitting process: 1) number of sample-data used in the representation of the Y_c and H matrices, 2) number of poles or fitting order and 3) mode grouping. It is shown here also that when aforementioned aspects are correctly addressed, passivity violations can be completely overcome, or at least decreased to a large extent, thus obtaining stable and causal time-domain simulations and avoiding the need of extra computationally-expensive procedures inside the fitting process. A model is said to be causal when the output given by the model is the consequence of a previous input, *i.e.*, the model must not respond before the input has been given [36].

Several examples of dc and ac cables, as well as of aerial lines, are presented in this chapter. These examples are analyzed with the EMTP-RV software to show the advantages of considering the previously mentioned three aspects of the fitting process. Test circuits used for these examples are not practical and the reader must be aware that they are used for numerical testing purposes only.

4.6 Passivity

4.6.1 Passivity test

The passivity test adopted in this chapter is the one used in [38]. The test is based on the fact that, when the line model is treated as a multi-port electrical network, passivity is guaranteed if and only if its transfer admittance matrix $Y_n(s)$ (with $s = j\omega$) has a purely positive real part through the whole frequency range [8]. Thus, If

$$\begin{bmatrix} I_0 \\ I_L \end{bmatrix} = Y_n \begin{bmatrix} V_0 \\ V_L \end{bmatrix} \quad (4.17)$$

then $Y_n(s)$ can be easily obtained as a function of $Y_c(s)$ and $H(s)$ as follows [8]:

$$\mathbf{Y}_n = \begin{bmatrix} (\mathbf{U} - \mathbf{H}^2)^{-1}(\mathbf{U} + \mathbf{H}^2)\mathbf{Y}_c & (\mathbf{U} - \mathbf{H}^2)^{-1}(-2\mathbf{H})\mathbf{Y}_c \\ (\mathbf{U} - \mathbf{H}^2)^{-1}(-2\mathbf{H})\mathbf{Y}_c & (\mathbf{U} - \mathbf{H}^2)^{-1}(\mathbf{U} + \mathbf{H}^2)\mathbf{Y}_c \end{bmatrix} \quad (4.18)$$

where \mathbf{U} is the identity unit matrix. The following conditions are necessary and sufficient for the admittance matrix \mathbf{Y}_n to be positive real [8]:

- 1) $\mathbf{Y}_n(s)$ is analytic at every value of s such that $\text{Re}(s) > 0$
- 2) $\mathbf{Y}_n(s) = \mathbf{Y}_n(s^*)$
- 3) $\mathbf{Y}_H(s) = \mathbf{Y}_n^T(s^*) + \mathbf{Y}_n(s)$ (Hermitian matrix) is positive definite.

The first two conditions are fulfilled by VF since poles and residues always appear as complex conjugates [38]. To satisfy the third condition, all eigenvalues of $\mathbf{Y}_H(s)$ must be positive for every frequency ω . Thus, the test is based in this third condition.

4.6.2 Effect of the number of data samples on passivity

The matrices \mathbf{Y}_c and \mathbf{H} to be fitted are first obtained as in (4.15) and (4.16) for a given number of frequency samples into a certain frequency range. The frequency range is well established at the specialized EMT literature and is related to the type of simulation that is to be conducted. On the other hand, however, the number of samples to be used is left to user judgment. In most cases and at some EMTP-type programs the used value is 10 samples per decade (SPD). Although, this value can be adequate for many applications, it is shown here that a low number of samples can misrepresent the true form of the \mathbf{H} matrix leading to a nonpassive rational model.

The above mentioned situation is shown next on the case of a 15 km long dc cable whose transversal geometry is depicted at Figure 4-1. Additional data required for an EMT simulation are given at Table 4.1. Two sampling resolutions are applied in this example, one is at 10 SPD and the other is at 20 SPD, the simulation time step is $1\mu\text{s}$. Figure 4-2 provides plots for each one of the diagonal real parts of the \mathbf{Y}_c matrix obtained with both resolutions: 10 SPD in solid lines and 20 SPD in dashed lines. It can be noticed in the figure that there is no significant difference between both results. This is due to the fact that the elements of \mathbf{Y}_c are very smooth along the whole frequency range. Thus, the \mathbf{Y}_c elements can be accurately represented with a small number of samples.

Figure 4-3 shows the plot of first diagonal element of the \mathbf{H} matrix that is obtained with 10 SPD in solid lines and of the same element as obtained with 20 SPD in dashed lines. It is apparent from this figure that the plots of \mathbf{H} elements can have a very different shape according to the number of data samples used in their representation. The reason for this is that \mathbf{H} elements often present a highly oscillatory behavior at high frequencies. Thus, if a small number of samples is used to synthesize the \mathbf{H} matrix, this may lead to an inaccurate, and even nonpassive, model.

Simulations are carried out next using both cases, 10 (dashed line) and 20 (solid line) samples per decade. The test circuit is as in Figure 4-4, where the current at the first conductor sending-end is monitored and plotted. Figure 4-5 shows both plots, the one with 10 SPD which is nonpassive, and the one with 20 SPD which is passive.

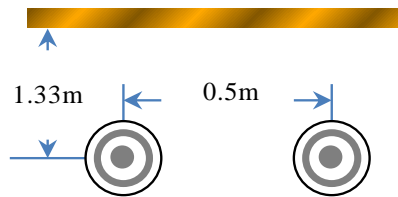


Figure 4-1 : RTE dc-cable system's layout.

Table 4.1 : RTE dc-Cable Provenance and Data

Case proposed by RTE, Provided by Hani Saad	
Radius of inner solid conductor (m)	0.032
Resistivity nuclei/sheath (ohm/m)	1.72e-8/2.83e-8
Inner/Outer radius of sheath (m)	0.0569/0.0582
Relative permittivity of 1st & 2nd insulation	2.5

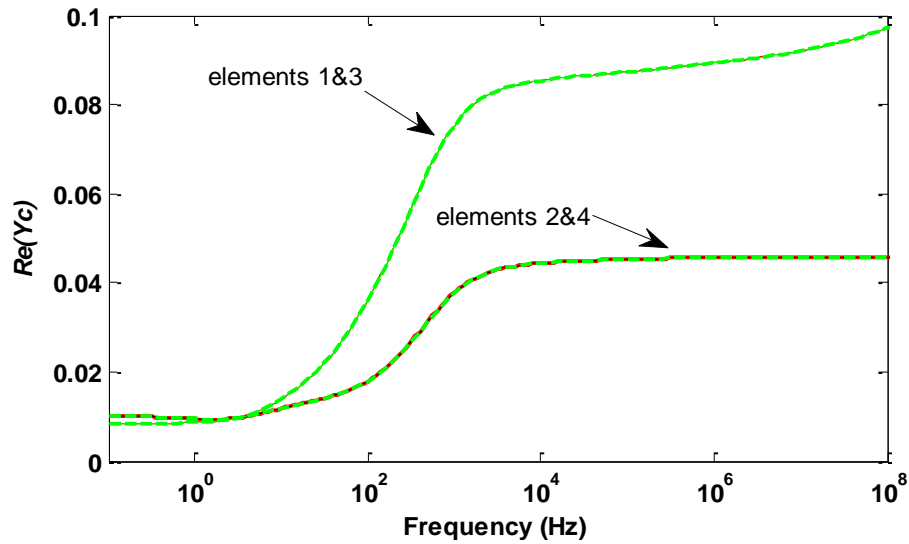


Figure 4-2 : RTE dc-cable real part of Y_c diagonal elements. Solid line for results with 10 SPD, dashed line for results with 20 SPD.

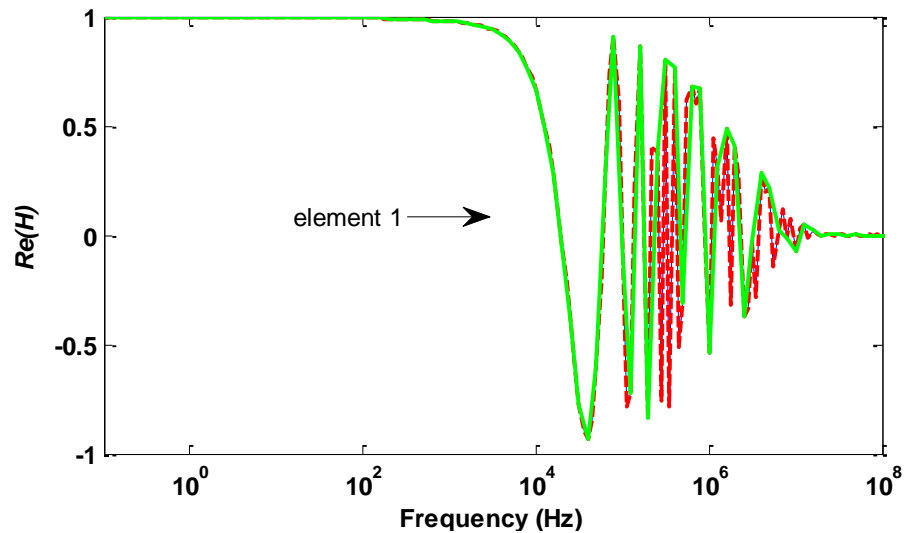


Figure 4-3 : RTE dc-cable real part of H diagonal elements. Solid line for results with 10 SPD, dashed line for results with 20 SPD.

To gain a better understanding of the differences obtained at the previous example the passivity test of section 4.6.1 is applied. Figure 4-6 shows the results for the 10 SPD case and Figure 4-8 provides the ones corresponding to the 20 SPD case. Figure 4-7 further provides a close up to Figure 4-6, where passivity violations are fairly evident and small passivity violations

in the 7,493Hz-25,119Hz range are present. On the other hand, for the results obtained with 20 SPD the model shows no passivity violations at all. For this last case, all eigenvalues are positive through the whole frequency range. It can thus be affirmed that erroneous simulations often are the result of passivity violations that may be cured by improving the rational approximations of Y_c and H and that this is often accomplished by increasing the number of data samples used to describe both matrices. At the moment of the writing of this thesis there is not automatic way to determine the appropriate number of samples for the synthesis of rational Y_c and H . Nevertheless, in view of the previously reported findings, a recommendation is issued here as to try increasing the data samples used in the fitting process when a nonpassive condition is detected.

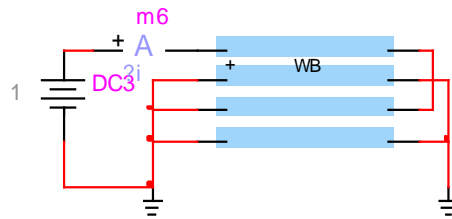


Figure 4-4 : RTE dc-cable test circuit (numerical test only).

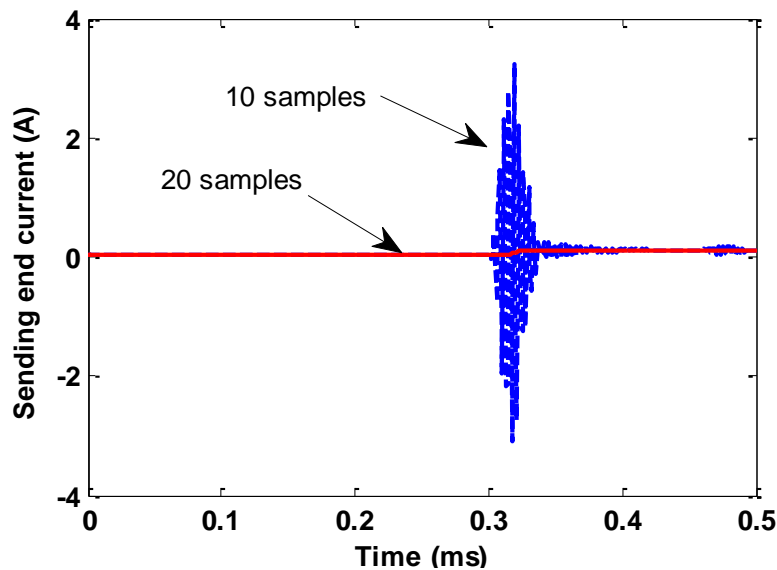


Figure 4-5 : RTE dc-cable current waveforms at the sending end. Solid line are results with 20 SPD, dashed line are results with 10 SPD.

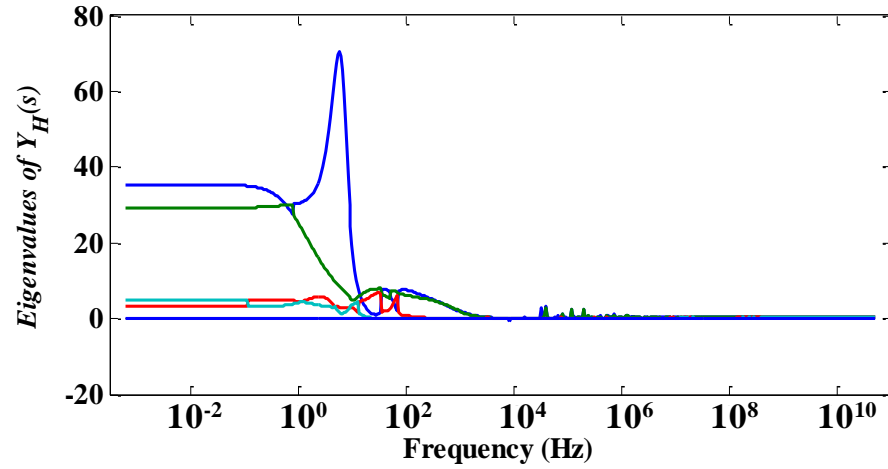


Figure 4-6: RTE dc-cable passivity test results for 10 SPD case.

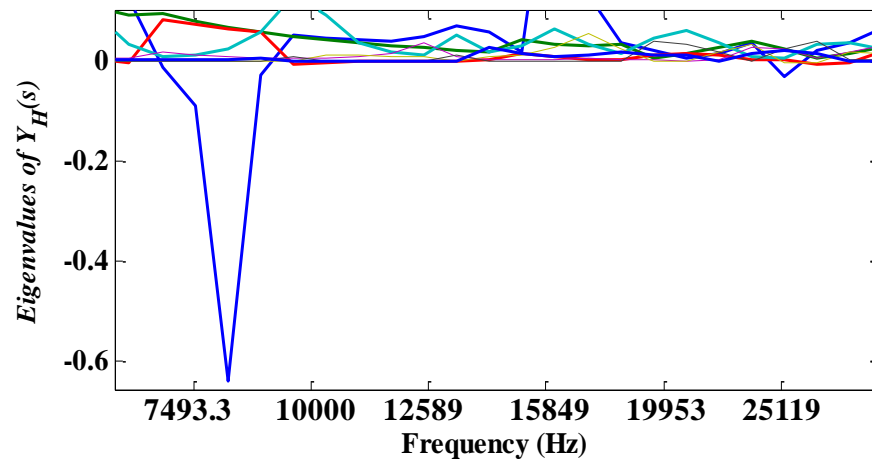


Figure 4-7: RTE dc-cable passivity test results for 10 SPD case close up.

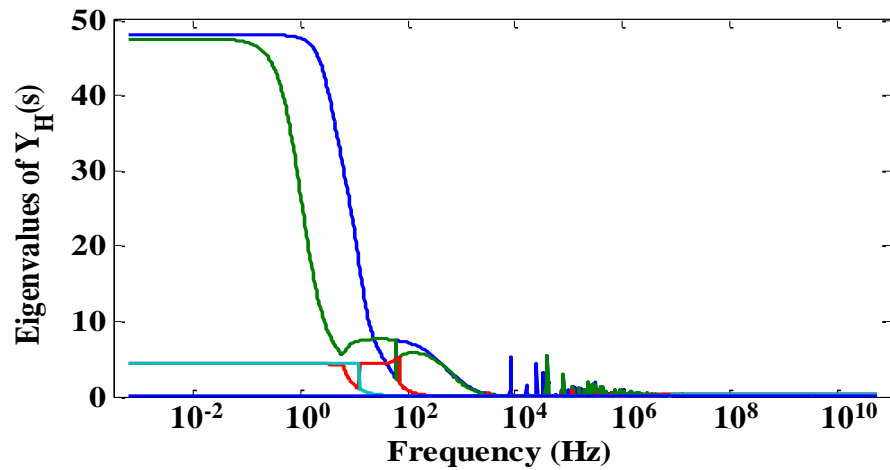


Figure 4-8: RTE dc-cable passivity test results for 20 SPD case.

4.6.3 Effect of fit order on passivity

The improvement of a rational approximation by increasing the number of poles (fit order) also helps to alleviate passivity violations. This is due to the fact that obtained rational models are not always sufficiently accurate and this often causes passivity violations leading to incorrect time domain simulations. At the fitting process, the number of poles used for the rational representation of \mathbf{Y}_c and \mathbf{H} is closely related to the error in the obtained rational model. Typical VF implementations for synthesizing phase-domain line models start the fitting process by giving one pole and trying to fit the given matrix with this single pole, after the fitting is done the error is measured and if this is greater than a pre-specified value, another pole is added and the fitting is done again with the poles. The process of adding poles is repeated until the specified error criterion is fulfilled or until the specified maximum number of poles is reached [26].

Generally, a tradeoff between accuracy and model order is desired. Thus, the error is selected not too low to obtain compact rational models. In general, an absolute error figure of 0.01 gives accurate approximations. In some cases, however, this results in synthesized nonpassive models. It is shown in this section that increasing the number of poles often eliminates passivity violations.

Since the elements of the \mathbf{Y}_c matrix are very smooth functions through the entire frequency range, its elements can be accurately represented with a reduced number of poles. On the other hand, the elements in the \mathbf{H} matrix are less regular functions of the frequency and a flawed rational approximation often is obtained when the fit is done with a small number of poles. The next example shows how, by increasing the number of poles, the rational approximation of the \mathbf{Y}_c and \mathbf{H} matrices are improved and passivity violations are cured.

The following example consists of a 12-phase, 256 m long cable whose transversal layout is shown in Figure 4-9. The cable data and case provenance are given in Table 4.2. The test circuit considered here is shown in Figure 4-10. Stress is made here that this configuration is considered here for numerical tests only. All the elements of \mathbf{Y}_c and \mathbf{H} are fitted first with an error-level specification of 0.01. With this value good approximations are obtained for \mathbf{Y}_c and for most elements of \mathbf{H} . Nevertheless, some elements of \mathbf{H} are not well fitted in the low frequency region. This is shown in Figure 4-11 where the element (1,2) of the \mathbf{H} matrix is plotted in solid

line along with its approximation in dashed line.

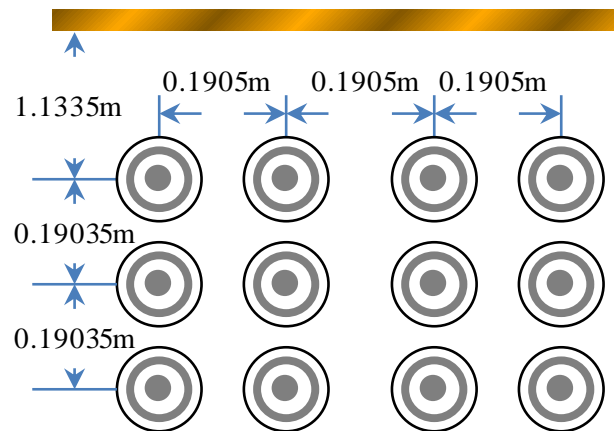


Figure 4-9: Mader ac-distribution 12-phase cable layout.

Table 4.2 : Mader ac-distribution 12-phase Cable's Provenance and Data

Case proposed by Mr. Mader, Provided by Jean Mahseredjian	
Radius of inner solid conductor (m)	0.01238
Resistivity nuclei/sheath (ohm/m)	1.7e-8/1.7e-8
Inner/Outer radius of sheath (m)	0.02469/0.025326
Relative permittivity of 1st & 2nd insulation	2.48/2.3

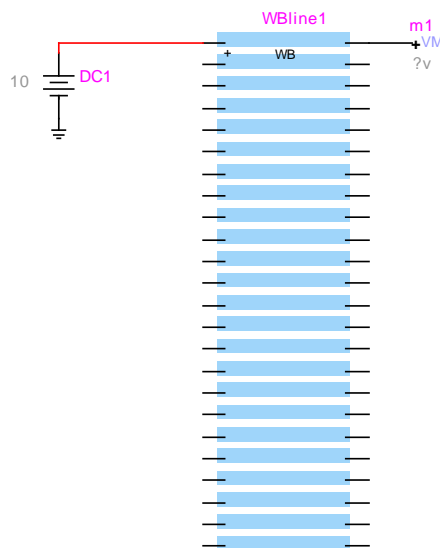


Figure 4-10: Mader ac-distribution 12-phase cable test circuit.

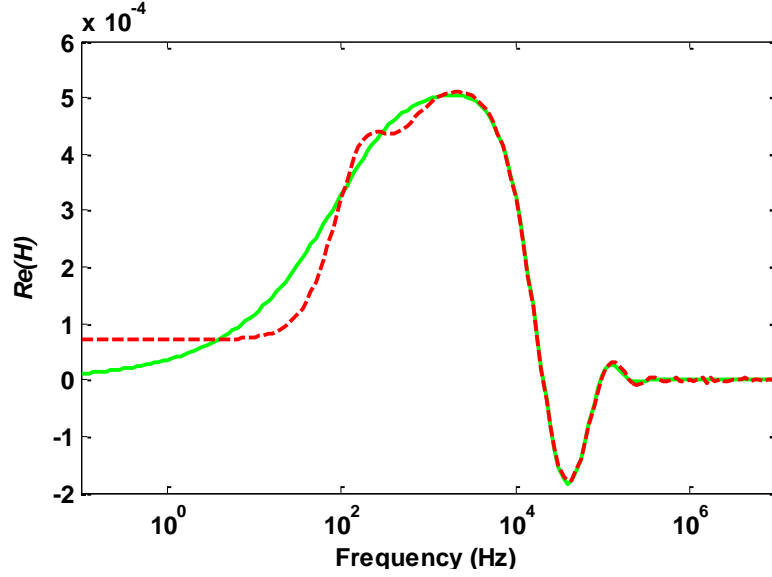


Figure 4-11: Mader ac-distribution 12-phase cable. Real part of element (1,2) in matrix \mathbf{H} fitted with 2 poles. Solid line is the original value, dashed line is the fitted one.

For this case 8 poles were used for the fitting of the \mathbf{Y}_c matrix and 48 poles (2 poles per mode) for the one of the \mathbf{H} matrix. Passivity test results are shown at Figure 4-12 and a close up is given in Figure 4-13. It can be noticed in these figures that small passivity violations in the order of $-1e-5$ are present in the range 10Hz-32 kHz. These passivity violations are reduced by increasing the number of poles. Using 19 poles to fit the \mathbf{Y}_c matrix and 96 poles (4 poles per mode) to fit the \mathbf{H} matrix, which represents an approximation error of 0.001. Figure 4-14 provides the plot for the improved representation of element (1,2) of the \mathbf{H} matrix; this figure should be compared with Figure 4-11. Figure 4-15 shows the results of the new passivity test. Although the passivity violations are still present in the range 1Hz-32 kHz, their magnitudes have been reduced to a level lower than $-2e-6$.

Simulations using both rational approximations, with 0.01 and 0.001 absolute error levels, are carried out next. Figure 4-16 shows the voltage waveforms at the receiving end of the first core when at the sending end this core is excited with a 10 V step function for numerical evaluation purposes. It can be noticed in this figure that the simulation with the higher approximation error becomes divergent after 0.5ms of simulation, whereas the simulation with the lower approximation remains convergent until the end of the simulation. The time step used in the simulation is $0.1\mu\text{s}$ because the smallest travel time along the cable system is $1.3170\mu\text{s}$.

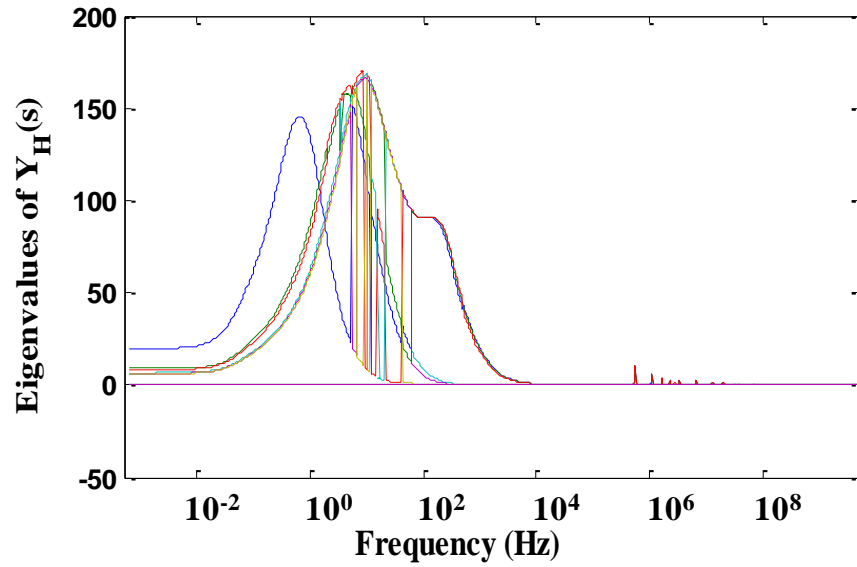


Figure 4-12: Mader ac-distribution 12-phase cable. Passivity test result for a 0.01 level of absolute approximation error.

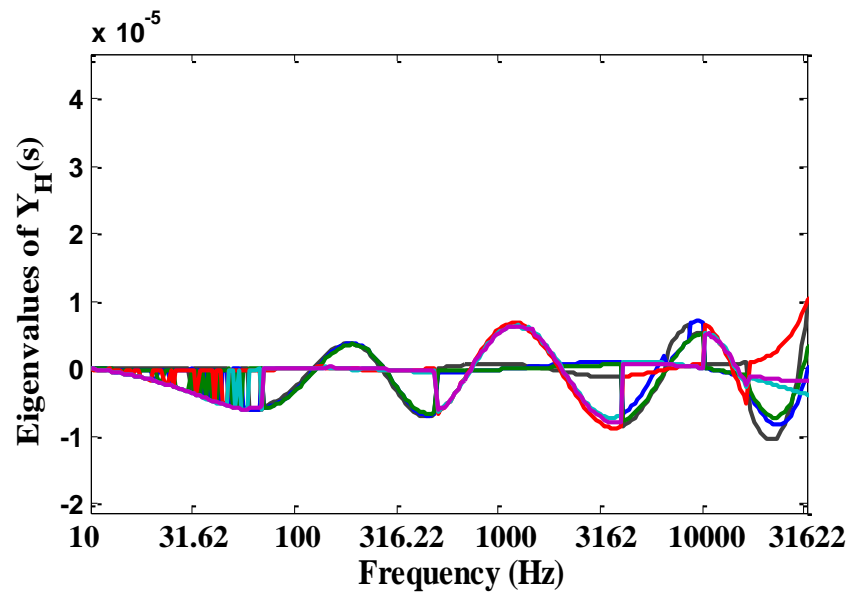


Figure 4-13: Mader ac-distribution 12-phase. Passivity test results close-up for the 0.01 level of absolute fitting.

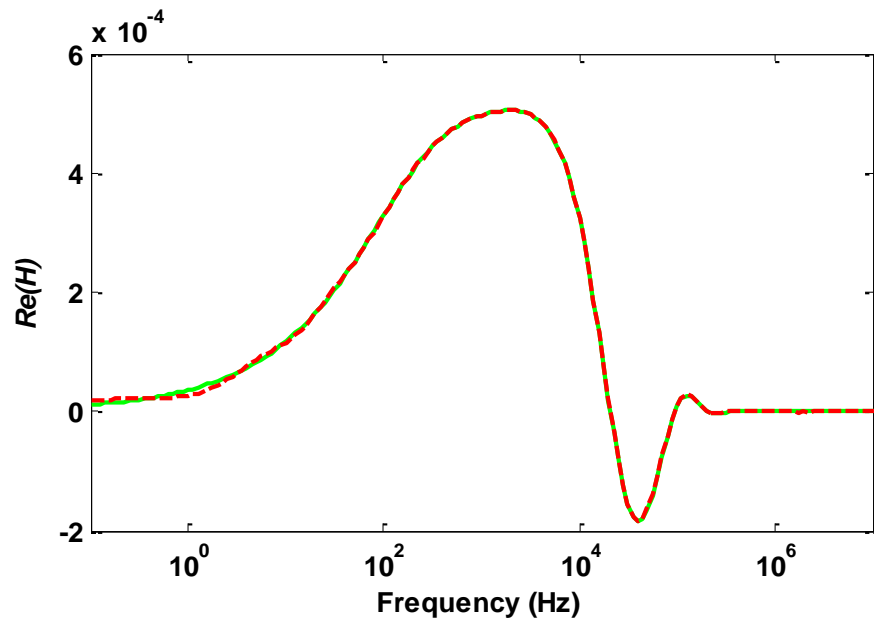


Figure 4-14: Mader ac-distribution 12-phase cable. Real part of element (1,2) of \mathbf{H} matrix fitted with 4 poles. Solid line is for original function values, dashed line is for fitted values.

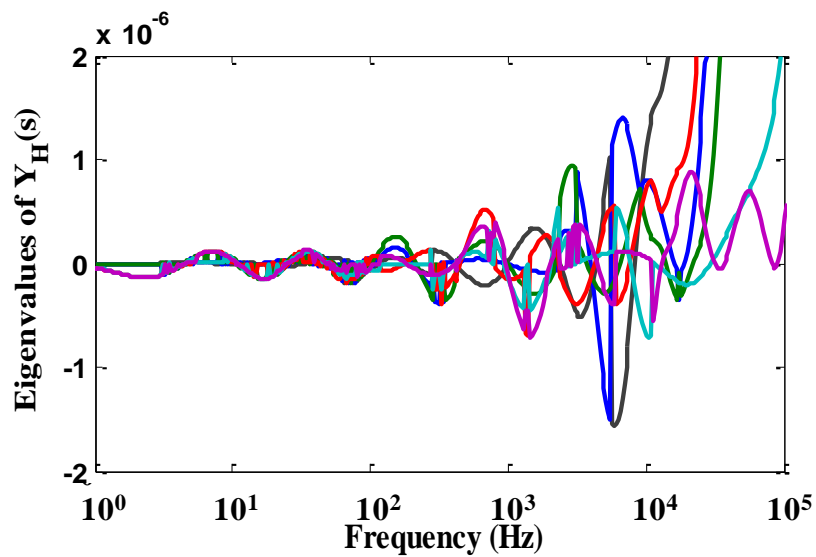


Figure 4-15: Mader ac-distribution 12-phase cable. Passivity test results close-up for the 0.001 level of absolute fitting.

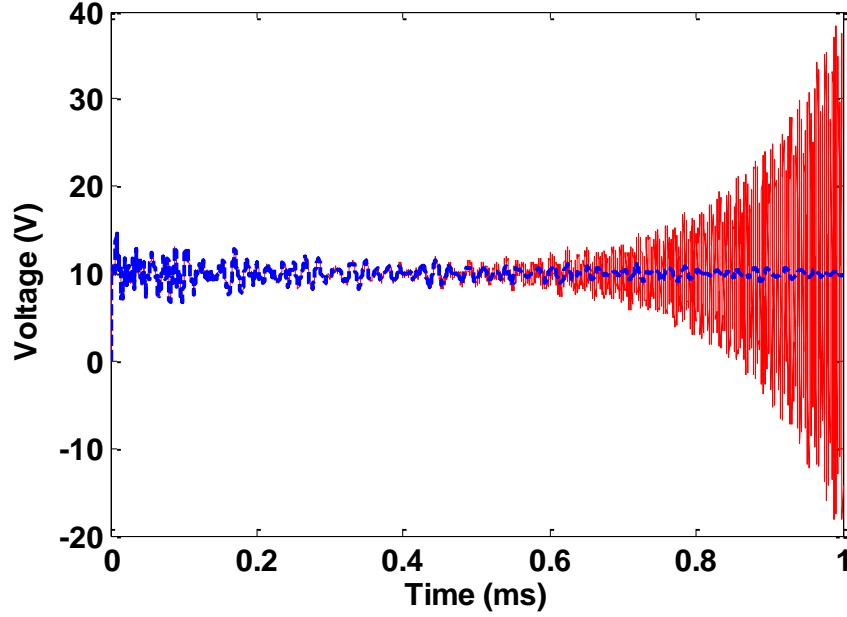


Figure 4-16: Mader ac-distribution 12-phase cable. Sending end current waveforms. Solid line corresponds to the 0.01 error level approximation case, dashed line is for the 0.001 error-level case.

It should be stressed at this point that keeping on increasing the number of poles in a rational approximation does not guarantee the elimination of passivity violations. In this author's experience, increasing the number of poles is good until a 0.001 of absolute error level when using the WVF tool. After this point, passivity violations will not decrease anymore regardless of the number of added poles and if these poles are not well located, the passivity violations may be increased.

4.6.4 Effect of modal grouping on passivity

Since the appearance of phase domain line models a standard practice when realizing the fitting of \mathbf{H} , is the grouping of modal propagation functions with equal and nearly equal phase angles and time delays into a single group. This is for the sake of improving the computational performance of the synthesized models [6],[16],[19],[20]-[24],[38],[39],[41]. The obtained group is the arithmetical average of the conforming modal contributions and the smallest time delay is designated as the group time delay [7],[19].

It is shown in this chapter that grouping modal propagation functions by considering only the similitude of phase angles and time delays can stiffen the fitting process. This often results in

the misrepresentation of the original modal propagation functions which in turn can render a nonpassive rational model. A simple approach to solve this problem is to completely avoid modal grouping. Nevertheless, since modal grouping certainly increases the computational efficiency of line models, the issue is pursued further in this thesis. It is thus proposed here that, in addition to the similitude of mode angles, the relative magnitudes among the considered modal components to be grouped should be considered too. If these magnitudes are almost similar through the whole frequency range then a group is formed. The criterion used to test for magnitudes similarity is based on the RMS differences among the magnitudes of the modal propagation functions to be grouped. After several tests it has been determined that the obtained RMS differences should not be greater than $1e-4$. The RMS differences between two modal propagation functions $H_{m,i}(\omega)$ and $H_{m,k}(\omega)$ is obtained as follows:

$$D_{i,k} = \sqrt{\sum_{l=1}^M \left(|H_{m,i}(\omega_l)| - |H_{m,k}(\omega_l)| \right)^2} \leq 1e^{-4}$$

where $\omega_1, \omega_2, \dots, \omega_M$ are the M frequency samples used to represent the modal propagation functions as discrete frequency functions. The experience at the research work being reported here is that, by applying the above RMS-difference criterion, many passivity problems are cured, while the high computational efficiency of the synthesized models is preserved. Maintaining a compact rational model is particular important at real-time applications where the computational speed is a critical feature. It is shown in [42] that the original implementation of the ULM or WB line model requires a total of 16 flops per pole, while in a model proposed here and described in the following chapter the update of the states requires an average of 2.5 flops per pole. In any case, the reduction in the number of poles reduces the number of operations performed by the line model and this speeds up the simulations.

As an example, consider the 6.67km long ac transmission cable whose transversal layout is shown in Figure 4-17. The cable data and provenance are given in Table 4.3. For this case the rational fit has been obtained first by grouping modal components in the traditional way, then by disabling the grouping and, finally, by applying the previously proposed criterion. As the modal grouping is performed in the conventional manner, four delay groups are formed, one of these includes three modal components. Each group is fitted with 20 poles given a total of 80 poles for

the description of the \mathbf{H} matrix. The passivity test shows that the obtained model presents large passivity violations at the low frequency region. This is shown at Figure 4-18. When mode grouping is disabled the number of obtained groups is evidently 6, each one being fitted with 20 poles to give a total of 120 poles. Figure 4-19 shows the results of passivity test being applied to this model. It can be seen there that the passivity violations have disappeared.

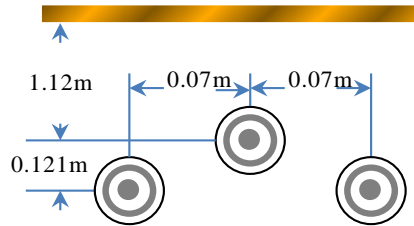


Figure 4-17: EDF ac-cable layout.

Table 4.3 : EDF ac-Cable Data and Provenance

Case proposed by EDF and provided by Jean Mahseredjian	
Radius of inner solid conductor (m)	0.015
Resistivity nuclei/sheath (ohm/m)	4.25e-8/2.84e-8
Inner/Outer radius of sheath (m)	0.0258/0.0263
Relative permittivity of 1st & 2nd insulation	2.5

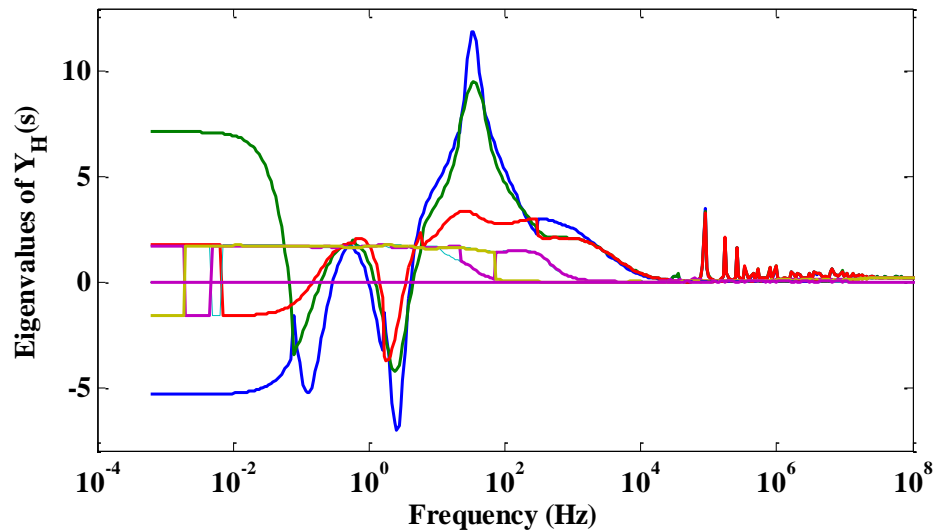


Figure 4-18: EDF ac-cable traditional grouping case passivity test results.

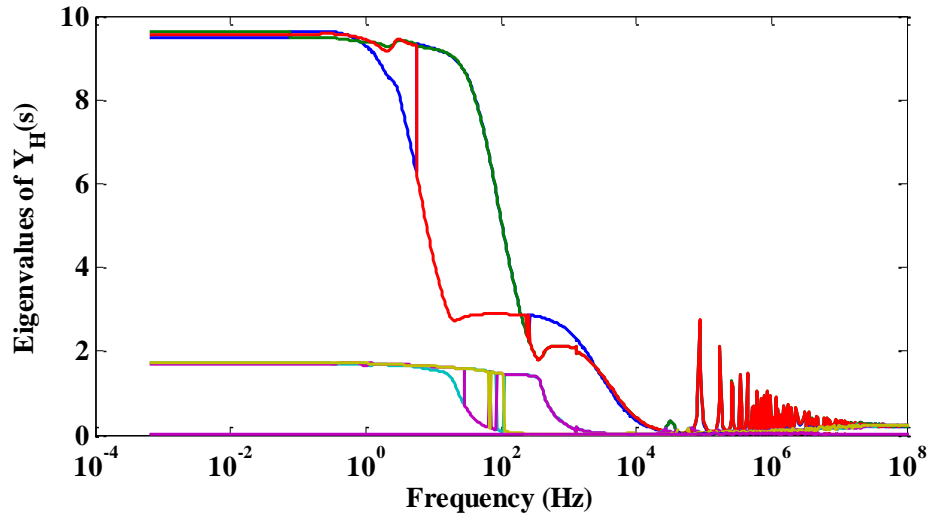


Figure 4-19: EDF ac-cable no grouping case passivity test results.

For this example Figure 4-20 shows the modal propagation functions magnitudes. It can be seen that elements 1-3 (which are originally selected for grouping) are very similar through the whole frequency range, except in the range 100 Hz-100 kHz where element 3 gets apart resulting in a RMS error of 0.124. Thus, when the proposed grouping method is applied modal propagation function 3 is left out of the group and just modal propagation functions 1 and 2 are grouped. The results of the passivity test are similar to those for the nongrouping case. Hence, the obtained rational model is passive and compact with 5 delay groups and a total of 100 poles.

Time domain simulations were carried out using the three different rational models and a time step of 1 μ s. The simulation circuit is shown in Figure 4-21 where the line is energized at $t=0$. For this test, the receiving-end voltage-waveforms as obtained when using the rational model with traditional mode grouping (i.e. the nonpassive realization) are shown in Figure 4-22. One can observe in this figure numerical oscillations after 1 ms at the three phases. This behavior is not part of the transient phenomenon. When simulating with the passive rational models obtained, either by not grouping or by grouping according to the above described method the numerical oscillations disappear. This can be observed at Figure 4-23.

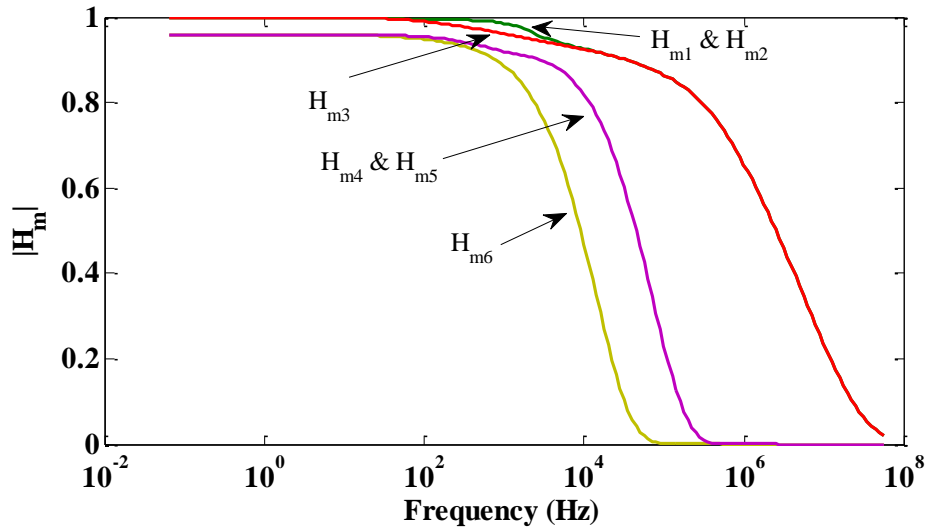


Figure 4-20: EDF ac-cable, modal propagation function magnitudes.

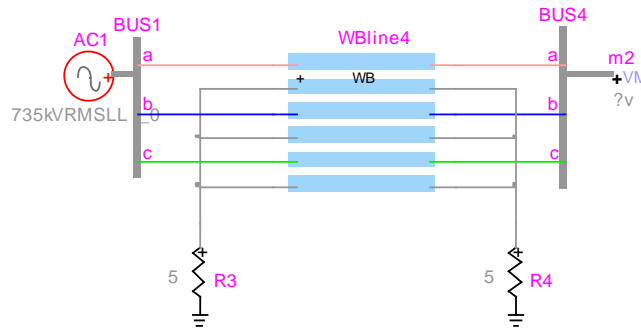


Figure 4-21: EDF ac-cable test circuit.

A second example to test the conventional practice of mode grouping consists in the BC HYDRO 9-Phase Aerial Line case already presented at section 3.7.2, where the line layout has been given at Figure 3-23 and the line data is given at the beginning of section 3.7.2. For this example the test circuit presented in Figure 4-24 is used and two cases are considered. The first case consists in the grouping of modal propagation parameters in the traditional way. At the second case the modal parameters grouping is performed in the previously proposed form. In the first case the time domain solution is divergent as shown in Figure 4-25. Such behavior is due to the passivity violations of the rational model. Figure 4-26 shows the passivity test results for the conventional-grouping case. A close up into this figure is provided in Figure 4-27 where a passivity violation of magnitude $7e-5$ can be observed close to the 1 GHz frequency, and small passivity violations in the order of $1e-6$ at the low frequency range 9Hz-1100Hz are present, see

Figure 4-28. By contrast, when mode grouping is performed in the proposed fashion no groups are created and the passivity violation in the high frequency region is cured, see Figure 4-29. Nevertheless, small passivity violations at the low frequency region prevail. However, is this author's experience that when passivity violations are very small, less than $1e-5$, time domain solutions are stable and accurate as shown in Figure 4-30 (also refer to [39]). The time step used for this simulation was $1 \mu s$.

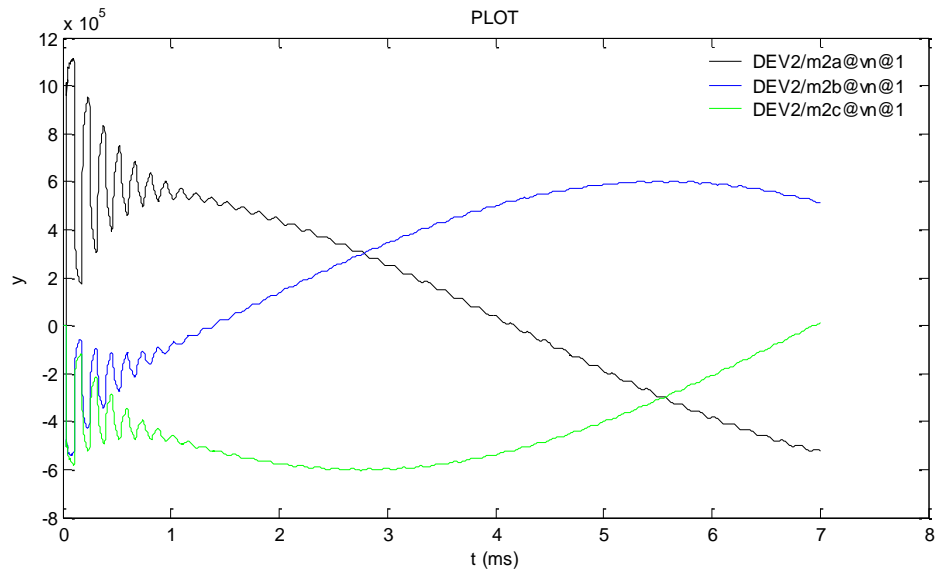


Figure 4-22: EDF ac-cable nonpassive case receiving end voltage waveforms.

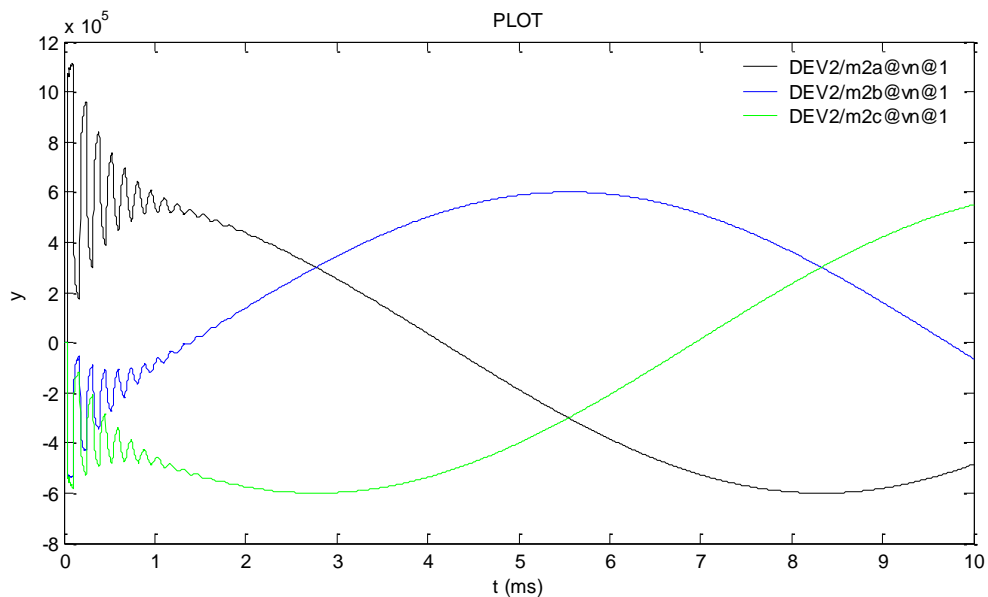


Figure 4-23: EDF ac-cable passive case receiving end voltage waveforms.

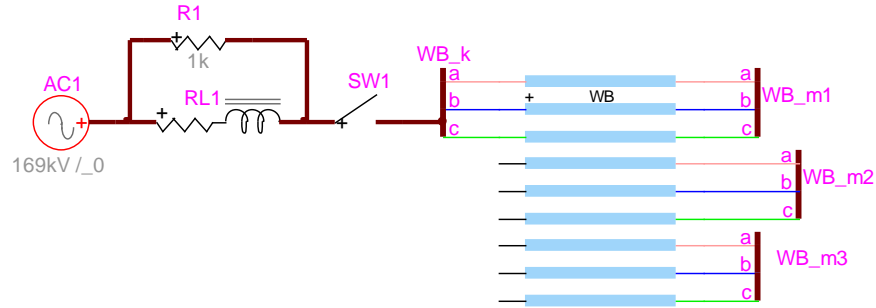


Figure 4-24 : BC HYDRO 9-phase aerial line layout, passivity study.

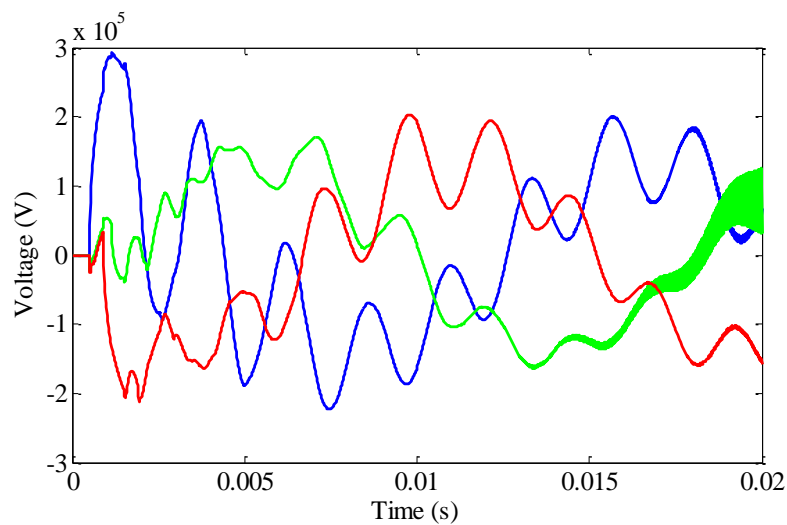


Figure 4-25 : BC HYDRO 9-phase aerial line. Voltage waveforms at the receiving end of circuit 1 nonpassive case.

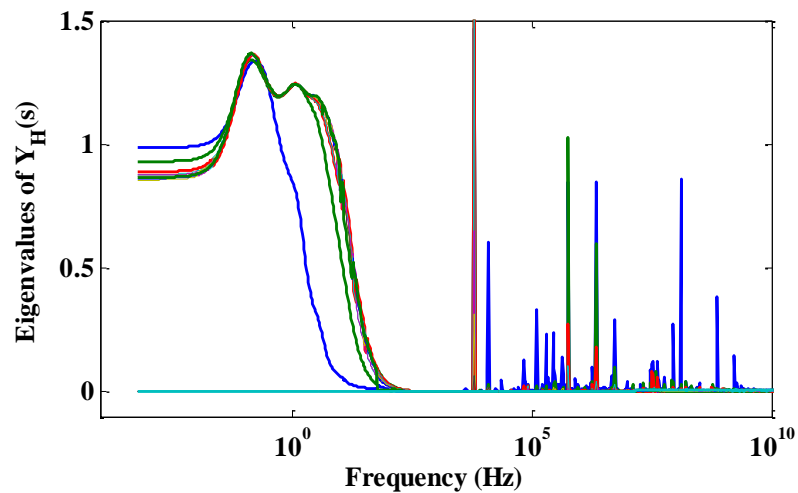


Figure 4-26: BC HYDRO 9-phase aerial line traditional grouping case passivity test results.

Figure 4-31 provides the magnitude plot of the modal propagation functions for the BC HYDRO 9-phase aerial line. According to the conventional grouping practice modes 1-3 should be selected to form a single delay-group. Nonetheless, the magnitudes of the propagation functions corresponding to these modes are very different at high frequencies as can be seen in Figure 4-31. The grouping of these modal propagation functions into a single one will not accurately represent the behavior of the original modal functions, since the added stiffness to the fitting process causes the passivity violations.

Consider again the case of section 4.6.3. If traditional mode grouping is allowed here, the resulting model will be nonpassive, even if one keeps on increasing the number of fitting poles. If modal grouping is performed by the proposed method, or simply avoided, the resulting model remains convergent as the number of poles is increased. In this case, the advantage of grouping as proposed here is that the number of delay groups reduces from 24 to 19 and this speed up the time-domain simulations.

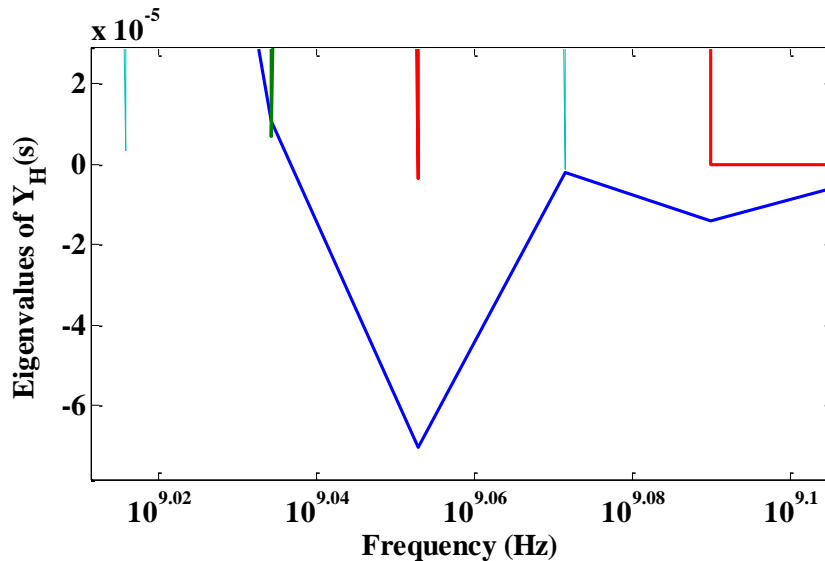


Figure 4-27: BC HYDRO 9-phase aerial line traditional grouping case, passivity test results close-up.

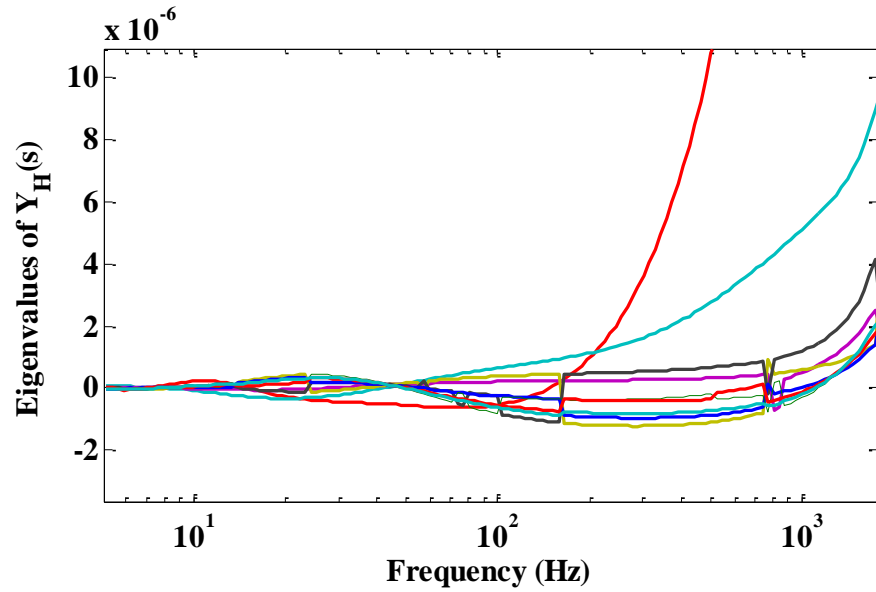


Figure 4-28: BC HYDRO 9-phase aerial line, proposed grouping case, passivity test results, close-up around the low-frequency range.

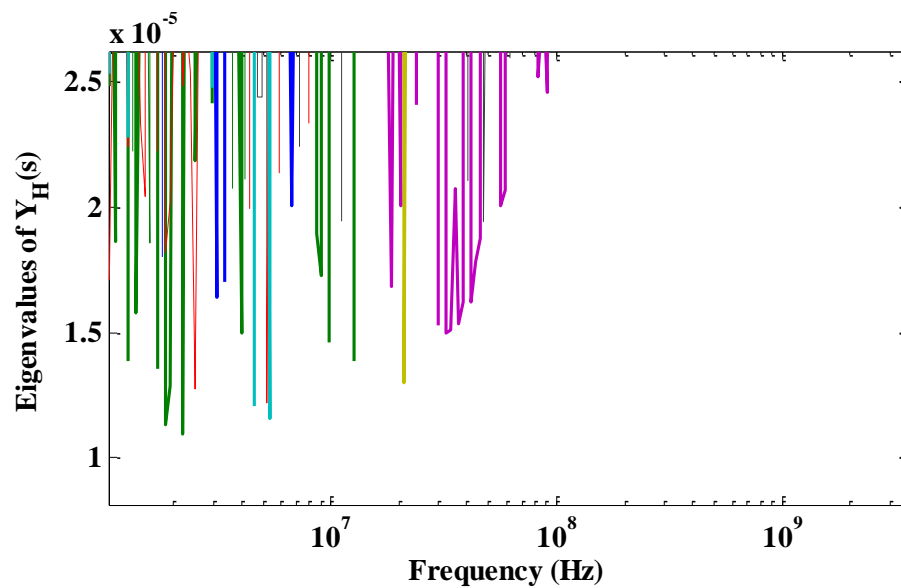


Figure 4-29: BC HYDRO 9-phase aerial line, proposed grouping case, passivity test results, close-up.

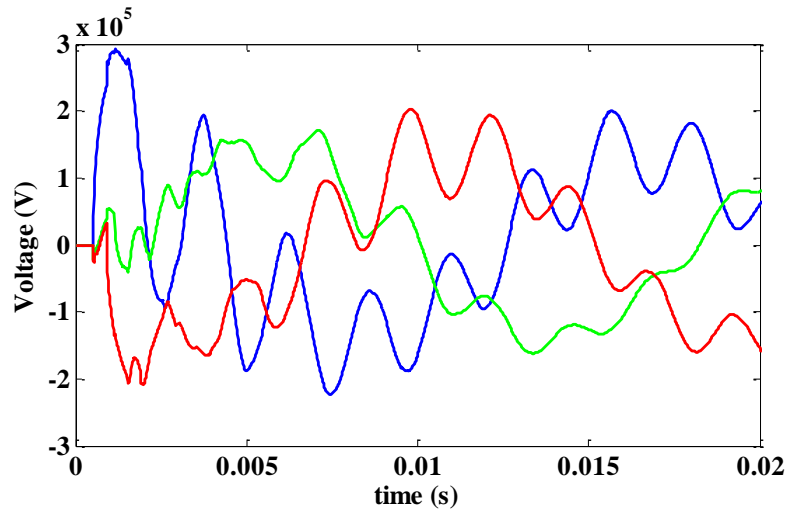


Figure 4-30 : BC HYDRO 9-phase aerial line. Voltage waveforms at the receiving end of circuit 1 passive case.

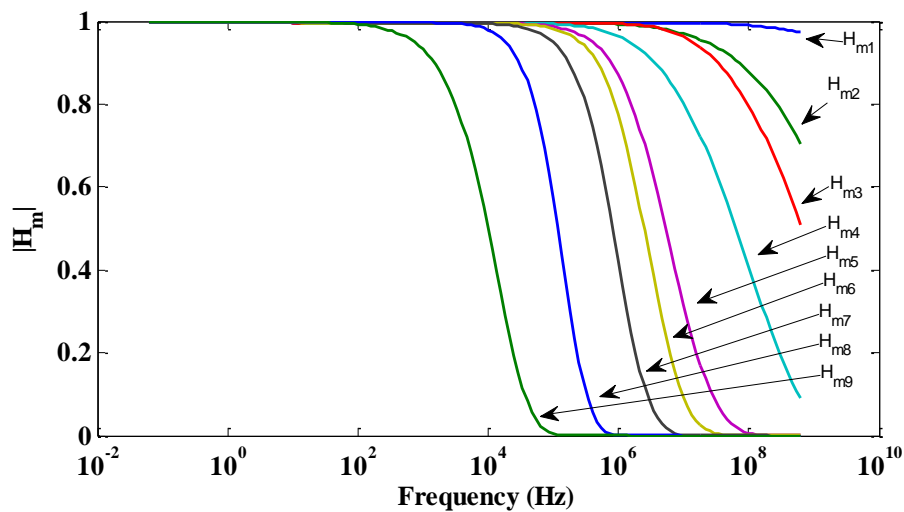


Figure 4-31: BC HYDRO 9-phase aerial line, modal propagation functions magnitudes.

4.7 Remarks

This chapter provides guidelines to avoid nonpassive behavior of multiconductor power-line and power-cable models that are synthesized by means of rational functions. Nonpassive models often exhibit behavior that departs from that of physical devices that they are supposed to represent. It has been shown in this chapter that many instances of passivity violations can be fixed by revising three simple aspects of the fitting process:

- 1) Providing a sufficient number of data samples at the fitting process of the Y_c and H

matrices.

2) The increase of the number of fitting poles often improves the accuracy of the fitted models and cures passivity violations.

3) In addition to phase-angle similarities, mode grouping should consider the magnitude similarities of the modal propagation functions being involve.

Taking care of the above three aspects can considerably decrease the occurrences of passivity violations at line and cable models and, if these still persist, their amplitude is decreased to a very small value in which time domain behavior is not divergent. Passivity enforcement methods, on the other hand, often result computationally-expensive.

CHAPTER 5 COMPUTATIONAL EFFICIENCY IMPROVEMENT

Essential to the WB line and cable model is the rational approximation of Y_c and H , the characteristic admittances and propagation functions matrices. This issue is dealt with in Chapter 4. At the original WB implementation (ULM), the Vector Fitting (VF) tool is used to fit these matrix functions. Nevertheless, VF can sometimes render nonpassive realizations which cause the model to fail. Improvements to this fitting technique have been proposed in the last few years; among these are the Orthonormal Vector Fitting (OVF) [43] and the Weighted Vector Fitting (WVF) [26] techniques. Their focus is on the reduction of the number of poles needed for the rational approximations, as well as on attaining more stable (passive) realizations. Although, the number of poles affects directly the numerical performance of the line model as explained in [42], there are other possible ways for substantially increasing its numerical performance.

One issue requiring special consideration, regarding the use of VF, OVF and WVF, is the handling of complex state variables produced by complex poles that may arise by using these fitting tools. The standard approach, which is the direct one, consists in treating all internal states as complex. In the case of real states, the imaginary parts are zeros. In the case of complex states, the imaginary parts must cancel each other since complex poles and states arise in conjugate pairs[22],[23],[42]. Clearly, this standard approach is inefficient. The alternative proposed here is to handle all state variables with real arithmetic [22],[42]. Various methods for doing this are proposed and analyzed here. By doing this, the computational-speed constraints imposed by real-time simulators can be overcome towards making the WB line model a suitable tool for real-time platforms.

As VF, OVF or WVF are applied to obtaining rational approximations of Y_c and H , some of the fitting poles may be complex. These poles and their associated state variables come in conjugate pairs. The imaginary parts of the state variables must cancel each others at the sums in (3.33) and (3.37). At the direct implementation of the WB model, as described in Chapter 3, all internal state variables are treated as complex, including those that are real. This approach is in fact the one adopted at standard implementations of the WB model (ULM) in EMTP-type programs. From the standpoint of computational efficiency, however, this direct approach introduces a large number of trivial and redundant computations [22], [42].

In this author's experience, complex poles arise less frequently in the fitting of Y_c than in the one of H and, at the latter only between 20 to 50% of the fitting poles may be complex. Thus, the handling of the real variables as complex will increase the number of sums at least by a factor of two and the number of real multiplications by a factor of four [22],[42]. In addition, all the added sums and multiplications are trivial; that is, sums of zeros and multiplications by zeros. For the case of complex state variables, the two states from a conjugate pair convey the same information; thus, the computation of these two is redundant [22],[42].

The handling of complex poles by real arithmetic allows to decrease dramatically the number of arithmetic operations performed by the model and, by virtue of this, its computational efficiency is boosted. This chapter introduces three new techniques to handle the internal state variables of the WB model efficiently and with real Arithmetic. The first technique is referred to here as first order blocks –or first order realizations, the second one is called second order blocks and the third one is called higher order blocks.

5.1 First Order Realizations: Complex States with Real Arithmetic

The first-order blocks technique is based on the replacement of each pair of complex-conjugate equations by two real equations that are coupled. This is explained as follows.

Assume that two fitting poles, either in (3.31) or in (3.35), are complex conjugates: $p = p_R + jp_I$ and $\bar{p} = p_R - jp_I$, where subscript R stands for the real part and subscript I stands for imaginary part and the bar signifies conjugation. Thus, the two residue matrices associated to these poles are complex conjugates too: $\mathbf{R} = \mathbf{R}_R + j\mathbf{R}_I$ and $\bar{\mathbf{R}} = \mathbf{R}_R - j\mathbf{R}_I$. The contribution of these complex poles to the output equation, either (3.31) or (3.35), is:

$$\mathbf{I}_x = \mathbf{X}_1 + \mathbf{X}_2 \quad (5.1)$$

with

$$\mathbf{X}_1 = \frac{\mathbf{R}\mathbf{U}}{s - p} \quad (5.2)$$

and

$$\mathbf{X}_2 = \frac{\bar{\mathbf{R}}\mathbf{U}}{s - \bar{p}}, \quad (5.3)$$

where \mathbf{U} is the input vector; that is, $\mathbf{U} = \mathbf{V}_0$ for (3.32) and $\mathbf{U} = \mathbf{I}_{fw,L} \exp(s - \tau_k)$ for (3.36).

Application of the Inverse Laplace Transform to (5.1)-(5.3) yields:

$$\mathbf{i}_x = \mathbf{x}_1 + \mathbf{x}_2 \quad (5.4)$$

$$\frac{d}{dt} \mathbf{x}_1 = p\mathbf{x}_1 + \mathbf{R}\mathbf{u} \quad (5.5)$$

$$\frac{d}{dt} \mathbf{x}_2 = \bar{p}\mathbf{x}_2 + \bar{\mathbf{R}}\mathbf{u}. \quad (5.6)$$

Consideration is now made as to the fact that state vectors \mathbf{x}_1 and \mathbf{x}_2 must be conjugates:

$$\mathbf{x}_1 = \mathbf{x}_R + j\mathbf{x}_I \quad (5.7)$$

$$\mathbf{x}_2 = \mathbf{x}_R - j\mathbf{x}_I. \quad (5.8)$$

By introducing (5.7) and (5.8) in (5.4) the following expression is drawn

$$\mathbf{i}_x = 2\mathbf{x}_R. \quad (5.9)$$

The introduction of (5.7) in (5.5) and the subsequent separation of real and imaginary terms results in the following pair of coupled differential equations:

$$\frac{d}{dt} \mathbf{x}_R = p_R \mathbf{x}_R - p_I \mathbf{x}_I + \mathbf{R}_R \mathbf{u} \quad (5.10)$$

$$\frac{d}{dt} \mathbf{x}_I = p_R \mathbf{x}_I + p_I \mathbf{x}_R + \mathbf{R}_I \mathbf{u} \quad (5.11)$$

Further application of (5.8) in (5.6) results again in (5.10) and (5.11). It is thus clear that (5.7) is redundant with (5.8) and that (5.9)-(5.11) are sufficient to determine the output \mathbf{i}_x as in

(5.4). In addition to this, state vectors \mathbf{x}_R and \mathbf{x}_I are real.

The discrete state-space (SS) forms are obtained applying the trapezoidal rule of differentiation to (5.9)-(5.11). After an algebraic process the following expressions are obtained:

$$\mathbf{i}_x = 2\mathbf{x}_R \quad (5.12)$$

$$\mathbf{x}_R = \delta \mathbf{x}'_R - \varepsilon \mathbf{x}'_I + \boldsymbol{\Theta}(u + u') \quad (5.13)$$

$$\mathbf{x}_I = \delta \mathbf{x}'_I + \varepsilon \mathbf{x}'_R + \mathbf{E}(u + u') \quad (5.14)$$

where variables $\delta, \varepsilon, \boldsymbol{\Theta}$ and \mathbf{E} are as follows:

$$\delta = 1 + \frac{4\Delta t p_R - 2\Delta t^2(p_R^2 + p_I^2)}{4 - 4\Delta t p_R + \Delta t^2(p_R^2 + p_I^2)},$$

$$\varepsilon = \frac{4\Delta t p_I}{4 - 4\Delta t p_R + \Delta t^2(p_R^2 + p_I^2)},$$

$$\boldsymbol{\Theta} = \frac{(2\Delta t - \Delta t^2 p_R)\mathbf{R}_R - \Delta t^2 p_I \mathbf{R}_I}{4 - 4\Delta t p_R + \Delta t^2(p_R^2 + p_I^2)},$$

and

$$\mathbf{E} = \frac{\Delta t^2 p_I \mathbf{R}_R + (2\Delta t - \Delta t^2 p_R)\mathbf{R}_I}{4 - 4\Delta t p_R + \Delta t^2(p_R^2 + p_I^2)}$$

For the case of complex poles in \mathbf{H} , (5.12)-(5.14) are in proper discrete SS forms to evaluate \mathbf{i}_x , since the input u at the right-hand side of (5.13) and (5.14) is the already determined historic value $\mathbf{i}_{fw,L}(t - \tau_k)$. On the basis of this last result, (3.37) can be modified as follows to calculate $\mathbf{i}_{h-aux,0}$ in real arithmetic with first order blocks:

$$\mathbf{i}_{h-aux,0} = \sum_{k=1}^{Ng} \left(\sum_{i=1}^{Nhr(k)} \mathbf{x}_{k,i} + \sum_{i=1}^{Nhc(k)/2} 2\mathbf{x}_{R-k,i} \right) \quad (5.15)$$

where $Nhr(k)$ and $Nhc(k)$ are, respectively, the number of real and of complex poles at the k th delay group. Note that (5.12)-(5.14) have to be modified adding sub-indexes k and i to include more than one pair of complex poles that could arise in the evaluation of $\mathbf{i}_{h-aux,0}$.

To calculate $\mathbf{i}_{sh,0}$, as complex poles arise at the fitting of \mathbf{Y}_c , (5.12)-(5.14) are not in proper discrete SS forms since input \mathbf{u} , at their right-hand sides corresponds to present-time value \mathbf{v}_0 . Thus, a change of variable is introduced. This helps not only to avoid the nonproper discrete SS forms, but also to improve the numerical efficiency of the line model. State variables are thus redefined as follows:

$$\mathbf{y}_R = \mathbf{x}_R - \boldsymbol{\Theta}\mathbf{u} \quad (5.16)$$

$$\mathbf{y}_I = \mathbf{x}_I - \mathbf{E}\mathbf{u}. \quad (5.17)$$

The introduction of (5.16) and (5.17) in (5.12)-(5.14) yields the following discrete SS forms:

$$\mathbf{i}_x = 2\mathbf{y}_R + 2\boldsymbol{\Theta}\mathbf{u} \quad (5.18)$$

$$\mathbf{y}_R = \delta\mathbf{y}'_I - \varepsilon\mathbf{y}'_I + \boldsymbol{\Psi}\mathbf{u}' \quad (5.19)$$

$$\mathbf{y}_I = \delta\mathbf{y}'_I + \varepsilon\mathbf{y}'_R + \boldsymbol{\Xi}\mathbf{u}' \quad (5.20)$$

where variables $\boldsymbol{\Psi}$ and $\boldsymbol{\Xi}$ are as follows:

$$\boldsymbol{\Psi} = (\delta + \mathbf{I})\boldsymbol{\Theta} - \varepsilon\mathbf{E}$$

$$\boldsymbol{\Xi} = (\delta + \mathbf{I})\mathbf{E} + \varepsilon\boldsymbol{\Theta}.$$

On the basis of (5.18)-(5.20), (3.43) is modified as follows for the calculation of $\mathbf{i}_{sh,0}$

$$\mathbf{i}_{sh,0} = \mathbf{G}_y \mathbf{v}_0 + \sum_{i=1}^{N_{yr}} \mathbf{y}_i + 2 \sum_{i=1}^{N_{yc}/2} \mathbf{y}_{R-i} \quad (5.21)$$

with

$$\mathbf{G}_y = \mathbf{G}_0 + \sum_{i=1}^{N_{yr}} \boldsymbol{\beta}_i + 2 \sum_{i=1}^{N_{yc}/2} \boldsymbol{\theta}_i \quad (5.22)$$

where N_{yr} and N_{yc} are the respective numbers of real and complex poles in the rational approximation of \mathbf{Y}_c .

If (5.16) and (5.17) are further introduced in (5.15) the latter can be expressed as

$$\mathbf{i}_{h-aux,0} = \sum_{k=1}^{N_g} \mathbf{G}_{h-k} \mathbf{i}_{fw,0}(t - \tau_k) + \sum_{k=1}^{N_g} \sum_{i=1}^{Nh(k)/2} \mathbf{y}_{k,i} + 2 \sum_{k=1}^{N_g} \sum_{i=1}^{Nh(k)/2} \mathbf{y}_{R-k,i} \quad (5.23)$$

where

$$\mathbf{G}_{h-k} = \sum_{i=1}^{Nh(k)/2} \boldsymbol{\beta}_{k,i} + 2 \sum_{i=1}^{Nh(k)/2} \boldsymbol{\theta}_{k,i} \quad (5.24)$$

Expressions (5.18)-(5.24), allow to calculate (3.28) using real arithmetic only with first order realizations.

5.2 Second Order Realizations

Another possibility to implement the WB model, using real arithmetic only, is the second order block or second order realization technique which is based on the fact that the imaginary parts of complex conjugate poles are naturally eliminated when these are combined into a single second order state. In order to develop the second-order block-technique, consider again two poles: this time, however, these poles can be complex conjugates or any two real ones. Let these be p_1 and p_2 . Their associated residue matrices are \mathbf{R}_1 and \mathbf{R}_2 . The contribution of these poles to the output equation, either (3.31) or (3.35), is:

$$\mathbf{I}_x = \mathbf{X}_1 + \mathbf{X}_2 = \mathbf{X} \quad (5.25)$$

where

$$\mathbf{X}_1 = \frac{\mathbf{R}_1 \mathbf{U}}{s - p_1} \quad (5.26)$$

and

$$\mathbf{X}_2 = \frac{\mathbf{R}_2 \mathbf{U}}{s - p_2} . \quad (5.27)$$

By adding \mathbf{X}_1 and \mathbf{X}_2 , a second-order real-state \mathbf{X} is obtained since imaginary parts are naturally eliminated

$$\mathbf{X} = \frac{(\mathbf{a}_1 s + \mathbf{a}_0)}{(s^2 + b_1 s + b_0)} \mathbf{U}. \quad (5.28)$$

Real variables $\mathbf{a}_1, \mathbf{a}_0, b_1$ and b_0 are as follows:

$$\mathbf{a}_1 = \mathbf{R}_1 + \mathbf{R}_2,$$

$$\mathbf{a}_0 = -\mathbf{R}_1 p_2 - \mathbf{R}_2 p_1,$$

$$b_1 = -p_1 - p_2,$$

and

$$b_0 = p_1 p_2.$$

Application of the Inverse Laplace Transform to (5.25) and (5.28) yields:

$$\mathbf{i}_x = \mathbf{x} \quad (5.29)$$

and

$$\frac{d^2}{dt^2} \mathbf{x} + b_1 \frac{d}{dt} \mathbf{x} + b_0 \mathbf{x} = \mathbf{a}_1 \frac{d}{dt} \mathbf{u} + \mathbf{a}_0 \mathbf{u} . \quad (5.30)$$

The discrete SS forms for the second-order block-model are obtained applying the trapezoidal rule of differentiation to (5.29) and (5.30), which after an algebraic process become

$$\mathbf{i}_x = \mathbf{x} \quad (5.31)$$

$$\mathbf{x} = -\eta \mathbf{x}' - \iota \mathbf{x}'' + \Phi \mathbf{u} + \mathbf{K} \mathbf{u}' + \mathbf{N} \mathbf{u}'' \quad (5.32)$$

where $\mathbf{x}'' = \mathbf{x}(t - 2\Delta t)$ and $\eta, \iota, \Phi, \mathbf{K}, \mathbf{N}$ are as follows:

$$\eta = \frac{B}{A}, \quad \iota = \frac{C}{A}, \quad \Phi = \frac{D}{A}, \quad \mathbf{K} = \frac{E}{A}, \quad \mathbf{N} = \frac{F}{A},$$

with

$$A = \frac{1}{\Delta t^2} + \frac{b_1}{2\Delta t} + \frac{b_0}{4},$$

$$B = \frac{b_0}{2} - \frac{2}{\Delta t^2},$$

$$C = \frac{1}{\Delta t^2} - \frac{b_1}{2\Delta t} + \frac{b_0}{4},$$

$$D = \frac{a_1}{2\Delta t} + \frac{a_0}{4},$$

$$E = \frac{a_0}{2}$$

$$F = \frac{a_0}{4} - \frac{a_1}{2\Delta t}.$$

Notice in (5.32) that two history terms are needed. For the case of poles in \mathbf{H} , (5.31) and (5.32) are in proper discrete SS form to evaluate \mathbf{i}_x . Thus, (3.37) can be modified as follows for calculating $\mathbf{i}_{h-aux,0}$ in real arithmetic with second order blocks:

$$\mathbf{i}_{h-aux,0} = \sum_{k=1}^{N_g} \sum_{i=1}^{Nh(k)/2} \mathbf{x}_{k,i} . \quad (5.33)$$

Notice that the number of terms Nh in each propagation group has dropped to half.

If a change of variable is needed the implied state variable can be redefined as follows:

$$\mathbf{y} = \mathbf{x} - \Phi \mathbf{u} . \quad (5.34)$$

The introduction of (5.34) in (5.31) and (5.32) yields the following discrete SS forms:

$$\mathbf{i}_x = \mathbf{y} + \Phi \mathbf{u} . \quad (5.35)$$

and

$$\mathbf{y} = -\eta \mathbf{y}' - \iota \mathbf{y}'' + \Lambda \mathbf{u}' + \mathbf{M} \mathbf{u}'' . \quad (5.36)$$

Variables Λ and \mathbf{M} are as follows:

$$\Lambda = \mathbf{K} - \eta \Phi$$

$$\mathbf{M} = \mathbf{N} - \iota \Phi$$

Expression (3.40) can now be modified as follows to calculate $\mathbf{i}_{sh,0}$ with second order blocks

$$\mathbf{i}_{sh,0} = \mathbf{G}_y \mathbf{v}_0 + \sum_{i=1}^{N_y/2} \mathbf{y}_i \quad (5.37)$$

With

$$\mathbf{G}_y = \mathbf{G}_0 + \sum_{i=1}^{N_y/2} \Phi_i . \quad (5.38)$$

If (5.34) is further introduced in (5.33) the latter can be expressed as

$$\mathbf{i}_{h-aux,0} = \sum_{k=1}^{N_g} \mathbf{G}_{h-k} \mathbf{i}_{fw,0}(t - \tau_k) + \sum_{k=1}^{N_g} \sum_{i=1}^{Nh(k)/2} \mathbf{y}_{k,i} . \quad (5.39)$$

where

$$\mathbf{G}_{h-k} = \sum_{i=1}^{Nh(k)/2} \boldsymbol{\Phi}_{k,i} . \quad (5.40)$$

This technique may give the impression of being capable of handle even number of poles only: nevertheless, it can manage odd numbers of poles as well by considering the single pole left as a second order block by taking \mathbf{a}_0 and \mathbf{b}_0 as in (5.28) equal to 0.

5.3 Higher Order Realizations

The general idea of second order blocks can be further extended to any degree-order greater than 2. Thus, third, fourth and higher order blocks can be synthesized in addition to the previous ones of first and second order. This section describes the development of M -order block WB models with $M > 2$.

Considering the contribution to (3.31) or (3.35) of M poles:

$$\mathbf{I}_x = \mathbf{X}_1 + \mathbf{X}_2 + \dots + \mathbf{X}_M = \mathbf{X} \quad (5.41)$$

the following expression is obtained as contributions are added into a single M th order state

$$\mathbf{X} = \frac{\sum_{i=0}^{M-1} \mathbf{a}_i s^i}{s^M + \sum_{i=0}^{M-1} b_i s^i} \mathbf{U} , \quad (5.42)$$

where variables \mathbf{a}_i and \mathbf{b}_i are obtained by conventional arithmetic in (5.41). Application of the Inverse Laplace Transform to (5.41) and (5.42) yields:

$$\mathbf{i}_x = \mathbf{x} , \quad (5.43)$$

and

$$\frac{d^M}{dt^M} \mathbf{x} + \sum_{i=0}^{M-1} b_i \frac{d^i}{dt^i} \mathbf{x} = \sum_{i=0}^{M-1} a_i \frac{d^i}{dt^i} \mathbf{u}, \quad (5.44)$$

The discrete SS forms corresponding to (5.44) are obtained applying the trapezoidal rule of differentiation to (5.43) and (5.44). Where the number of history terms is given by M .

$$\mathbf{i}_x = \mathbf{x} \quad (5.45)$$

$$\mathbf{x} = -\sum_{k=1}^M \alpha_k \mathbf{x}^k + \beta_0 \mathbf{u} + \sum_{k=1}^M \beta_k \mathbf{u}^k, \quad (5.46)$$

where the variables α and β are obtained when the trapezoidal rule is applied to (5.44).

For the case of poles in \mathbf{H} , (5.43) and (5.44) yield proper discrete SS forms to evaluate \mathbf{i}_x . Thus, (3.37) can be modified as follows for calculating $\mathbf{i}_{h-aux,0}$ in real arithmetic:

$$\mathbf{i}_{h-aux,0} = \sum_{k=1}^{Ng} \sum_{i=1}^{Nh(k)/M} \mathbf{x}_{k,i}. \quad (5.47)$$

In order to gain computational speed, state vector \mathbf{x} can be redefined as:

$$\mathbf{y} = \mathbf{x} - \beta_0 \mathbf{u}. \quad (5.48)$$

The introduction of (5.48) in (5.45) and (5.46) yields the following discrete SS forms:

$$\mathbf{i}_x = \mathbf{y} + \beta_0 \mathbf{u} \quad (5.49)$$

and

$$\mathbf{y} = -\sum_{k=1}^M \alpha_k \mathbf{x}^k + \sum_{k=1}^M \boldsymbol{\Xi}_k \mathbf{u}^k. \quad (5.50)$$

where $\boldsymbol{\Xi}_k = \beta_k - \alpha_k \beta_0$. Expression (3.40) can be modified as follows to calculate $\mathbf{i}_{sh,0}$

$$\mathbf{i}_{sh,0} = \mathbf{G}_y \mathbf{v}_0 + \sum_{i=1}^{N_y/M} \mathbf{y}_i \quad (5.51)$$

With

$$\mathbf{G}_y = \mathbf{G}_0 + \sum_{i=1}^{N_y/M} \boldsymbol{\beta}_{0-i}. \quad (5.52)$$

The introduction of (5.48) in (5.47) results in the following discrete SS form for the output equation:

$$\mathbf{i}_{h-aux,0} = \sum_{k=1}^{Ng} \mathbf{G}_{h-k} \mathbf{i}_{fw,0}(t - \tau_k) + \sum_{k=1}^{Ng} \sum_{i=1}^{Nh(k)/M} \mathbf{y}_{k,i}. \quad (5.53)$$

where

$$\mathbf{G}_{h-k} = \sum_{i=1}^{Nh(k)/M} \boldsymbol{\beta}_{0-k,i}. \quad (5.54)$$

Expressions (5.46), (5.47), (5.50)-(5.54) can be considered as a general representation for the WB model being realized with blocks of any order. In fact, by making $M=1$ at the above equations, the resulting expressions correspond to those given at section 3.5 for the ULM.

5.4 Application Examples

Three test cases are presented here to assess both the accuracy and the numerical efficiency of the previously proposed model-realizations. The first case involves an aerial line. The second case involves a 2-phase (dc) underground cable. For the third case, the previous two-cable system is converted into a three-cable one. The first two examples were chosen for convenience, since the first one only includes real poles and the second includes a mix of real and complex poles. The third case is applied in the testing stability and accuracy of the second-order block-model as the selected integration time-step is below 1 μ s.

5.4.1 Example 1: aerial line

This case consists of a 3-phase, 193 km long aerial line. Two propagation or delay groups are formed. For this case 8 real poles have been obtained at the fitting of the \mathbf{H} matrix: that is, 4 poles correspond to each propagation group. A total of 8 real poles were needed as well for the fitting of \mathbf{Y}_c .

Figure 5-1 shows the transversal configuration of the line which was provided by Professor Jean Mahseredjian, Figure 5-2 shows the test configuration, where the far-end of the line is almost open through its connection to high-valued resistance. At the sending-end the three phases are energized simultaneously. The simulation was carried out with a $1\mu\text{s}$ time step. The source is 169kV, RL2 is determined by its zero and positive sequence data in Ohms: $R_0=2$, $R_1=1$, $X_0=22$, $X_1=15$.

Figure 5-3 shows the voltage waveforms at the far-end as obtained with EMTP-RV, as well as with the previously proposed first, second and fourth order block-models. The differences among the simulation methods are not distinguishable by eye. Nevertheless, Figure 5-4 shows the relative errors by groups of three phases between each one of the proposed methodologies and the results obtained with EMTP-RV. Figure 5-5 provides the waveforms of current at the receiving end of the line as obtained with EMTP-RV, and with the three proposed methodologies. Figure 5-6 shows the relative errors between EMTP-RV and each one of the three proposed techniques.

For this test case, the largest relative difference between EMTP-RV and the first-order block-model is just above 10^{-15} . In the case of the second-order block-realization the relative difference is under 10^{-11} . Finally, for the fourth-order block-realization the relative difference is under 10^{-3} .

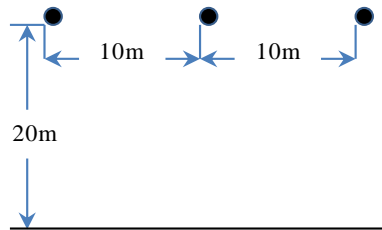


Figure 5-1 : RTWB 3-phase aerial line configuration.

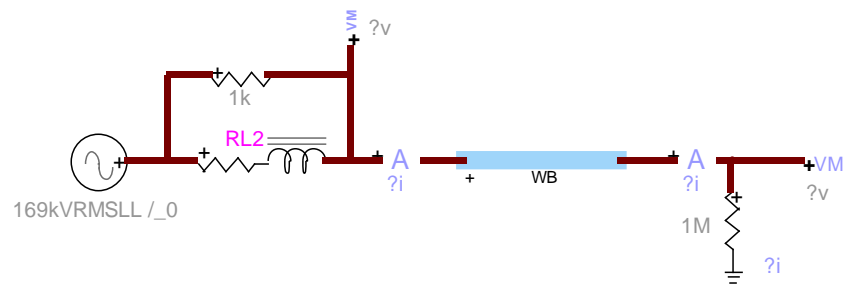


Figure 5-2 : RTWB 3-phase aerial line test circuit.

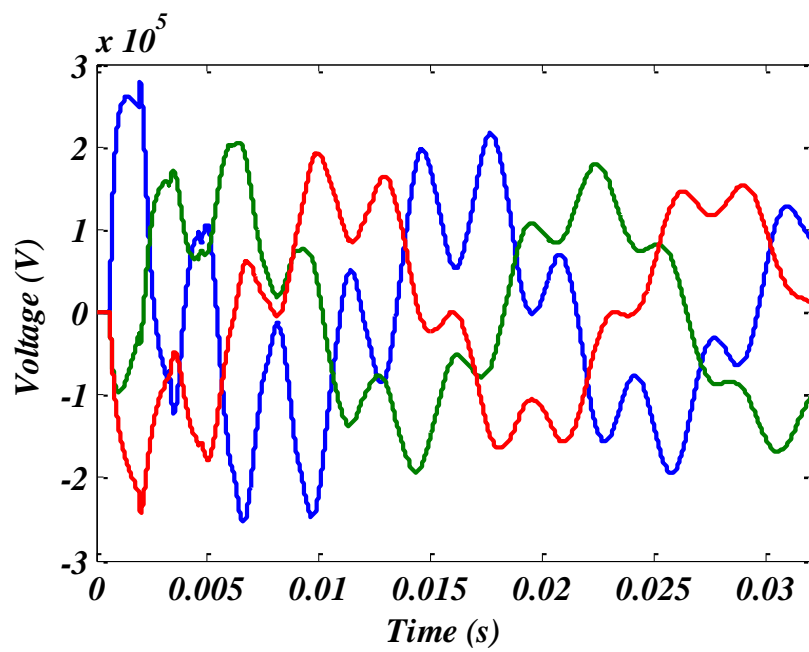


Figure 5-3 : RTWB 3-phase aerial line receiving end voltage waveforms.

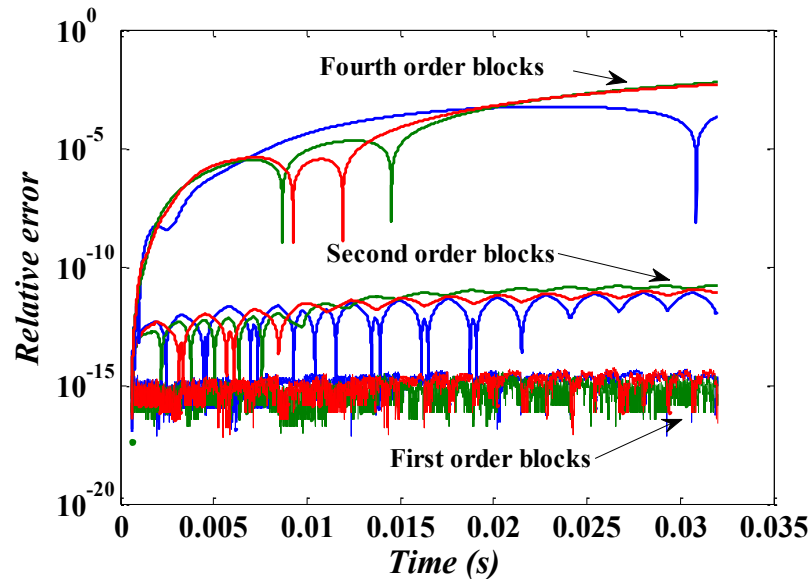


Figure 5-4 : RTWB 3-phase aerial line receiving end voltage relative errors.

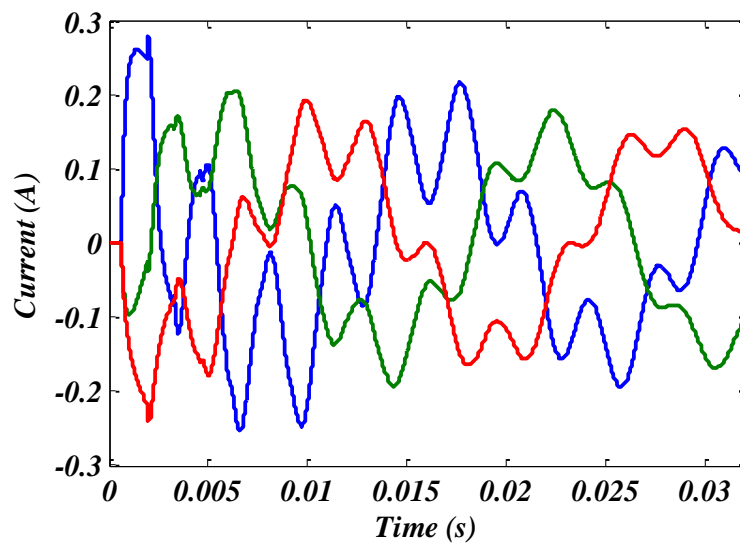


Figure 5-5 : RTWB 3-phase aerial line receiving end current waveforms.

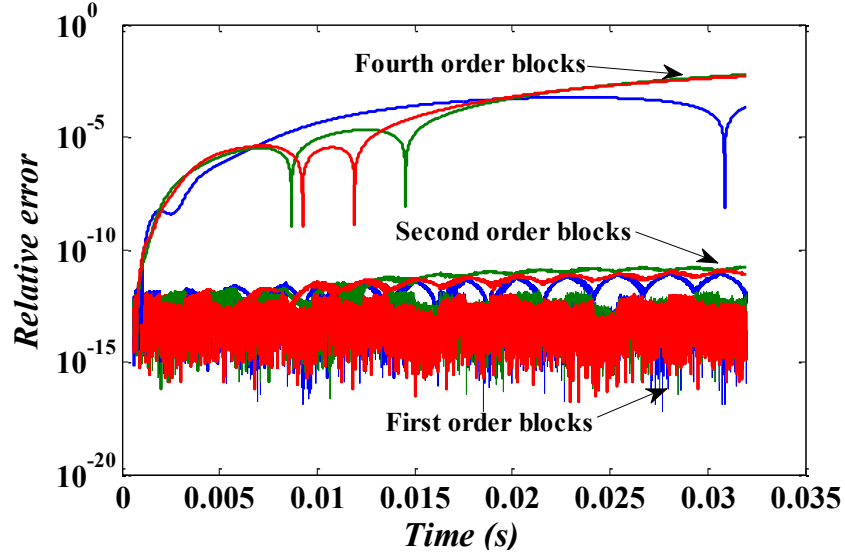


Figure 5-6 : RTWB 3-phase aerial line receiving end current relative errors.

5.4.2 Example 2: underground cable

Figure 5-7 provides the transversal layout of a 2-phase underground cable. Note that this case is a modified version of the underground cable at section 3.6.1. For this case three delay groups have been formed and 28 poles in total were needed for the fitting of the \mathbf{H} matrix. Six real poles and zero complex poles correspond to the first propagation group, 12 real poles and 4 complex poles correspond to the second group and 4 real poles and 2 complex poles are for the third group. Finally 10 real poles were used in the fitting of \mathbf{Y}_c .

Figure 5-8 shows the test configuration where the far-ends of the cores are left open and their sending-ends are energized simultaneously, cable sheaths are grounded at both ends through 1 Ohm resistances. The simulation was carried out with a $1\mu\text{s}$ time step. Cable and source data are as in section 3.6.1. Recall that cable length is 15 km.

Figure 5-9 shows the voltage waveforms at the far-end of the cable as obtained with EMTP-RV, as well as with the first, second and fourth order block-models proposed here. The differences among these simulation methods are not distinguishable at this figure. Figure 5-10, nevertheless, shows the relative differences by groups of four phases between EMTP-RV and each one of the proposed models. Figure 5-11 shows waveforms of currents as obtained with EMTP-RV, and with each one of the proposed models. The waveforms are measured at the receiving end of the cable. Figure 5-12 shows the corresponding relative differences.

Note from Figure 5-10 and Figure 5-12 that the highest relative difference between EMTP-RV and the first-order block-model is under 10^{-14} . In the case of the second-order block-model this difference is under 10^{-9} , whereas for fourth order blocks the maximum error is under 10^1 .

From the above results it can be observed that as the order of the realization blocks increases the accuracy goes down. It can be observed also that first and second order blocks present high accuracy, while the one of the fourth order block starts deteriorating very quickly. The loss of accuracy at the higher order blocks is caused by the finite precision (quantization) of the model parameters and variables [51].

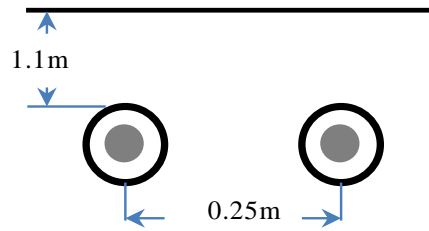


Figure 5-7 : RTWB 2-phase underground cable layout.

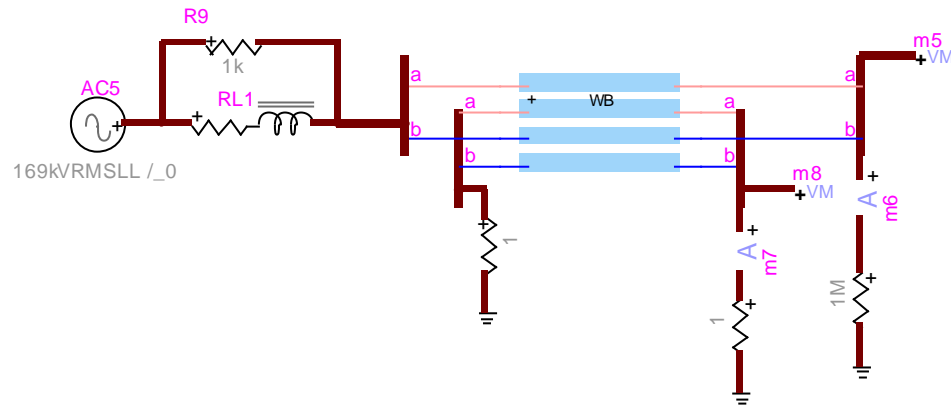


Figure 5-8 : RTWB 2-phase underground cable test circuit.

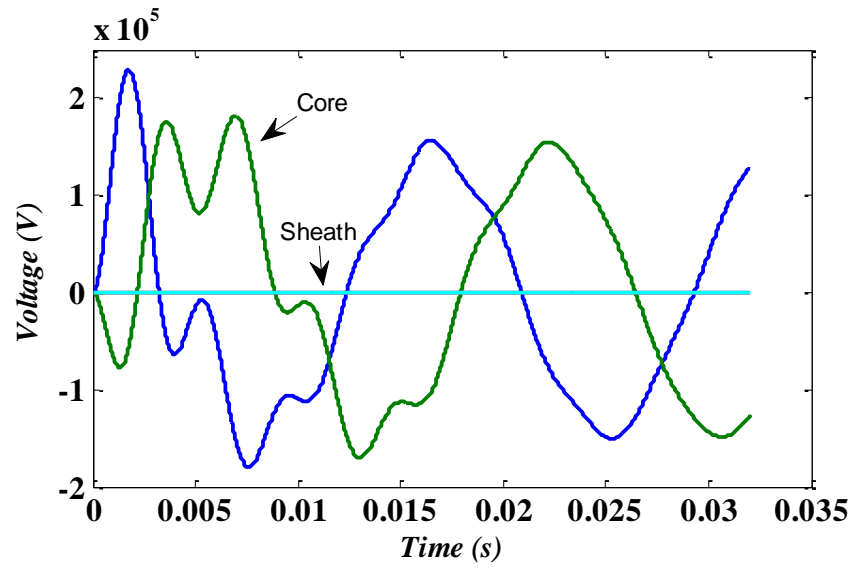


Figure 5-9 : RTWB 2-phase underground cable receiving-end voltage waveforms.

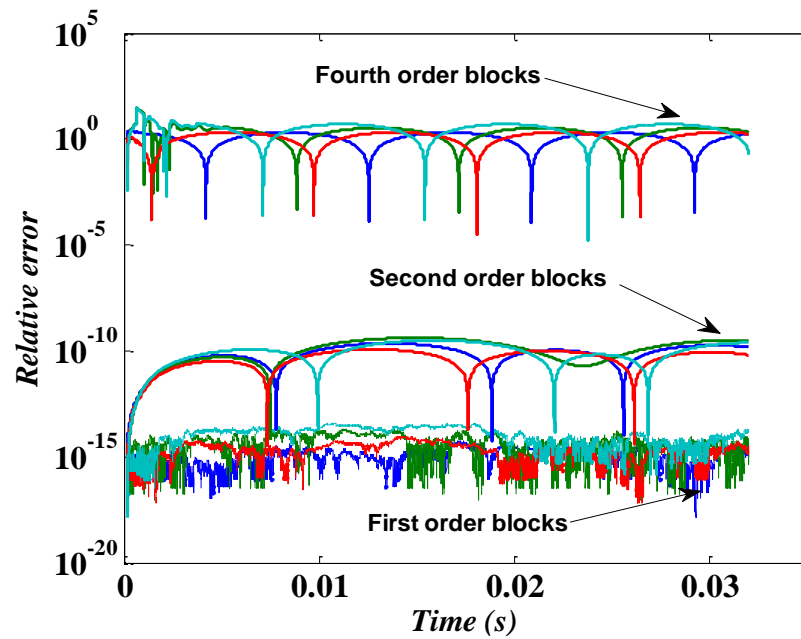


Figure 5-10 : RTWB 2-phase underground cable receiving-end voltage relative differences.

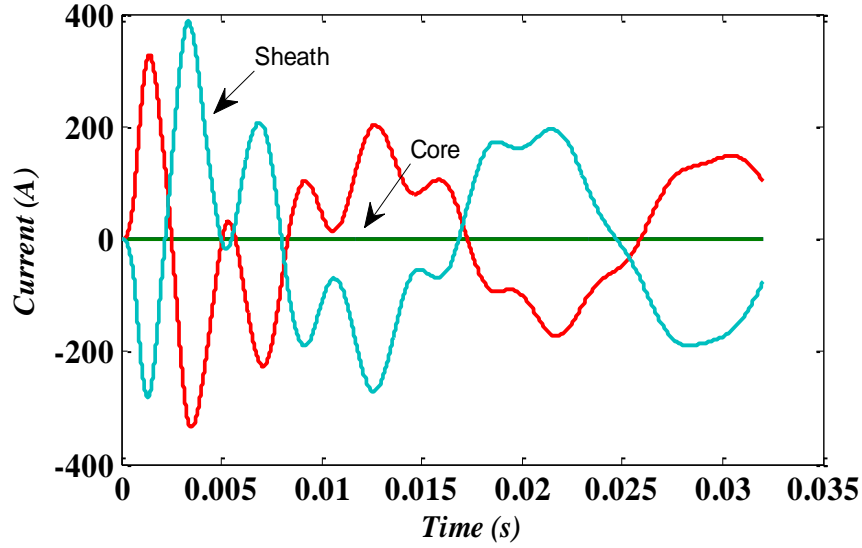


Figure 5-11 : RTWB 2-phase underground cable receiving-end current waveforms.

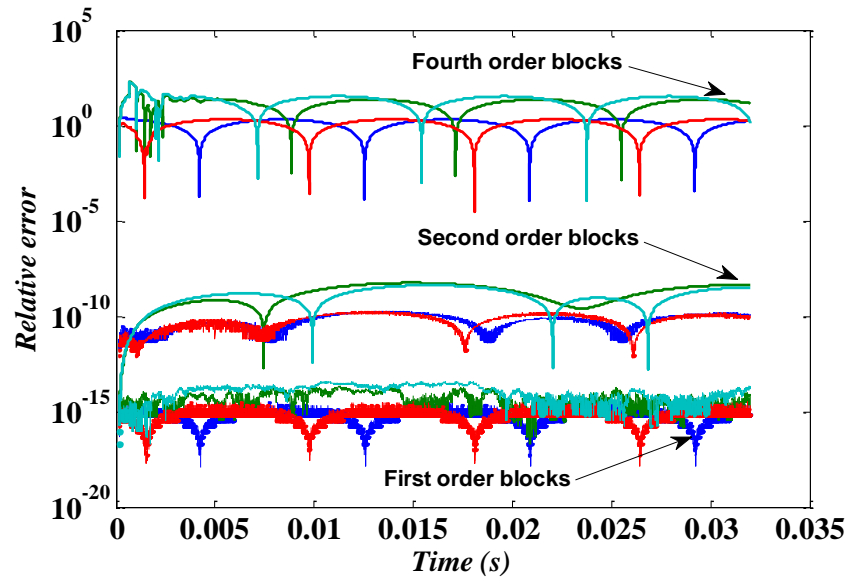


Figure 5-12 : RTWB 2-phase underground cable receiving-end current relative differences.

5.4.3 Example 3: 3-phase underground cable

The study case involving a 3-phase underground cable-system at section 3.6.1 is used here to test the accuracy and convergence of the second-order block-model as it is used with very small time steps, up to $0.01\mu\text{s}$. The transversal layout of the 3-phase cable is as in Figure 3-3 and the connection diagram is as in Figure 3-4.

The simulation results for this test are presented in Figure 5-13 and Figure 5-14, where phase a is in blue, phase b is in green and phase c is in red color. Dashed lines are used for EMTP-RV waveforms, while solid lines are used for second-order block-model results. Figure 5-15 and Figure 5-16 show the relative differences between both results.

After an analysis of Figure 5-15 and Figure 5-16 it is noticed that the proposed second-order block-model renders good accuracy for such small simulation time step, since the maximum relative differences for core voltages is in the range of 10^{-6} , and the one for the sheath voltages is in the range of 10^{-5} . It is also noticed that the model is stable even after 2 million simulation points.

This simulation represents a very stringent test to the model. Given the nature of its discrete parameters and variables, a very small time step may produce large quantization errors.

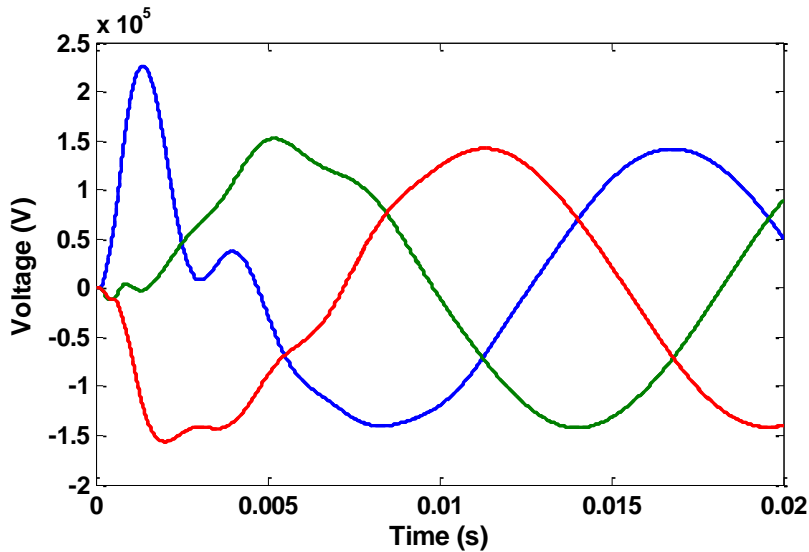


Figure 5-13: RTWB 3-phase cable-core receiving-end voltage waveforms.

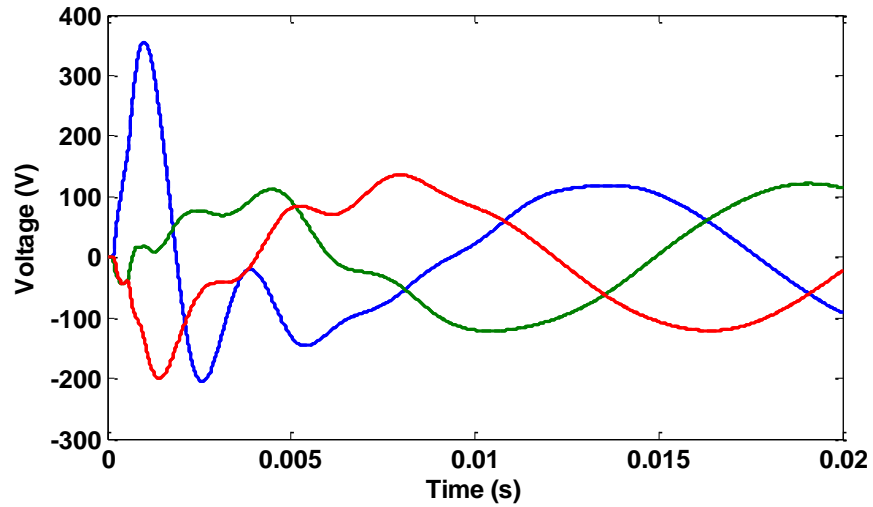


Figure 5-14: RTWB 3-phase cable-sheath receiving-end voltage waveforms.

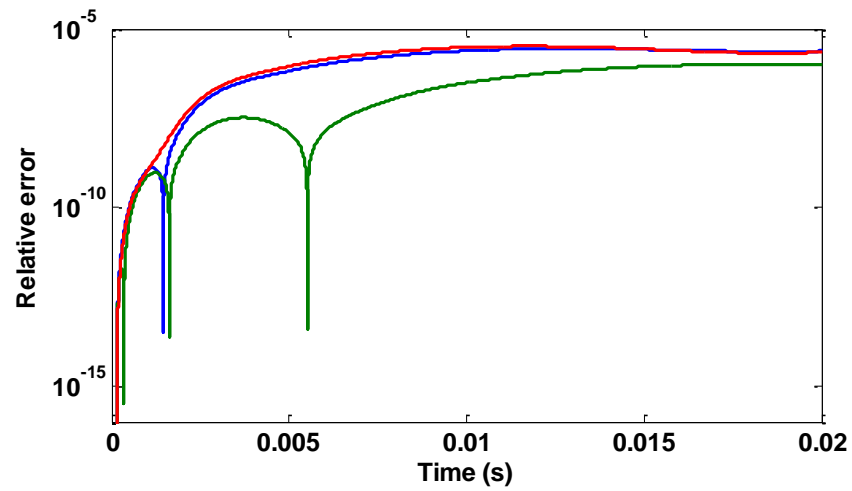


Figure 5-15: RTWB 3-phase cable-core relative differences.

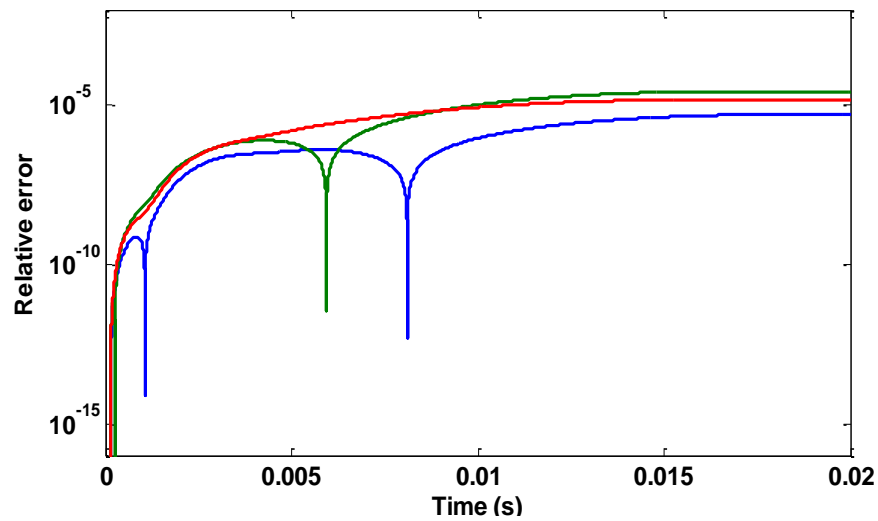


Figure 5-16: RTWB 3-phase cable-sheath relative differences.

5.4.4 Performance of proposed realizations

The model realizations proposed in this chapter have been implemented in Matlab, Fortran and in C language. Table 5.1 presents the performance of each implementation as obtained with the Fortran versions at tests in subsections 5.4.1 and 5.4.2. It's noticed from Table 5.1 that the first-order block-realization is 7.1 times faster than the conventional approach and that second-order block-realization is 8.3 times faster in the aerial line case. For the second case a 22% of \mathbf{H} poles are complex and, for this, first-order blocks are 5.5 times faster than the conventional approach, while second-order blocks are almost 6.3 times faster.

It may be thought that blocks of higher order than two should give a better computational performance. Nevertheless, a careful analysis of expressions (5.50), (5.53) and (5.54) shows that the number of operations reaches fast an almost constant value as the block order is increased. The advantage of the second-order block-realization lies on the fact that complex values are naturally eliminated with the grouping. Given their susceptibility to quantization errors, the use of block models of order higher than the second is unadvised.

Table 5.1 : Comparison of numerical performance

Method	Time to perform 14286 steps	
	Aerial line	Underground cable
Conventional	781 ms	2263 ms
First order blocks	110 ms	410 ms
Second Order blocks	94 ms	360 ms
Fourth Order blocks	94 ms	360 ms

5.5 Remarks

It has been shown in this chapter that the computational efficiency of the standard implementation of the WB line-model is increased substantially. Rational fit of matrices \mathbf{Y}_c and \mathbf{H} as obtained with VF, OVF or WVF may produce complex states and the standard treatment of these has been discarded here due to its computational inefficiency. Instead, it has been proposed here the handling of all internal state-variables by processes in real arithmetic. As conjugate pairs of complex states convey the same information; one out of these two states can be discarded while the other can be handled very efficiently by a pair of equivalent real states that are coupled.

Other alternatives proposed and analyzed here consist in the realizations of line models by means of second, fourth and higher order blocks of states. These blocks naturally eliminate complex states. Second-order block-realizations involve fewer computations than first-order blocks and than the standard WB implementation. As the order of the blocks is increased, the model becomes more sensitive to quantization errors at the digital representation of the model coefficients and internal variables.

The test included here have shown that first-order block-realizations with real arithmetic, as well as second-order block-realizations, are the most accurate and do not show detrimental error-accumulation symptoms, even after 2 million of simulated samples with an integration time-step of $0.01 \mu\text{s}$. Fourth and higher order realizations, on the other hand, do show error-accumulation rather soon.

CHAPTER 6 **REAL-TIME WIDE-BAND (RTWB) LINE MODEL**

Due to the growing complexity of electric power supplying systems, reliable simulators are needed to assess system performance under normal and abnormal operation conditions. Power system utilities and consulting companies each time more resort to real-time simulators to carry out tests on control and protection equipment to be connected to the power grid; for instance, HVDC interconnections, SVCs, STATCOMs and other FACT devices, as well as the each time more popular distributed-generation (DG) devices and the renewable energy sources (RES). Real-time simulators are also being used to study the behavior of electrical systems at the design stage and for post-mortem analysis. Transmission lines are a very important part of power supplying systems and are often difficult to simulate with the required accuracy. This chapter provides a description of the implementation of one of the line models proposed in Chapter 5, along with that of the real-time platform where this model was implemented.

6.1 Overview of Real-Time Platform

eMEGAsim is a fully-digital power systems real-time simulator capable of simulating electromagnetic transients with sub-microsecond time steps. It has been developed and is commercialized by OPAL-RT technologies [47]. It takes advantage of open high-performance distributed and parallel computer technologies. Its hardware system is based on new generation Intel or AMD multi-core processors. Today, it is thus one of the least expensive alternatives for doing real-time simulations of EMTs. In addition, eMEGAsim can combine FPGA-based models to obtain simulation time steps in the order of hundred nanoseconds [44]. eMEGAsim's I/O system includes several independent fast 2.5-microseconds 16-bit analog input and 1 μ s output converters directly controlled by an FPGA processor to achieve sample times as low as 10 μ s. Users can program FPGA processors using a SIMULINK-to-HDL code generator to implement fast signal processing or special interface functions [44].

OP5000 I/O modules and FPGA boards can be selected to meet specific application needs. I/O with specialized signal conditioning can be installed in the same HILBOX chassis as the processor board or in a remote compact chassis interconnected to the main computer by fast optical fiber interfaces to minimize cabling, reduce noise, and eliminate ground loop problems [44].

Commercial off-the-shelf (COTS) simulators never become obsolete since processors and motherboards can be upgraded by the manufacturer or by customers with the latest technologies as soon as new hardware is available in the marketplace. Systems based on COTS ensure maximum long-term support, maintenance, expandability and upgradeability. This means that COTS simulator performance continuously increases over time as processor performance increases [44].

eMEGAsim allows users to develop controller models with SIMULINK [45] and electrical circuit models with SimPowerSystem [46]. An EMTP-RV interface is available to facilitate circuit diagram capture and validation of large circuits. The resulting model can be simulated off-line using available variable-step and fixed step solvers in MATLAB-SIMULINK and with Opal-RT's ARTEMIS third- and fifth-order fixed-step solver, optimized for real-time parallel simulation of electrical systems. EMTP-RV is used to validate the simulations by comparing with results obtained in off-line mode [44].

Simulink has emerged as a worldwide standard for scientific computing and has been extended for use in real-time simulation. It is a powerful, graphical interfaced, modeling and simulation tool contained in Matlab, multifunctional software for mathematical processing and is fully integrated with Real-Time Workshop (RTW) code generator [44].

SimPowerSystem (SPS) is a Matlab/Simulink toolbox which provides multiple integrated models, all based on electromechanical and electromagnetic equations, for the simulation of power grids and machine drives [44]. With the combination of other Simulink mathematical and physical-domain toolboxes, it is possible to easily model any power system components interconnected with complex mechanical sub-systems and associated controls [44].

The major advantage of using an SPS/Simulink-based real-time simulator is that it enables the user to conduct complete model design and tests using hardware in the loop (HIL) simulation. The eMEGAsim simulator uses a set of software tools especially designed to optimize real-time performance of electrical systems and drive applications. It enhances the simulation performance of SPS/Simulink-based models using various techniques and tools [44].

The calculation tool used in eMEGAsim, ARTEMIS, enables real-time simulation of SPS models by pre-calculating system equations. It provides a set of special discrete solvers to improve numerical stability and optimize parallel simulation of complex network equations. Its

main solvers are based on L-stable approximations of the matrix exponential. L-stability is an extension of A-stability in which most numerical oscillations are naturally suppressed [44]. The calculation tool includes a library of essential decoupling elements for the cluster distribution of the system state-space equations. The decoupling is either: 1) naturally made with traveling-wave power line models with inherent delays as with the WB line model; 2) artificially added by stubline (a line with single time step propagation delay) selected to achieve the required accuracy and computational speed [44].

The processor used for the tests presented in this thesis is an Intel Xeon X5680 Westmere 3.33GHz 12MB L3 Cache LGA 1366 130W Six-Core Server Processor.

6.2 RTWB Using First Order Realizations with Real Arithmetic

The WB line model described at section 3.5 with the modifications described at section 5.1 is coded, first in Matlab M-code, Fortran and finally in C language. The C version is further implemented as an object in the RT-LAB platform [22] (eMEGAsim simulator). This is the parallel and real-time version for the Wide-Band line model (RTWB).

RTWB is programmed as a set of two sub-blocks, each one representing one line/cable end. Each sub-block can be executed in a different processor of PC-cluster-based hardware. The sub-blocks create natural-network decoupling due to propagation delay between the two ends of a transmission line or cable.

RTWB is a model with nodal structure, while the RT-LAB platform is based in the SimPowerSystem toolbox [46] and employs a state-space formulation. The interfacing of RTWB with RT-LAB is through the state-space nodal (SSN) solver [48]-[50] included in ARTEMIS [50]. With this approach, the nodal representation of the RTWB model can be directly and simultaneously interfaced with the network-state equations using an SSN V-type group [48]. It means that the Norton model of Figure 6-1 is directly mapped into the nodal equations of the corresponding nodal group.

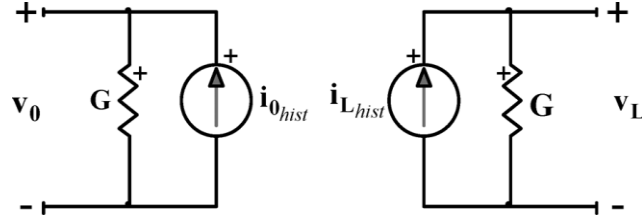


Figure 6-1: Discrete time-domain Norton equivalent of a multiconductor line.

The SSN method uses discretized state-space equations of clustered network elements. These equations are of the form

$$\dot{\mathbf{x}} = \mathbf{A}_k \mathbf{x} + \mathbf{B}_k \mathbf{u} \quad (6.1)$$

$$\mathbf{y} = \mathbf{C}_k \mathbf{x} + \mathbf{D}_k \mathbf{u}, \quad (6.2)$$

where bold characters are used to denote vectors and matrices. The column vectors \mathbf{x} and \mathbf{u} are the state variable and the input vectors, respectively. The state variables are capacitor voltages and inductor currents. These are independent and derived from the proper tree of the network to be simulated. The column vector \mathbf{y} is the vector of outputs. The state-space matrices $\mathbf{A}_k, \mathbf{B}_k, \mathbf{C}_k$ and \mathbf{D}_k correspond to the k th permutation of switches and piecewise linear device segments [48]-[50].

The discretization of state equations in (6.1) results in [48],[49]

$$\mathbf{x}_t = \hat{\mathbf{A}}_k \mathbf{x}'_t + \hat{\mathbf{B}}_k (\mathbf{u}' + \mathbf{u}) \quad (6.3)$$

where the hatted matrices result from the discretization process and primed variables represent their values delayed one time-step. Then, expressions (6.2) and (6.3) are re-written as follows [48],[49]:

$$\mathbf{x}_t = \hat{\mathbf{A}}_k \mathbf{x}'_t + \hat{\mathbf{B}}_k \mathbf{u}' + [\hat{\mathbf{B}}_{ki} \quad \hat{\mathbf{B}}_{kn}] \begin{bmatrix} \mathbf{u}_i \\ \mathbf{u}_n \end{bmatrix} \quad (6.4)$$

$$\begin{bmatrix} \mathbf{y}_i \\ \mathbf{y}_n \end{bmatrix} = \begin{bmatrix} \mathbf{C}_{ki} \\ \mathbf{C}_{kn} \end{bmatrix} \mathbf{x}_t + \begin{bmatrix} \mathbf{D}_{kii} & \mathbf{D}_{kin} \\ \mathbf{D}_{kni} & \mathbf{D}_{knn} \end{bmatrix} \begin{bmatrix} \mathbf{u}_i \\ \mathbf{u}_n \end{bmatrix}. \quad (6.5)$$

Subscript i refers to internal sources (injections) and subscript n refers to external nodal injections. The combination of the lower row of (6.5) with (6.4) gives [48],[49]

$$\mathbf{y}_n = \mathbf{W}_{kn} \mathbf{u}_n + \mathbf{y}_{khist} \quad (6.6)$$

where subscript $hist$ is used to denote past values known from the solution of equation (6.6) and

$$\mathbf{W}_{kn} = \mathbf{C}_{kn} \hat{\mathbf{B}}_{kn} + \mathbf{D}_{knn}. \quad (6.7)$$

Two different interpretations are possible for (6.7). When \mathbf{y}_n represents current injections (entering a group) and \mathbf{u}_n is for node voltages, \mathbf{y}_{khist} represents history current sources (\mathbf{i}_{khist}) and \mathbf{W}_{kn} is an admittance matrix. Expressions (6.6) and (6.7) are thus called a V-type SSN group and conform a Norton equivalent [48],[49]. If \mathbf{y}_n represents node voltages and \mathbf{u}_n holds currents entering a group, then \mathbf{y}_{khist} represents history voltage sources (\mathbf{v}_{khist}), and \mathbf{W}_{kn} is an impedance matrix. Expressions (6.6) and (6.7) are then referred to as an I-type SSN group and conform a Thevenin equivalent [48],[49]. The V-type group is the one used to interconnect the RTWB model with RT-LAB.

The interconnection is done by rewriting (3.28) as

$$\mathbf{i}_0 = \mathbf{G}_y \mathbf{v}_0 + \mathbf{i}_{hist,0} \quad (6.8)$$

where, (6.8) is equivalent to (6.6), $\mathbf{i}_{hist,0}$ is a history current which contains all the contributions from past states and is given by:

$$\mathbf{i}_{hist,0} = \mathbf{i}_{sh,0} - \mathbf{G}_y \mathbf{v}_0 - \mathbf{i}_{h-aux,0} \quad (6.9)$$

Figure 6-2 presents a flow diagram of RTWB, along with its interface with SSN. As it is mentioned before, RTWB is structured as two sub-blocks that can be simulate in parallel. The interrelations between the sub-blocks are shown in the figure and the dashed line indicates the model sub-division for the parallel execution of the line model. The steps followed by RTWB in a simulation are enlisted as follows for the line end at $x=0$. The process for the line end at

$x = L$ is analogous. Prior to the simulation, the conductance matrix \mathbf{G}_y of the line in question is evaluated and it is added to the corresponding sub-blocks of the conductance matrix that represents the entire network inside SSN. Then, initial values are assigned to history currents and to state variables inside RTWB.

Step I. SSN uses the history current, known either from initial conditions or from previous simulation steps, to determine network nodal voltages. v_0 and v_L are among these determined voltages and are given as the inputs to RTWB.

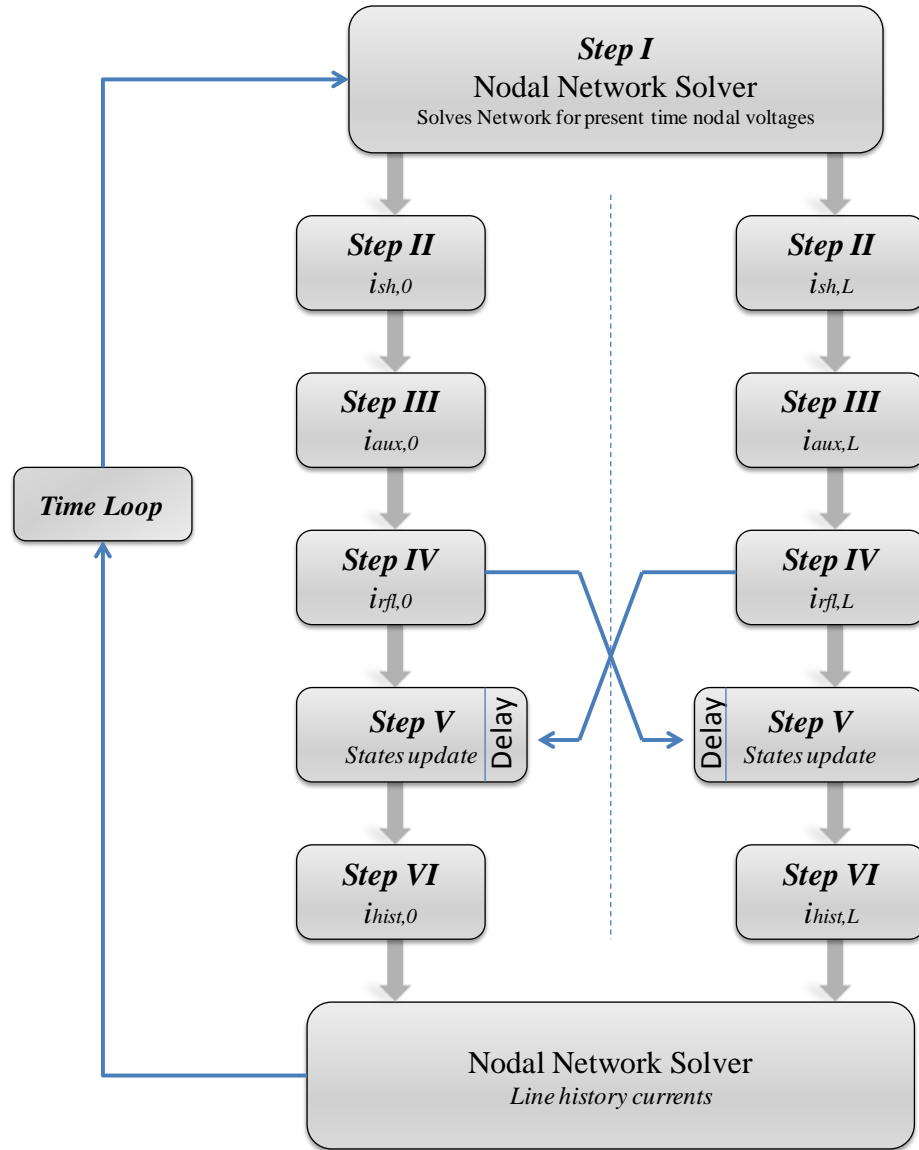


Figure 6-2 : Flow diagram for RTWB implementation and its interface with SSN.

Step II. Shunt current $i_{sh,0}$, due to the characteristic admittance of the line, is calculated by (5.21) which is repeated here for convenience:

$$i_{sh,0} = G_y v_0 + \sum_{i=1}^{N_{yr}} y_i + 2 \sum_{i=1}^{N_{yc}/2} y_{R-i}$$

Step III. Auxiliary current source value $i_{h-aux,0}$, due to the traveling waves from the remote line end, is updated by (5.15) also repeated as follows:

$$i_{h-aux,0} = \sum_{k=1}^{N_g} \left(\sum_{i=1}^{N_{hr}(k)} x_{k,i} + \sum_{i=1}^{N_{hc}(k)/2} 2x_{R-k,i} \right)$$

Step IV. Forward or local traveling wave currents are calculated by (3.27) in time domain for the terminal $x=0$, which after an algebraic process can be obtained by:

$$i_{fw,0} = 2i_{sh,0} - i_{h-aux,0}$$

These values are delivered to the other sub-block representing end $x=L$ and, branch currents i_0 are evaluated by (6.8) reproduced again as follows:

$$i_0 = G_y v_0 + i_{hist,0}$$

Step V. Internal states of the line model are updated.

Real states are updated by (3.42) and (3.47), both repeated as follows:

$$y_i = \alpha_i y'_i + \beta_i v'_0; \quad i = 1, 2, \dots, N_y$$

and

$$x_{k,i} = \alpha_{k,i} x'_{k,i} + \lambda_{k,i} [i_{fw,L}(t - \tau_k) + i'_{fw,L}(t - \tau_k)]; \quad \begin{matrix} k=1,2,\dots,N_g \\ i=1,2,\dots,Nh(k) \end{matrix}$$

Complex states are updated by the following expressions obtained as the respective modifications of (5.13), (5.14), (5.19), and (5.20). Subscript characters k and i are required for handling cases of more than one redundant complex pole in H and in Y_c :

$$x_{R-k,i} = \delta_{k,i} x'_{R-k,i} - \varepsilon_{k,i} x'_{I-k,i} + \Theta_{k,i} [i_{fw,L}(t - \tau_k) + i'_{fw,L}(t - \tau_k)]$$

$$x_{I-k,i} = \delta_{k,i} x'_{I-k,i} + \varepsilon_{k,i} x'_{R-k,i} + E_{k,i} [i_{fw,L}(t - \tau_k) + i'_{fw,L}(t - \tau_k)]$$

$$\mathbf{y}_{R-i} = \delta_i \mathbf{y}'_{R-i} - \varepsilon_i \mathbf{y}'_{I-i} + \boldsymbol{\Psi}_i \mathbf{v}'_0$$

$$\mathbf{y}_{I-i} = \delta_i \mathbf{y}'_{I-i} + \varepsilon_i \mathbf{y}'_{R-i} + \boldsymbol{\Xi}_i \mathbf{v}'_0$$

Step VI. History current contribution to the network representation from line end at $x=0$ is updated by (6.9):

$$\mathbf{i}_{hist,0} = \mathbf{i}_{sh,0} - \mathbf{G}_y \mathbf{v}_0 - \mathbf{i}_{h-aux,0}$$

This updated value is delivered to the SNN.

Step VII. Step I to step VI are repeated as required by the simulation time.

At step IV the calculated values of \mathbf{i}_{fw} are saved in a memory for their subsequent use at step V. Buffer size is calculated by:

$$\left\lceil \frac{\tau_{\max}}{\Delta t} \right\rceil \quad (6.10)$$

where, τ_{\max} is the highest propagation time of the line. If all propagation times were integer multiples of the simulation time step, then all the values for \mathbf{i}_{fw} could be readily retrieved as these correspond to stored data [33],[34]. Nevertheless, in most cases the various propagation times of a multiconductor line will seldomly be integer multiples of the simulation time step. Thus, values which lie between existing data are needed in order to compute the contribution to the next time step. Linear interpolation is used to obtain the required past value [33],[34].

Figure 6-3 depicts the buffers for the travelling waves of currents originating at both line ends, where the simulation time step is $\Delta t=0.03\text{ms}$ and the line travel time is assumed at $\tau=0.18\text{ms}$. It can be observed there that at simulation time 0.24ms the required history values of are at 0.06ms which are readily available from the buffer (table). Now, at Figure 6-4 a simulation time step of $\Delta t=0.04\text{ms}$ is used instead. In this case the required history values at 0.06ms are not available and an interpolation process must be used.

Thus, given that:

$$r\Delta t \leq \tau < (r+1)\Delta t \quad (6.11)$$

where, r is an integer, the following relationship is established:

$$\tau \cong (r + \zeta)\Delta t \quad (6.12)$$

with, $0 \leq \zeta < 1$. On applying linear interpolation:

$$i_{fw,L}(t - \tau_k) \cong i_{fw,L}(t - r\Delta t) + \zeta[i_{fw,L}(t - r\Delta t) - i_{fw,L}(t - r\Delta t - \Delta t)]. \quad (6.13)$$

The use of quadratic interpolation has been investigated in [34] and it has been found that this certainly increases the accuracy of the line model with a very small computational cost. Nevertheless, as the accuracy gain is very small, the linear interpolation method is the one adopted here.

t(ms)	$i_{fw,0}$	$i_{fw,L}$
0.0	*	*
0.03	*	*
0.06	*	*
0.09	*	*
0.12	*	*
0.15	*	*
0.18	*	*
0.21	*	*
0.24	*	*




Figure 6-3 : Integer multiple buffer scheme.

t(ms)	$i_{fw,0}$	$i_{fw,L}$
0.0	*	*
0.04	*	*
0.08	*	*
0.12	*	*
0.16	*	*
0.20	*	*
0.24	*	*




Figure 6-4 : Interpolation buffer scheme.

6.3 RTWB Using Second Order Realizations

From the results reported at section 5.4 it follows that, for real-time applications the RTWB model realized with second order blocks (RTWB2B) is an attractive alternative to the realization with first order blocks (RTWB). The computational speed of RTWB2B is higher than that of RTWB. This gain comes at the cost of a small loss of accuracy. Thus this section describes the way to implement RTWB2B in a real-time platform, such as RT-Lab.

The WB line model described at section 3.5 with the modifications proposed at section 5.2 for performing the required computations with real arithmetic is coded first in Matlab M-code, then in Fortran 95 and finally in C language. At the writing of thesis the C code version of the RTWB2B model hasn't been further implemented as an S-function for Simulink and as an object inside RT-Lab. Nevertheless, its implementation can be done in much the same way as that of the RTWB.

RTWB2B can be also programmed as a set of two separate sub-blocks, each one representing one line end. In general, the implementation steps are the same as for the RTWB; although, the calculation of shunt currents, auxiliary currents, forward currents and internal states is must be modified by using expressions at section 5.2 as follows:

Step I. SSN uses the known history current values, either from initial conditions or from previous simulation steps to determine network nodal voltages. \mathbf{v}_0 and \mathbf{v}_L are among these and are given as input to RTWB2B.

Step II. Shunt current due to the characteristic admittance of the line is calculated by (5.37), repeated here for convenience:

$$\mathbf{i}_{sh,0} = \mathbf{G}_y \mathbf{v}_0 + \sum_{i=1}^{N_y/2} \mathbf{y}_i$$

Step III. Auxiliary-current source-values, due to the traveling waves form the remote line end, are updated by (5.33):

$$\mathbf{i}_{h-aux,0} = \sum_{k=1}^{N_g} \sum_{i=1}^{Nh(k)/2} \mathbf{x}_{k,i}$$

Step IV. Forward or local traveling wave currents are calculated by (3.27) for the line terminal at $x=0$ which, after an algebraic process, can be rewritten as:

$$\mathbf{i}_{fw,0} = 2\mathbf{i}_{sh,0} - \mathbf{i}_{h-aux,0}$$

These values are delivered to the sub-block representing the line end at $x = L$ and branch currents \mathbf{i}_0 are conveniently evaluated as follows by (6.8):

$$\mathbf{i}_0 = \mathbf{G}_y \mathbf{v}_0 + \mathbf{i}_{hist,0}$$

Step V. Internal states inside the line model are updated by means of (5.32) and (5.36), which are repeated here:

$$\mathbf{y}_i = -\eta_i \mathbf{y}_i' - \mathbf{t}_i \mathbf{y}_i'' + \mathbf{A}_i \mathbf{v}_0' + \mathbf{M}_i \mathbf{v}_0''$$

and

$$\mathbf{x}_{k,i} = -\eta_{k,i} \mathbf{x}_{k,i}' - \mathbf{t}_{k,i} \mathbf{x}_{k,i}'' + \mathbf{\Phi}_{k,i} \mathbf{u} + \mathbf{K}_{k,i} \mathbf{u}' + \mathbf{N}_{k,i} \mathbf{u}''.$$

with

$$\mathbf{u} = \mathbf{i}_{fw,L}(t - \tau_k)$$

Step VI. History current contribution to the network representation from the line end at $x=0$ is updated by (6.9):

$$\mathbf{i}_{hist,0} = \mathbf{i}_{sh,0} - \mathbf{G}_y \mathbf{v}_0 - \mathbf{i}_{h-aux,0}$$

The updated value is delivered to the SSN.

Step VII. Step I to step VI are repeated as required by the simulation time.

The implementations of RTWB and RTWB2B are very similar, the difference resides in the calculation of values of currents and in the state updates. Thus, Figure 6-2 represents both cases. It is clear from the previous analysis that the implementation of RTWB2B is easier than the one for RTWB. Handling of buffers and travelling-currents interpolation continue to be as in the RTWB case despite the fact that two history terms are needed for the RTWB2B case.

6.4 Limiting Factors in the RTWB Model

Generally speaking the implemented model is capable of performing as its off-line counterpart. Nevertheless due to physical as well as calculation time restrictions imposed by the

selected real-time platform the smallest time step which can be achieved in a real-time simulation is $5\mu\text{s}$. In HIL applications with I/Os connected to the real-time simulator the PCIe links used to transmit data to/from the cores and I/O cards limit the minimal simulator time step to a value of $5\mu\text{s}$ [44].

In general the speed of the RTWB model itself depends on three factors: 1) the number of real poles in the rational approximations of Y_c and H , 2) the number of imaginary poles in the rational approximations of Y_c and H , and 3) the number of phases. These factors may cause an overrun in the simulation preventing to achieve real-time simulations if the time-step is too small.

The RTWB model is accurate at representing voltages and currents for aerial transmission lines and underground/submarine cable cores. Nevertheless, attention must be given to underground/submarine cable sheaths because if the time step is not sufficiently small, misleading waveforms may be obtained.

This issue occurs also in off-line simulators as is shown in the next section. However, the advantage of off-line simulators is that the time step can be reduced to the required value in order to accurately represent the simulated phenomenon, something that cannot always be done with real-time simulators.

A key aspect in the development of the RTWB model is the improvement of the numerical performance with respect to the original ULM implementations. The model execution time is a critical aspect of real-time simulations the reason being that the simulation process is interfaced with real-world devices through analog and digital converters. These converters and the simulation process driving them are controlled by a real-time clock inside the simulator, it is therefore very important that the calculations of the network solver and in the models be completed at every time step of the simulator. For this reason, in real-time simulations, the time step is measured as the worst case calculation time for all time steps. Once this worst case time step is known, it is possible to complete all computations in real time and the interface with real-world devices is not disrupted.

The next section shows several examples where the capabilities of the model are presented in a more graphical way both, off-line simulations and real-time simulations are presented.

6.5 Test of RTWB in a Real-Time Platform

6.5.1 Test 1: RTWB ac 3-phase Cable

The underground 3-phase cable system presented in section 3.6.1 is used here to test the RTWB model in a real-time platform. The test circuit is the same shown in Figure 3-4 without capacitor C1. Simulation results are presented in Figure 6-5 to Figure 6-8, where phase a is in blue, phase b is in green and phase c is in red. A dashed line is used for EMTP-RV waveforms while a solid line is used for the results obtained with RTWB.

The observed minor differences are related to the different numerical integration techniques as well as the solver used in EMTP-RV and RT-LAB. The smallest achieved real-time integration time-step for this example was 12 μ s with two processors.

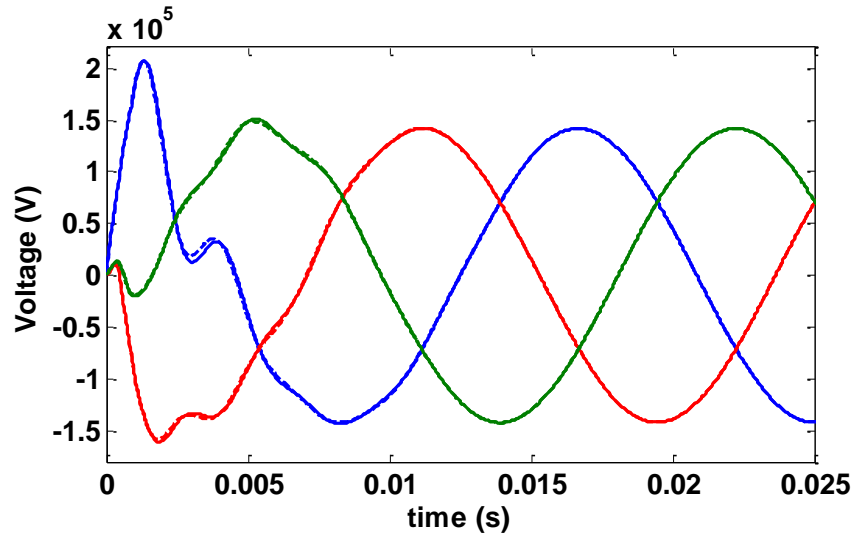


Figure 6-5 : RTWB ac 3-phase cable sending-end core-voltages, real-time test. Solid line for EMTP-RV results dashed line for RTWB results.

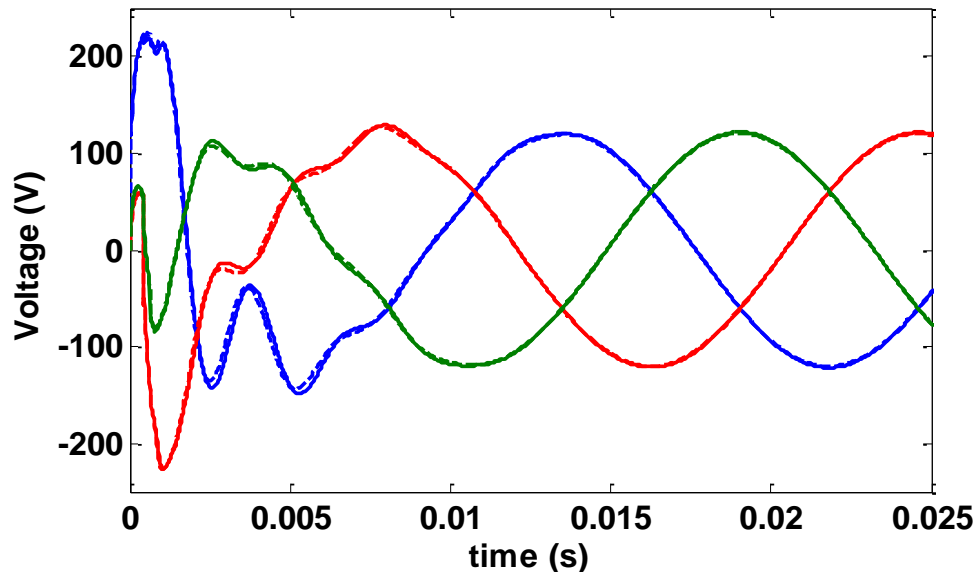


Figure 6-6 : RTWB ac 3-phase cable sending-end sheath-voltages, real-time test. Solid line for EMTP-RV results dashed line for RTWB results.

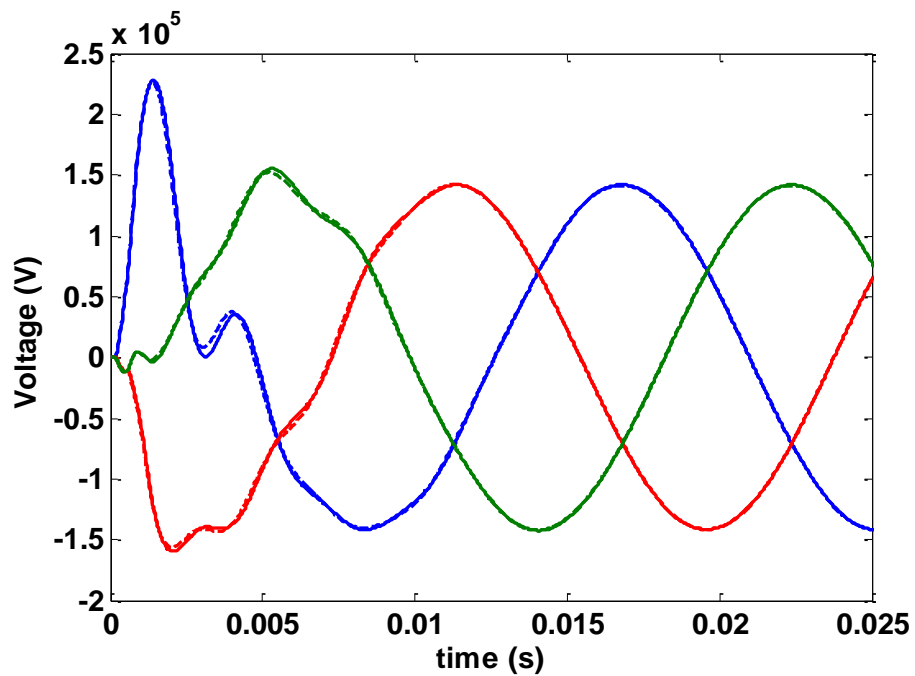


Figure 6-7 : RTWB ac 3-phase cable receiving-end core-voltages, real-time test. Solid line for EMTP-RV results dashed line for RTWB results.

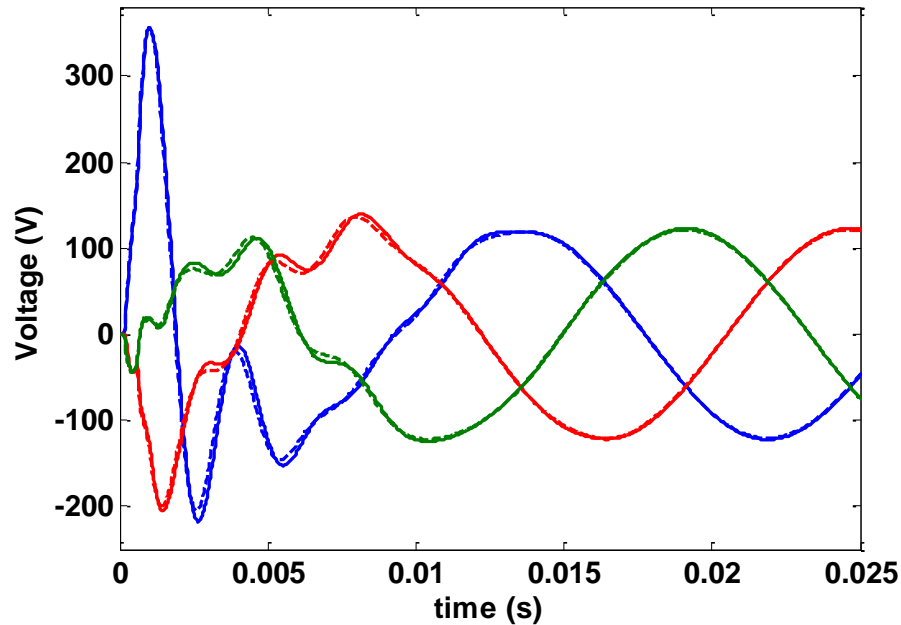


Figure 6-8 : RTWB ac 3-phase cable receiving-end sheath-voltages, real-time test. Solid line for EMTP-RV results dashed line for RTWB results.

In order to clarify the time step issue mentioned in section 6.4 this case is simulated again using an ideal source. Results are obtained using the off-line simulator EMTP-RV for two different time steps: case one is simulated with a time step of $1\mu\text{s}$ (solid line) and the second one with a time step of $10\mu\text{s}$ (dashed line). For this test only the voltages at the sending-end sheaths have visible differences. Thus, voltage waveforms for the sending end sheaths are shown in Figure 6-9 where phase a is in blue, phase b is in green and phase c is in red. Results are plotted in a solid line for the first case and in dashed line for the second case. This example shows that if the phenomenon is too fast smaller time steps are needed in order to observe high frequencies. Thus, when the RTWB model is applied in the real-time simulator caution must be taken and comparisons with off-line simulations with a small time step should be performed or if the fastest phenomenon in the simulation is known then the time step must be calculated according to the phenomenon frequency. A time step of $10\mu\text{s}$ will allow obtaining a bandwidth of 50 kHz [51] which cover most switching transients. Although, electromagnetic transients can go up to 100 kHz and more if lightning is taken into account.

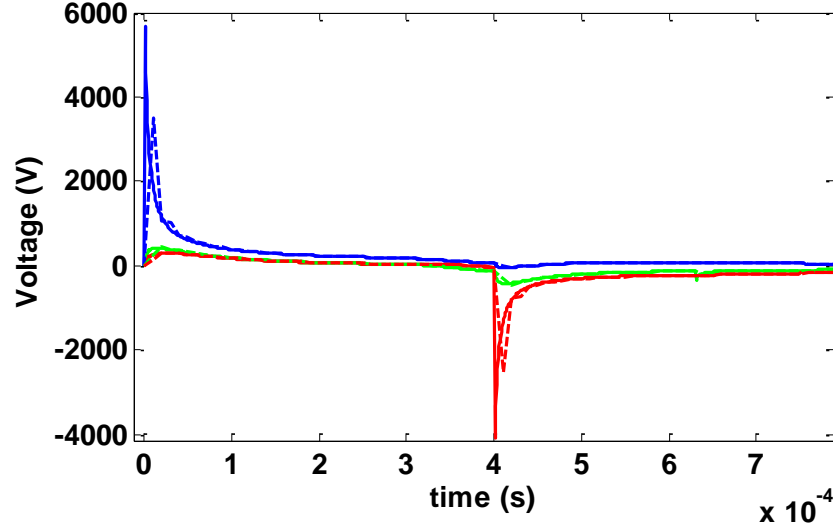


Figure 6-9 : RTWB ac 3-phase cable sending-end sheath-voltages, solid line simulation with a $1\mu\text{s}$ time step, dashed line simulation with a $10\mu\text{s}$ time step.

6.5.2 Test 2: BC HYDRO 9-phase aerial line

The 9-phases aerial line presented in section 3.7.2 is used here with the test circuit shown in Figure 6-10 where the values of the source, impedance and closing times are the same as in section 3.6.1.

For this case the fitting of \mathbf{Y}_c required 9 real poles and non complex poles, while the fitting of \mathbf{H} required 28 real poles and 2 complex poles. For this line traditional mode grouping causes numerical instability in the time-domain solution and must be addressed with the approach proposed in section 4.6.4 where mode grouping is discussed.

Simulation results are presented in Figure 6-11 to Figure 6-13, where phase a is in blue, phase b is in green and phase c is in red. A dashed line is used for the EMTP-RV resulting waveforms while a solid line is used for the RTWB results. The observed minor differences between both results are related to the different numerical integration techniques as well as the solver used in EMTP-RV and RT-LAB. The achieved smallest real-time integration time-step for this example was $20\mu\text{s}$ using two processors.

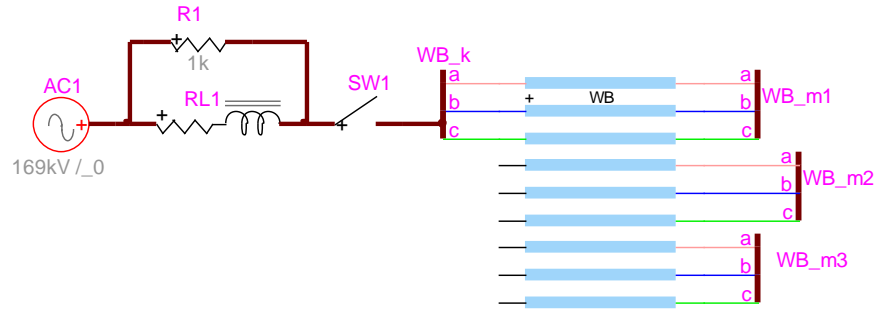


Figure 6-10 : BC HYDRO 9-phase aerial line test circuit, real-time test.

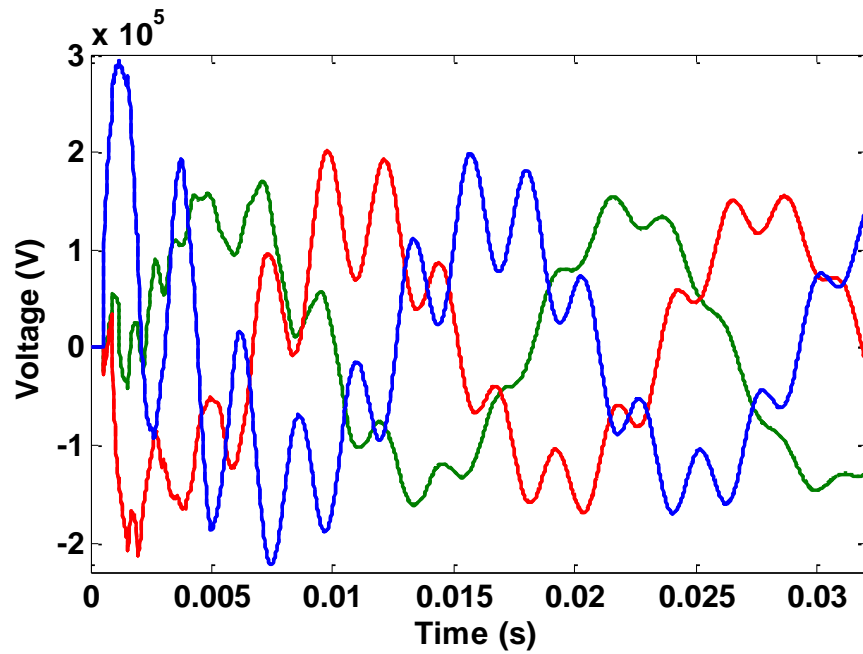


Figure 6-11 : BC HYDRO 9-phase aerial line circuit 1 receiving-end voltage-waveforms, real-time test. Solid line for EMTP-RV results dashed line for RTWB results.

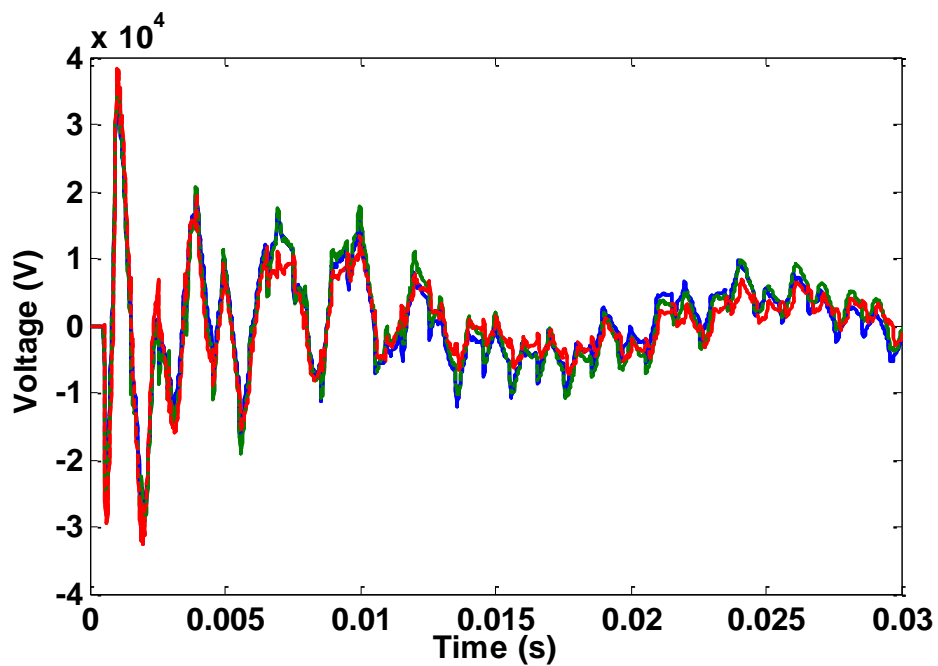


Figure 6-12 : BC HYDRO 9-phase circuit 2 receiving-end voltage-waveforms, real-time test. Solid line for EMTP-RV results dashed line for RTWB results.

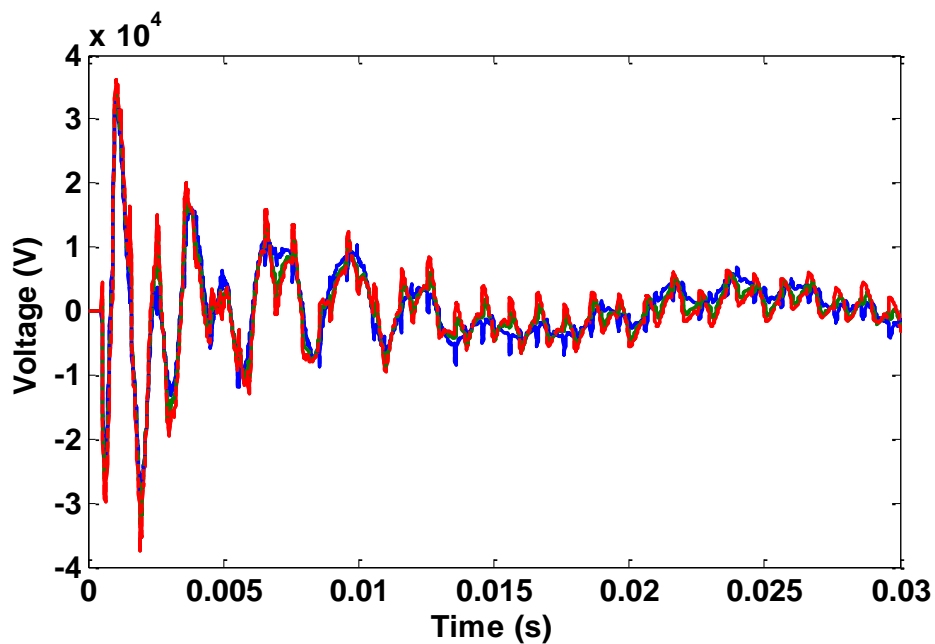


Figure 6-13 : BC HYDRO 9-phase circuit 3 receiving-end voltage-waveforms, real-time test. Solid line for EMTP-RV results dashed line for RTWB results.

6.5.3 Test 3: RTWB 6-phase underground cable

The underground cable system of section 3.6.3 is used for this test with the same parameters and test circuit presented there. In this case the fitting of Y_c requires 12 real poles and no complex poles, while the fitting of H requires 22 real poles and 24 complex poles.

Simulation results are presented in Figure 6-14, where EMTP-RV results are in solid line while RTWB results are in dashed line.

The observed minor differences are related to the different numerical integration techniques as well as the solver used in EMTP-RV and RT-LAB. For this case the test was run only offline with a time step of $1\mu s$. Real-time simulation was not possible given that the smallest travel time in the system is less than $7\mu s$ making its simulation impossible in real-time.

6.5.4 Test 4: transmission network

The power transmission network of section 3.6.4 is simulated here in real-time using the RTWB. All the network data and simulation circuit is as in section 3.6.4. However, the simulation in this case consists only in the fault of phase a and the subsequent liberation of the line running between Bus 7 and Bus 1. The voltage waveforms are measured at Bus 1. The system starts in steady state and at time $t=0.2s$ the fault occurs in the line at the side of Bus 1, the fault is cleared after 0.05s at time $t=0.25s$ by opening the switches between the faulted line. Figure 6-15 shows the voltage waveforms obtained at Bus1. Solid lines are used to represent RTWB results and dashed lines are used to represent EMTP-RV results. The observed minor differences are related to the different numerical integration techniques as well as the solver used in EMTP-RV and RT-LAB. This example is proposed in order to show that the RTWB model performs correctly for more complex examples than the ones showed so far. The achieved smallest real-time integration time-step for this example was $8\mu s$ using five processors.

6.6 Remarks

In this chapter the characteristics of the real-time platform where the RTWB model was implemented were given. An appealing advantage of such platform is its interface with MATLAB/Simulink which makes it very practical for the simulation of power system transients.

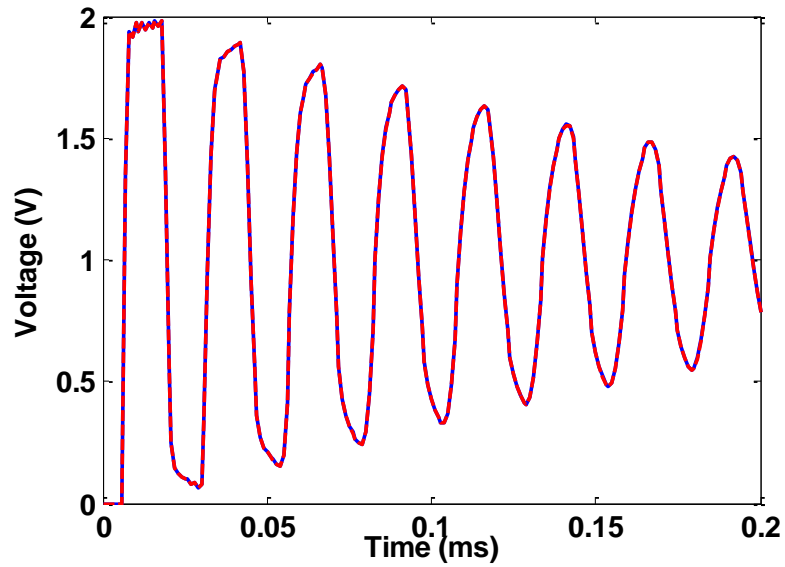


Figure 6-14 : RTWB 6-phase cable voltage waveforms at the receiving end of phase a, real-time test. Solid line for EMTP-RV results dashed line for RTWB results.

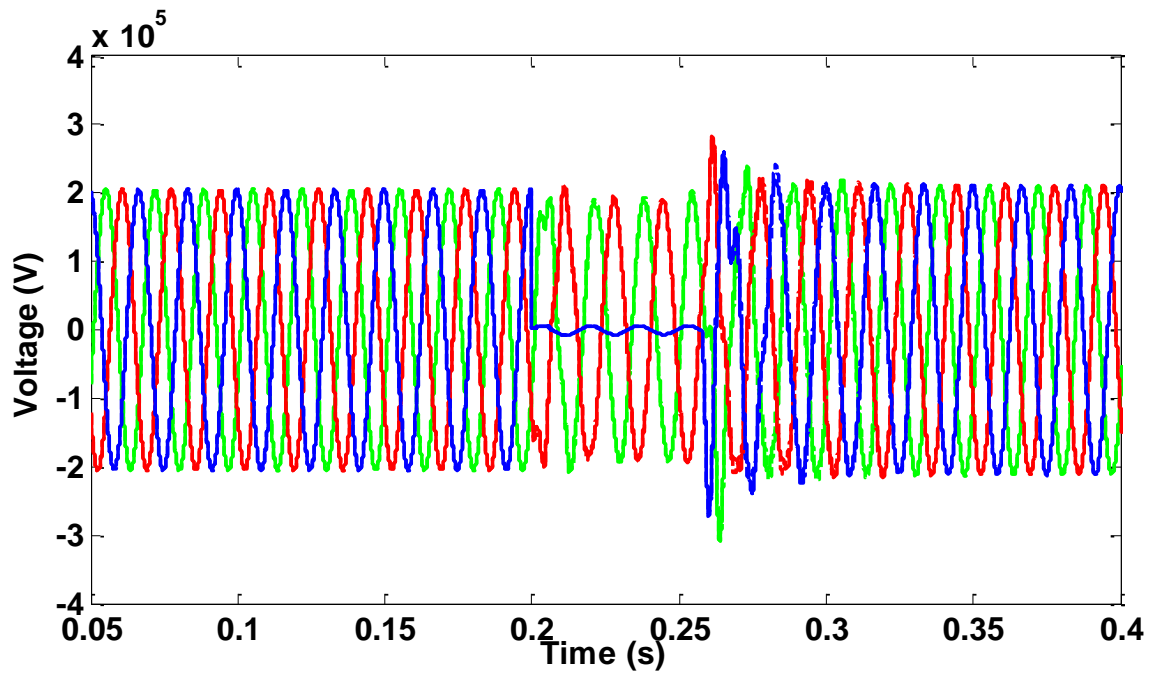


Figure 6-15 : Transmission network voltage waveforms at Bus1, real-time test. Solid line for EMTP-RV results dashed line for RTWB results.

The implementation of the model using first and second order realizations was explained in detail. Even though, second order blocks was not implemented in the real-time platform is clear that its implementation is easier and straight forward since model implementation steps are similar, almost generic for any of the models presented in this thesis.

The limitations of the RTWB model were shown through several examples and it was mentioned that the number of poles in the rational approximations as well as the number of phases are factors which affect the speed and numerical performance of the model. Such examples demonstrate the accuracy as well as the performance of the model in real-time and in off-line simulations. Main differences between the RTWB model implemented in RT-LAB and the WB model of EMTP-RV are due to the solvers and integration rules used in each platform.

At the moment of writing this thesis there are no reports of a full-frequency-dependent line model been implemented in a cluster-based real-time platform. For this reason the model presented here can be considered as the first one of its kind (FFD in RT) and, even though, there are no other comparison points besides off-line simulators, the presented tests suggest that the RTWB model has good accuracy, numerical efficiency and stability.

CHAPTER 7 CONCLUSION

As power systems and apparatuses grow in size and complexity. The use of simulation tools as real-time simulators are required in order to predict and assess their performance under normal and abnormal operation conditions. Transmission lines are a very important component of power networks and are very difficult to accurately simulate due to the strong frequency dependency of their parameters. Nowadays, the most general line model available in off-line simulators is the WB model which is now available in the real-time simulator eMEGAsim from OPAL-RT Technologies under the name of RTWB.

RTWB is the final implementation of the model developed in this thesis and to the best knowledge of this author is the first Full-Frequency-Dependent (FFD) line model being implemented in a cluster-based real-time platform. Even though, RTWB is based in the WB model several improvements were introduced. The most important one is the use of real arithmetic procedures to handle complex state variables a feature that highly improves the efficiency of the model as demonstrated in Chapter 5.

The WB model was used as a base since this is the most general and accurate model available in off-line simulators for it takes into account the full-frequency-dependence of line parameters.

Another model under the name of RTWB2B was proved to be faster than RTWB and to be accurate enough not only to be implemented in a real-time platform but also in an off-line platform since RTWB2B presents a good compromise between accuracy and speed as demonstrated in Chapter 5.

Other methods were proposed in Chapter 5 were it was show that they do not improve the speed of the model but on the contrary they accumulate rounding errors very fast rendering inaccurate responses. Thus their use was discarded.

The characteristics of the real-time platform where the RTWB model was implemented were described in Chapter 6. Main advantages of this platform are the interconnection between nodal and state-space formulations, the interface between the simulator and Simulink's user interface and the attainable simulation speed which makes it very appealing to the user.

The implementation steps for the models proposed in this thesis are presented in detail in Chapter 6. In this chapter, it can be seen that implementations are in general generic for all the models presented in this work.

The accuracy and performance of the RTWB model were tested through various examples that comprehended aerial lines as well as underground cables with several configurations. Such examples are presented in Chapter 5 and Chapter 6.

Rational fitting issues were addressed in Chapter 4. In it was found that obtained rational models with VF or WVF are not always passive which can cause the line model to dramatically fail or present instabilities in time domain simulations and/or give wrong answers. It was also shown in Chapter 4 that by correctly addressing three simple aspects of the fitting process passive rational models can be obtained.

Following conclusions are drawn from this work.

Conventional implementations of the WB model are highly inefficient since they manage all state variables as complex even if they are real. This introduces a big number of trivial operations, multiplications by zero and additions to zero, given the fact that complex poles only represent up to a 50% of the total number of poles in the rational approximations of the Y_c and H functions in most cases.

Complex conjugate poles contain redundant information. Thus, the replacement of complex conjugate equations by real coupled equations is much more efficient from the computational standpoint.

The inclusion of complex conjugate poles as well as real poles in second order states helps to naturally eliminate imaginary quantities in the states. By using this method the model computational efficiency is increased while model accuracy is maintained in an acceptable value. This method is easier to implement and presents a good speed/accuracy ratio.

Higher order blocks do not represent a real advantage regarding computational efficiency on the contrary round off errors do accumulate very fast and quantization errors extremely decrease the accuracy of the model.

Rational models or rational fittings are a very important part of the line model and their accurate approximation is crucial for the sound representation of line transient phenomena.

Nevertheless, important properties as passivity, stability and causality of these approximations must be assured since the lack of one or more of these properties can render flawed time-domain responses.

Even though, the used rational fitting tool assures stability by flipping unstable poles to the left hand-side of the complex plane. Passivity is not always guaranteed, it is better to obtain a passive model since passivity implies causality and stability, but causality and stability do not imply passivity.

A sound representation of the to-be fitted matrices is necessary, given the nature of \mathbf{Y}_c and \mathbf{H} matrices, guaranteeing this aspect by increasing the number of samples per decade can help to avoid passivity violations by the obtained rational models. Increasing the number of poles for some cases also helps to alleviate passivity violations.

Modal grouping must be addressed carefully since this process can misrepresent the former modal functions and/or stiffen the fitting process given as a result a nonpassive rational model. If mode grouping is wanted it is necessary not only to take into account the angles and time delays but also to the modal propagation function magnitudes.

7.1 Future Work

The greatest limitation of a software line model in terms of calculation speed is the number of operations that the model has to perform each time step. Convolutions pose a large numerical burden to the models thus, the higher the quantity of convolutions inside the model formulation the longer would take to the model to run, either in real-time or off-line platforms.

Another aspect that injures the WB model is the extraction of rational models to represent the characteristic admittance matrix and the propagation functions matrix. Such rational representations affect the speed of the model since the number of used poles in these representations directly affects the performance of the WB model. Also obtained rational representations can result nonpassive given as a result non-convergent or incorrect time-domain solutions.

In order to have faster, more accurate and passive models future research should focus in the obtention of either a fitting technique that guarantees not only the passivity of the rational

models but also a compact number of poles. Or in the development of simpler models that involve less computations and easier functions to fit. An appealing idea to achieve the first proposal is to use WVF and introduce passivity enforcement schemes that guarantee passivity for every single case.

Regarding the second proposal a line model based in the method of characteristics can be a good choice. This model is full frequency dependent, works in the modal domain thus there is no need to work with full matrices, there is one smooth matrix to be synthesized and requires only half of the convolutions needed by the WB model.

Although, the model of characteristics presents many advantages there is one disadvantage to be overtaken. The model not only requires time discretization but spatial discretization as well a drawback that has been recently removed for the case of aerial lines [52]. Research still needs to be conducted to develop this model and make it capable of simulating underground cables without the need of discretizing the spatial dimension.

REFERENCES

- [1] H. W. Dommel, "Digital computer solution of electromagnetic transients in single and multiphase networks", *IEEE Trans. On Power Apparatus and Systems*, vol.88, no. 4 pp. 388-399, April 1969.
- [2] J. R. Marti, "Accurate Modeling of Frequency-Dependent Transmission Lines in Electromagnetic Transient Simulations," *IEEE Trans. on Power Apparatus and Systems*, vol. 101, pp. 147-157, 1982.
- [3] B. Gustavsen and A. Semlyen, "Rational approximation of frequency domain responses by vector fitting," *IEEE Trans. Power Delivery*, vol. 14, no. 3, pp. 1052–1061, July 1999.
- [4] R. Iracheta, O. Ramos-Leaños, "Improving Computational Efficiency of FD Line Model for Real-Time Simulations of EMTs," presented at the IEEE North American Power Symposium, NAPS, Arlington, USA, 2010.
- [5] A. Morched, B. Gustavsen, M. Tartibi, "A universal model for accurate calculation of electromagnetic transients on overhead lines and underground cables," *IEEE Trans. on Power Delivery*, vol. 14, no. 3, July 1999, pp. 1032-1038.
- [6] I. Kocar, J. Mahseredjian and G. Olivier, "Improvement of numerical stability for the computation of transients in lines and cables," *IEEE Trans. on Power Delivery*, Vol. 25, Issue 2, April 2010, pp. 1104-1111.
- [7] I. Kocar, "Wide Band Modeling of Transmission Lines and Cables," Ph. D. Thesis, École Polytechnique de Montréal, Department of Electrical Engineering, Montreal, Canada, Jan. 2009.
- [8] E. Gad, "Passivity verification in delay-based macromodels of electrical interconnects," *IEEE Trans. Circuit Syst. I, Reg. Papers*, vol. 52, no. 10, pp. 2173-2187, Oct. 2005.
- [9] R. Radulet, A.I. Timotin, A. Tugulea, "The Propagation Equations with Transient Parameters for Long Lines with Losses", *Rev. Roumaine Sci. Tech. Electrotech. Energetique*, pp. 587-599, 15, (4), 1969.

- [10] R.H. Galloway, W.B. Shorrocks, L.M. Wedepohl, "Calculation of Electrical Parameters for Short and Long Polyphase Transmission Lines", Proc. IEE, Vol. 111, pp.2051-2059, Dec. 1964.
- [11] W.H. Wise, "Propagation of High-Frequency Currents in Ground Return Circuits", Proceedings IRE, Vol. 22, pp. 522-527, 1934.
- [12] S.O. Rice, "Steady State Solutions of Transmission Line Equations", The Bell System Technical Journal, Vol. XX, No. 2, pp. 131-178, April 1941
- [13] L. M. Wedepohl, "Application of Matrix Methods to the Solution of Travelling Wave Phenomena in Polyphase Systems", Proc. IEE, Vol. 110, No. 12, pp. 2200-2212, Dec. 1963.
- [14] D.E. Hedman, "Propagation on Overhead Transmission Lines. I-Theory of Modal Analysis", IEEE Trans. Power App. Syst., Vol. PAS-84, pp. 200-211, March 1965.
- [15] L.M. Wedepohl, "Electric Characteristics of Polyphase Transmission Systems with Special Reference to Boundary-Value Calculations at Power Line Carrier Frequencies", Proc. IEE, Vol. 112, pp.2103-2112, Nov. 1965,
- [16] O. Ramos-Leaños, R. Iracheta, "Wide-Band Line Model Implementation in Matlab for EMT Analysis," presented at the IEEE North American Power Symposium, NAPS, Arlington, USA, 2010.
- [17] Clayton R. Paul, "Analysis of Multiconductor Transmission Lines", John Wiley & Sons, 1994.
- [18] J. Mahseredjian, S. Dennerrière, L. Dubé, B. Khodabakhchian and L. Gérin-Lajoie, "On a new approach for the simulation of transients in power systems," *Proceedings of International Conference on Power Systems Transients*, IPST, 2005.
- [19] B. Gustavsen, G. Irwin, R. Mangelrød, D. Brandt, K. Kent, "Transmission Line Models for the Simulation of Interaction Phenomena between Parallel AC and DC Overhead Lines", IPST, Budapest, Hungary, 1999.
- [20] F. J. Marcano, "Modeling of Transmission Lines Using Idempotent Decomposition," MAsc. Thesis, Department of Electrical Engineering, The University of British Columbia, Vancouver, Canada, Aug. 1996.

- [21] R.M. Mathur, X. Wang, "Real-time digital simulator of the electromagnetic transients of power transmission lines," *Power Delivery, IEEE Transactions on*, vol.4, no.2, pp.1275-1280, Apr. 1989.
- [22] O. Ramos-Leaños, J. L. Naredo, J. Mahseredjian, C. Dufour, J. A. Gutierrez-Robles and I. Kocar, "A Wideband Line/Cable Model for Real-Time Simulations of Power System Transients," *IEEE Trans. On Power Delivery*.
- [23] O. Ramos-Leaños, J. L. Naredo, J. A. Gutierrez-Robles "An Advanced Transmission Line and Cable Model in Matlab for the Simulation of Power-System Transients" in *Matlab-a Fundamental Tool for Scientific Computing and Engineering Applications*, 1st ed. Vol. 1. V.N. Katsikis, Ed. Intech, 2012, pp. 269-303.
- [24] F. J. Marcano, J. R. Marti, "Idempotent Line Model: Case Studies," *Proceedings of International Conference on Power Systems Transients*, IPST, 1997, pp. 67-72.
- [25] J. R. Marti, H. W. Dommel, L. Marti, V. Brandwajn, "Approximate Transformation Matrices for Unbalanced Transmission Lines," in *Proc. PSCC*, 1987, pp. 416-422.
- [26] I. Kocar, J. Mahseredjian, G. Olivier, "Weighting Method for Transient Analysis of Underground Cables," *IEEE Trans. on Power Delivery*, Volume: 23, Issue: 3, pp 1629-1635, July 2008.
- [27] C. Dufour, L. Hoang, J. C. Soumagne, A. El Hakimi, "Real-time simulation of power transmission lines using Marti model with optimal fitting on dual-DSP card," *Power Delivery, IEEE Transactions on* , vol.11, no.1, pp.412-419, Jan 1996.
- [28] W. Xuegong, D. A. Woodford, R. Kuffel, R. Wierckx, "A real-time transmission line model for a digital TNA," *Power Delivery, IEEE Transactions on* , vol.11, no.2, pp.1092-1097, Apr 1996.
- [29] L. Marti, "Simulation of electromagnetic transients in underground cables with frequency dependent modal transformation matrices", Ph. D. Thesis, Department of Electrical Engineering, The University of British Columbia, November 1986.
- [30] L. M. Wedepohl, "Electrical characteristics of polyphase transmission systems with special reference to boundary-value calculations at power-line carrier frequencies," *Proceedings of the Institution of Electrical Engineers*, vol.112, no.11, Nov. 1965, pp.2103-2112.

- [31] Hendrik W. Bode, *Network Analysis and Feedback Amplifier Design*, D Van Nostrand Company, London, 1945.
- [32] H. W. Dommel, EMTP Theory Book, 2nd ed., Microtran Power System Analysis Corporation 1992.
- [33] T. de Rybel, J. Marti and M. Hodgson, "Analytical validation of time-step interpolation in Transient Insular Nodal Analysis," in *Proc. Acoustics*, 2008, pp. 3735-3740.
- [34] J. A. Gutierrez-Robles, L. A. Snider, J. L. Naredo, O. Ramos-Leaños, "An Investigation of Interpolation Methods Applied in Transmission Line Models for EMT Analysis," in *Proc IPST*, 2010.
- [35] J. Mahseredjian, "Régimes Transitoire Électromagnétique: Simulation," Éditions Les Techniques de l'Ingénieur, Dossier No.D4130, Réseaux électriques et applications.
- [36] P. Triverio, S. Grivet-Talocia, M. Nakhla, F. Canavero, and R. Achar, "Stability, Causality and Passivity in Electrical Interconnect Models," *IEEE Transactions on Advanced Packaging*, vol. 30, no. 4, pp. 795-808, Nov. 2007.
- [37] L. M. Wedepohl, et al, "Frequency-dependent transformation matrices for untransposed transmission lines using Newton-Raphson method," *IEEE Transactions on Power Systems*, vol.11, no. 3, pp.1538-1546, Aug 1996.
- [38] H. M. J. De Silva, A. M. Gole, J. E. Nordstrom, and L. M. Wedepohl, "Robust passivity enforcement for time-domain simulation of multiconductor transmission lines and cables," *IEEE Trans. Power Del.*, vol. 25, no. 2, pp. 930–938, Apr. 2010.
- [39] B. Gustavsen, "Passivity enforcement for transmission line models based on the method of characteristics," *IEEE Trans. Power Del.*, vol. 23, no. 4, pp. 2286–2293, Oct. 2008.
- [40] A. Charest, M. Nakhla, and R. Achar, "Scattering domain passivity verification and enforcement of delayed rational functions," *IEEE Microwave and Wireless Components Letters*, vol. 19, no. 10, pp. 605-607, Oct. 2009.
- [41] H. V. Nguyen, "Simulation of Lightning Surges in Transmission Lines," Ph.D. Thesis, Department of Electrical Engineering, The University of British Columbia, Vancouver, Canada, Feb. 1996.

- [42] J. L. Naredo, J. Mahseredjian, J. A. Gutierrez-Robles, O. Ramos-Leaños, C. Dufour, J. Bélanger “Improving the Numerical Performance of Transmission Line Models in EMTP,” in *Proc IPST*, 2010.
- [43] D. Deschrijver and T. Dhaene, “Broadband macromodelling of passive components using orthonormal vector fitting,” *Electronic letters of IEE*, vol. 41, no. 21, pp. 1160–1161, 2005.
- [44] J. Bélanger, V. Lapointe, C. Dufour, L. Schoen, “eMEGAsim: An Open High-Performance Distributed Real-Time Power Grid Simulator,” presented at the ICPS, Bangalore, India, 2007.
- [45] MathWorks. Internet: <http://www.mathworks.com/products/simulink/>. Nov. 1 2012
- [46] MathWorks. Internet: <http://www.mathworks.com/products/simpower/>. Nov. 1 2012
- [47] RT-LAB, www.opal-rt.com
- [48] C. Dufour, J. Mahseredjian, J. Bélanger, J. L. Naredo, “An Advanced Real-Time Electro-Magnetic Simulator for Power Systems with a Simultaneous State-Space Nodal Solver”, in *Proc. IEEE/PES*, Sao Paulo, Brazil, 2010.
- [49] C. Dufour, J. Mahseredjian, J. Bélanger, "A Combined State-Space Nodal Method for the Simulation of Power System Transients," *Power Delivery, IEEE Transactions on*, vol.26, no.2, pp.928-935, Apr. 2011.
- [50] ARTEMIS Add-On for the Power System Blockset for Simulink, v. 6.0, Opal-RT Technologies, Inc., Montreal, QC, Canada.
- [51] J. G. Proakis, D. G. Manolakis. *Digital Signal Processing*. Madrid, Spain: Pearson Education, 2007, pp. 18-25.
- [52] J. C. Escamilla, P. Moreno, E. Cruz, “A new Model of Multiconductor Transmission Lines for Time Domain Transient Analysis,” presented at the IEEE North American Power Symposium, NAPS, Arlington, USA, 2010.

APPENDIX I – Numerical Performance, State Space Methods

Equation (3.33) has a dimension of $N \times 1$ and can be evaluated using two different methods. In Method 1 equation (3.39) is directly replaced into (3.33) to give

$$\mathbf{i}_{sh,0} = \mathbf{G}_y \mathbf{v}_0 + \sum_{i=1}^{N_y} \boldsymbol{\eta}_i \quad (\text{A.1})$$

with

$$\mathbf{G}_y = \mathbf{G}_0 + \sum_{i=1}^{N_y} \mathbf{G}_i.$$

$$\boldsymbol{\eta}_i = \alpha_i \mathbf{w}'_i + \lambda_i \mathbf{v}'_0$$

Equation (3.39) is now written as $\mathbf{w}_i = \boldsymbol{\eta}_i + \lambda_i \mathbf{v}_0$. The following solution steps are applied at each simulation time-point and for both sides of the line. Only the left-hand side $x=0$ is shown here:

1. evaluate $\boldsymbol{\eta}_i = \alpha_i \mathbf{w}'_i + \lambda_i \mathbf{v}'_0$ for all N_y ;
2. evaluate $\sum_{i=1}^{N_y} \boldsymbol{\eta}_i$ in equation (A.1);
3. provide the history currents of equation (6.9) to the network solution to find \mathbf{v}_0 ;
4. update $\mathbf{w}_i = \boldsymbol{\eta}_i + \lambda_i \mathbf{v}_0$ for all N_y ;
5. prepare for the next time-point: $\mathbf{w}'_i = \mathbf{w}_i$ and $\mathbf{v}'_0 = \mathbf{v}_0$.

The number of multiplications and additions per time-point are given by the same count: $N_y * N * (2N + 1)$.

In Method 2 equation (3.43) is rewritten as

$$\mathbf{i}_{sh,0} = \mathbf{G}_y \mathbf{v}_0 + \sum_{i=1}^{N_y} \mathbf{x}_i \quad (\text{A.2})$$

Where $\mathbf{x}_i = \mathbf{w}_i - \lambda_i \mathbf{v}_0$ and λ_i is a pre-calculated term. The above solution steps are now modified to become:

1. evaluate $\mathbf{w}_i = \mathbf{x}_i + \lambda_i \mathbf{v}_0$ for all N_y ;

2. evaluate $\sum_{i=1}^{N_y} \mathbf{x}_i$ in equation (A.2);
3. provide the history currents of equation (6.9) to the network solution to find \mathbf{v}_0 ;
4. prepare for the next time-point: $\mathbf{w}'_i = \mathbf{w}_i$ and $\mathbf{v}'_0 = \mathbf{v}_0$.

The number of multiplications and additions per time-point are given by the same count: $N_y * N * (N + 1)$. The gain in the number of operations as compared to Method 1 is $(2N + 1) / (N + 1)$.